A SEARCH FOR BOSONIC DARK MATTER WITH THE MAJORANA DEMONSTRATOR

Jamin Michael Rager

A dissertation submitted to the faculty at the University of North Carolina at Chapel Hill in partial fulfillment of the requirements for the degree of Doctor of Philosophy in the Department of Physics.

Chapel Hill
2017

Approved by:

Reyco Henning

John Wilkerson

Jonathan Engel

Art Champagne

Fabian Heitsch

ABSTRACT

Jamin Michael Rager: A Search for Bosonic Dark Matter with the MAJORANA DEMONSTRATOR
(Under the direction of Reyco Henning)

The motivation for dark matter comes from a range of indirect, observational evidence such as gravitational lensing and galactic rotation curves. As viable parameter space for the traditionally favored WIMP model is carved away by increasingly sensitive measurements, the need arises to pursue alternative models, such as bosonic dark matter. Though its primary scientific purpose is to search for neutrinoless double-beta decay, the MAJORANA DEMONSTRATOR provides a good platform for probing bosonic dark matter because of its low backgrounds and the low capacitance of its p-type point contact detectors. Here, we present an updated search for bosonic dark matter with 3454.7 kg $\cdot$ d of exposure. We improve our previous result on pseudoscalar particles by a factor of 2.5 and on vector particles by a factor of 6, setting world-leading upper limits on the couplings for both species.

ACKNOWLEDGEMENTS

I would like to thank my family for their loving support and my friends for their constant encouragement. A big thanks to Clint Wiseman, Bryan Zhu, and Tom Caldwell for all the help and advice they gave me with my data analysis. I would like to acknowledge Kris Vorren, whose work laid a big part of the foundation for this dissertation. Thank you to our PI, John Wilkerson, for supporting my PhD research. And finally, I want to thank my PhD advisor, Reyco Henning, for training me as a nuclear physicist, for teaching me most of what I know about C++, for setting an excellent example as a scientist, and for all his patient assistance and encouragement over these past six years.

"But they that wait upon the LORD shall renew their strength; they shall mount up with wings as eagles; they shall run, and not be weary; and they shall walk, and not faint."

Isaiah 40:31

TABLE OF CONTENTS

LIST OF TABLES

LIST OF FIGURES

LIST OF ABBREVIATIONS AND SYMBOLS

$0\nu\beta\beta$	Neutrinoless Double-beta Decay
ALP	Axion-Like Particle
BDM	Bosonic Dark Matter
CAD	Computer Aided Design
CDM	Cold Dark Matter
CI	Confidence Interval
CMB	Cosmic Microwave Background
DAQ	Data Acquisition System
EFCu	Electroformed Copper
FWHM	Full Width at Half Maximum
HPGe	High Purity Germanium Detector
IR	Infrared
LMFE	Low Mass Front End
LN	Liquid Nitrogen
MOND	Modified Newtonian Dynamics
NDF	Number of Degrees of Freedom
NERSC	National Energy Research Scientific Computing Center
PDF	Probability Density Function

PPC	P-type Point Contact
PSA	Pulse Shape Analysis
QCD	Quantum Chromodynamics
ROI	Region of Interest
SURF	Sanford Underground Research Facility
SUSY	Supersymmetry
TCR	Temporary Cleanroom Facility
WIMP	Weakly Interacting Massive Particle

CHAPTER 1: Introduction

Dark matter is a type of matter that does not interact via the electromagnetic or strong nuclear force. It is motivated by a variety of indirect, observational evidence and is an integral part of the standard model of big bang cosmology called λCDM. While the traditionally favored candidate for dark matter is a class of weakly interacting, non-baryonic fermions known as Weakly Interacting Massive Particles (WIMP's), the experimental progress on WIMP detection has ruled out much of the viable WIMP parameter space and has opened the door for alternative theories. One such alternative theory is bosonic dark matter. This dissertation will describe the recent efforts of the MAJORANA DEMONSTRATOR to directly detect bosonic dark matter.

Section 1.1: Motivation

The favored model of big bang cosmology is known as λCDM. The theory incorporates a cosmological constant, λ, associated with dark energy, cold dark matter (CDM), and ordinary matter. Cold dark matter is called cold because its kinetic energy is nonrelativistic. Numerous predictions made by λCDM have been confirmed in recent years, such as the observation of baryon acoustic oscillations in 2005 by the Sloan Digital Sky Survey [1], the polarization of the CMB observed in 2002 by DASI [2], and the 2015 Plank observations of the temperature power spectrum [3]. Because of these numerous successes, there is good reason to believe that λCDM is a fairly reliable theory, though it admittedly has a few issues such as the small-scale crisis [4]. Part of the attractiveness of λCDM lies in its simplicity, as it contains a small number of independent parameters [5]. By fitting λCDM to data such as the CMB temperature power spectrum from Plank, it is possible to calculate a theoretical prediction for the abundance of dark matter in the universe.

There is a plethora of indirect, observational evidence for dark matter, though this discussion will not give an exhaustive list. One of the most commonly cited pieces of evidence is galactic rotation curves. Rotation curves plot the average transverse orbital velocity of matter within a galaxy as a function of distance from the galactic center. An example of a rotation curve is given in Figure 1.1. Orbital velocity is estimated by measuring the red and blue shift of light from the receding and approaching arms of the galaxy [6]. The measured velocity can be compared to a prediction made with Keplerian orbital mechanics and the mass profile of the galaxy. At large distances, the expected orbital velocity is given by,

$$v(r) = \sqrt{\frac{GM(r)}{r}} \tag{1.1}$$

where r is radius from the galactic center, G is the universal gravitational constant, and $M(r)$ is the mass contained within a disc of radius r centered on the galaxy. In 1970, Rubin and Ford [7] published a study of the Andromeda galaxy, which noted a flattening of the rotation curve far from the galactic center. This finding was a surprise, as Equation 1.1 indicates that $v(r)$ should fall off at large distances due to the diminishing mass profile inferred by visible light. Rubin and Ford tried to account for the discrepancy by correcting for the gravitationally confined gas far from the galactic center, but this contribution was not sufficient to make up the difference. This discrepancy was also observed in later measurements [8][9][10], and came to be interpreted as evidence for halos of nonluminous matter within galaxies [11][12].

More compelling evidence for dark matter comes from gravitational lensing. General relativity predicts that gravitational wells deform spacetime and bend the trajectories of light. Consider the cartoon in Figure 1.2 and assume a terrestrial observer looking at a very distant galaxy. To reach earth, the light from that distant galaxy must travel through the gravitational well of a massive galaxy cluster. These light rays will be “lensed” by the gravitational well so that the terrestrial observer sees a distorted image. Independent estimates of the mass of the cluster can be inferred from its light output as well as the amount

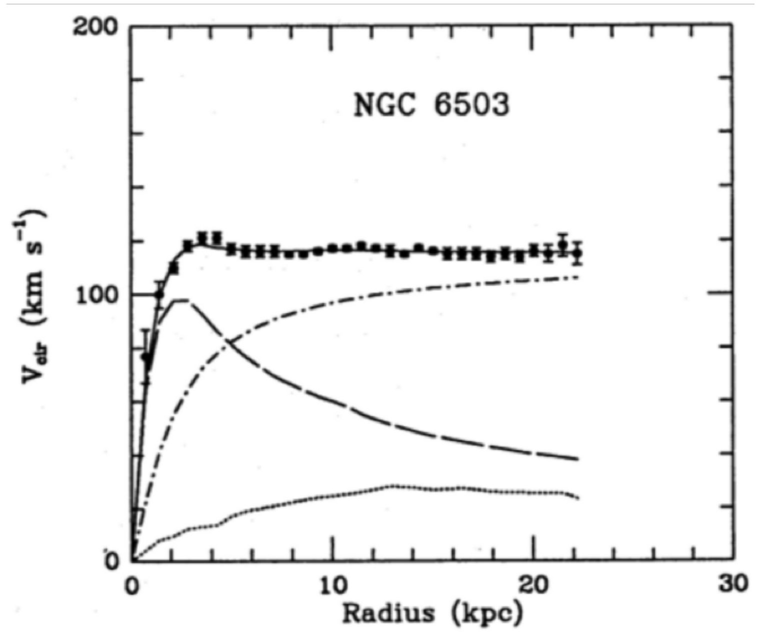

Figure 1.1: Rotation curve of NGC 6503. The points fitted to the curve are the measurement. The dashed line is from visible matter, dotted from confined gas, and dot-dashed from the dark matter halo. Figure from [13].

of gravitational lensing observed. In some observations, as the case of Figure 1.3, the mass estimate from gravitational lensing far exceeds the mass estimate from light output. This discrepancy suggests the presence of nonluminous matter within the cluster. Further, the lensing pattern can be used to reconstruct a map of the dark matter distribution within the cluster, as in Figure 1.4.

Another commonly referenced example of gravitational lensing is shown in Figure 1.5 for the Bullet Cluster. The Bullet Cluster was formed from the collision of two smaller clusters. The X-ray image shows turbulence in the gravitationally confined baryonic gas caused by electromagnetic interactions. The green contours are reconstructions of the mass distribution from gravitational lensing. These reconstructions show greater spatial separation than the baryonic matter in the X-ray image. This is because the baryonic gas from the two clusters interacted, causing it to slow down and separate from the dark matter. The dark matter, on the other hand, did not interact with itself, and the two dark matter clouds passed right through each other.

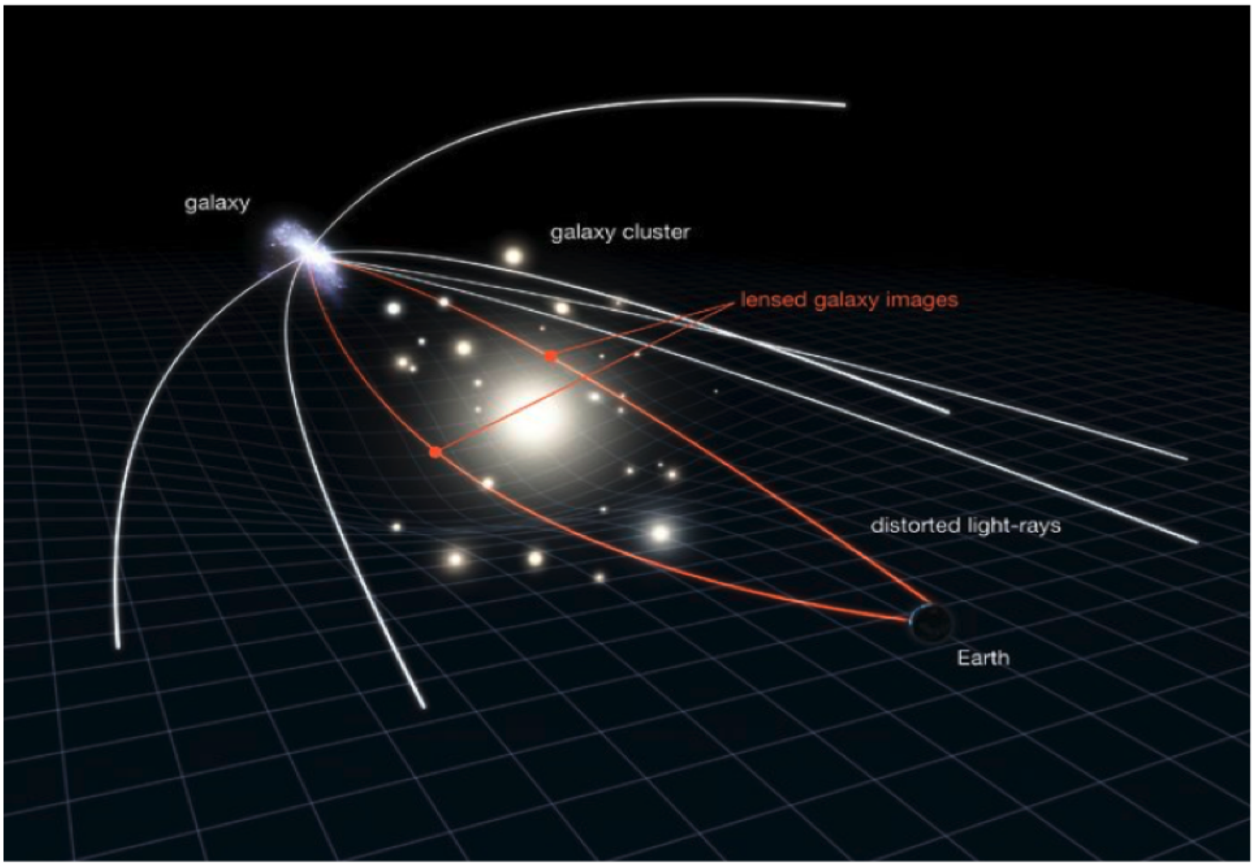

Figure 1.2: An artistic rendering of gravitational lensing as light from a distant galaxy is bent while it travels through the gravitational well of a galaxy cluster on its way to earth. Figure from [14].

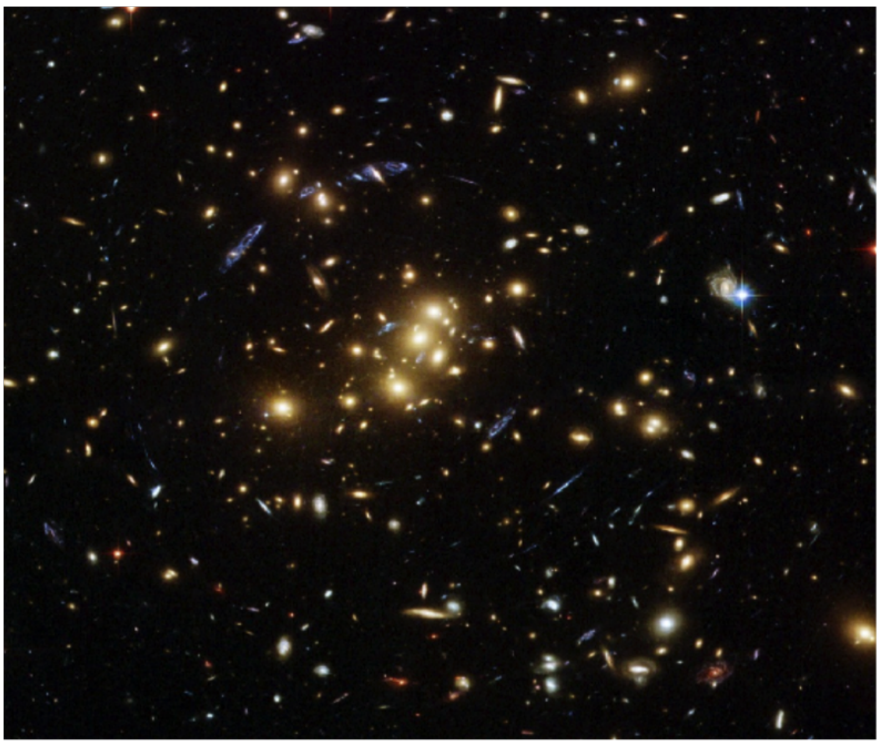

Figure 1.3: Gravitational lensing of light from distant galaxies (blue smears) through galaxy cluster CL0024+17 (yellow blobs). White dots with lens flare are objects within the Milky Way. Figure from [15].

Figure 1.4: Composite image from Hubble Space Telescope of the ring of dark matter around cluster CL0024+17, reconstructed from gravitational lensing. Figure from [16].

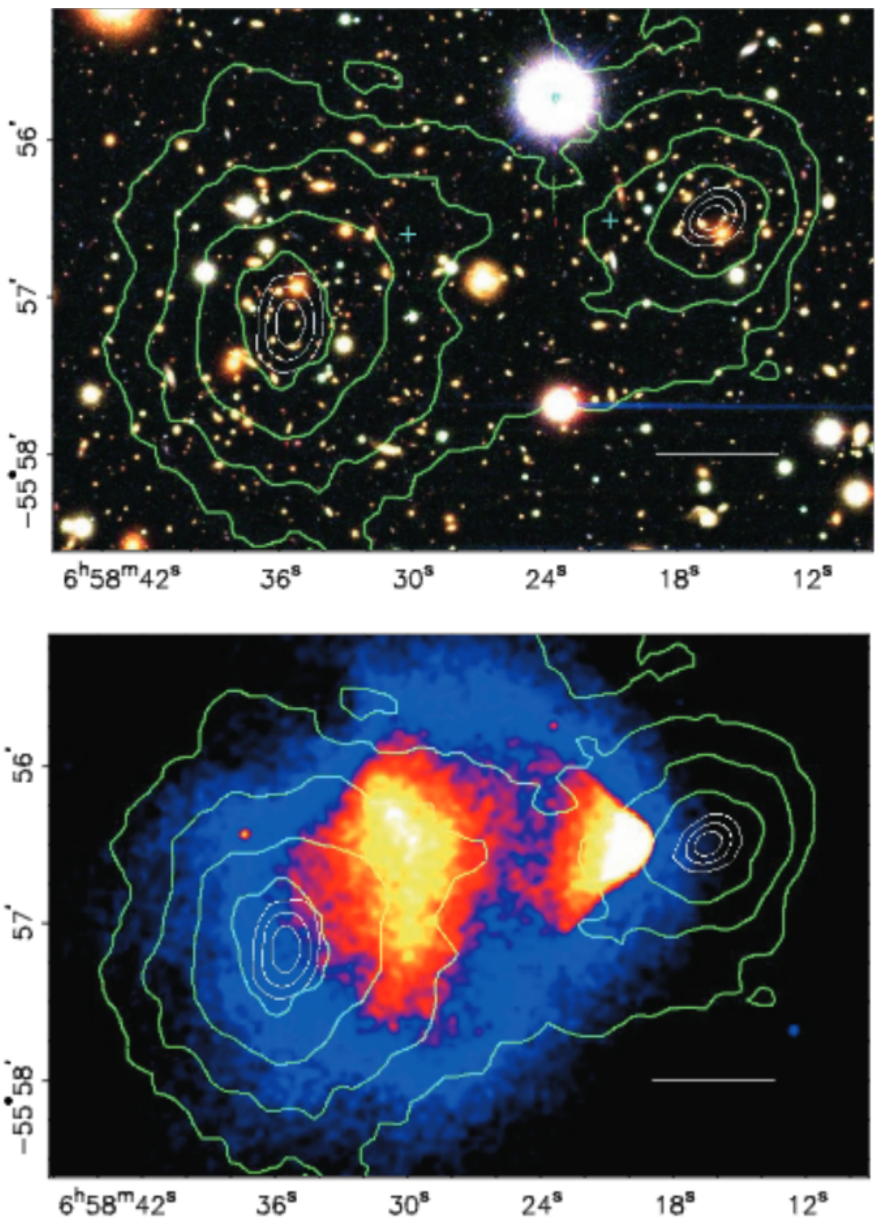

Figure 1.5: Top: contours reconstructing the mass density in the Bullet Cluster from gravitational lensing. Bottom: X-ray image of baryonic gas confined within Bullet Cluster. Figures from [17].

Competing with the dark matter hypothesis are various modified Newtonian dynamics (MOND) models [18] that have enjoyed some success in explaining away rotation curves [19]. A piece of evidence that eludes explanation by MOND, and that is related to the previous discussion on λCDM, is the CMB power spectrum [3], shown in Figure 1.6. The CMB is the remnant of light that decoupled from the baryon-photon plasma in the early universe. Before this decoupling happened, the plasma was in a state of "tension" from the compression force of gravity and the competing expansion force from radiation pressure. Dark matter contributed to this gravitational compression, but not to the radiation pressure. Quantum spacetime fluctuations created acoustic oscillations within the plasma, which are evidenced by the peaks in the CMB temperature power spectrum. The magnitude of the third peak in the spectrum is related to the abundance of nonbaryonic (dark) matter [3].

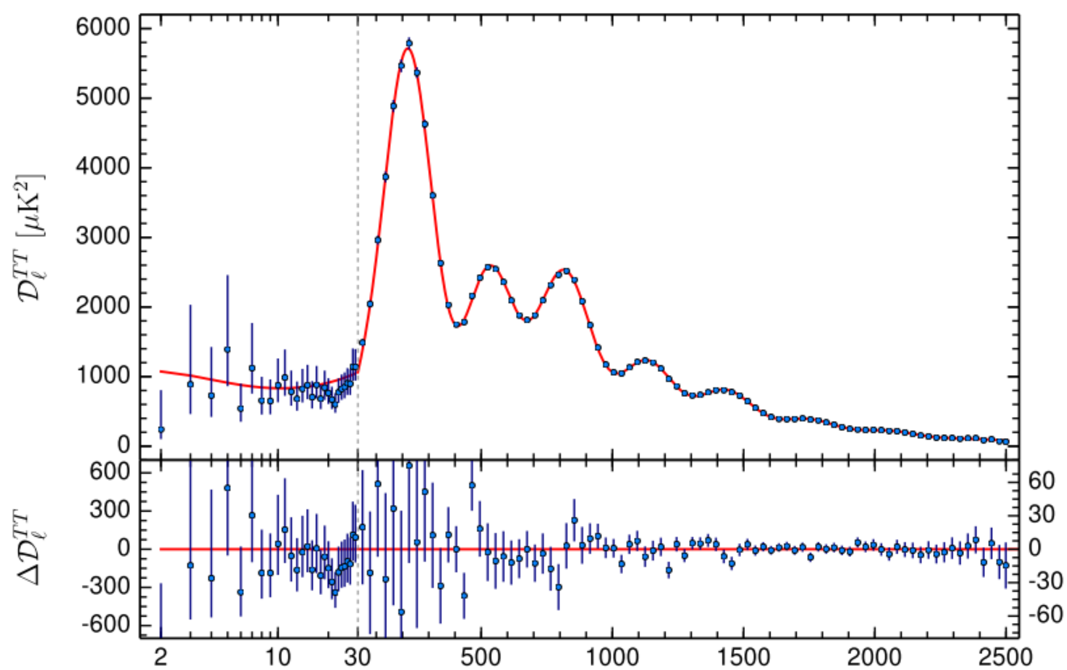

Figure 1.6: CMB temperature power spectrum. The Red curve is a fit using parameters from λCDM. Figure from [3].

Two additional sources of evidence worth mentioning in passing are the velocity dispersions of galaxy clusters and X-ray observations of hot gas confined within clusters. The former pertains to the historical contributions of Fritz Zwicky, who showed that an application of the virial theorem to the observable mass within the Coma cluster predicts a dispersion of galaxy velocities roughly an order of magnitude too small [20] [21]. The second pertains to the fact that X-ray observations of clusters reveal that they confine more hot gas in the intra-cluster region than one would expect given the strength of the gravity created by the visible matter within those clusters [22] [23].

Section 1.2: Dark Matter Species

1.2.1: WIMP's

The historically favored dark matter candidates are weakly interacting massive particles, or WIMP's. They are called "weakly interacting" because they only interact via gravitation and the weak nuclear force. WIMP's are predicted by supersymmetry (SUSY) [24] and are very massive (i.e. on the order 10 GeV - 1 TeV), hence the term "massive" in their name. The most commonly considered SUSY candidate is the lightest neutralino, which is protected from decay by R-parity [25]. They are produced by thermal freeze-out, which means that they were in equilibrium with standard model particles in the early universe before cooling due to expansion drastically slowed their production and annihilation reactions, thus "freezing out" a relic abundance. WIMP's are a type of cold dark matter. If one assumes that WIMP's constitute all the dark matter in the universe, then a necessary requirement to obtaining the correct dark matter abundance is a self-annihilation cross section congruent with a particle mass on the order of hundreds of GeV. This matches the prediction from supersymmetry and is known as the "WIMP Miracle." The WIMP Miracle is the reason why WIMP's have traditionally been the favored dark matter candidate.

An example of an ionization spectrum from WIMP nuclear recoils is shown in Figure 1.7. The spectral feature is a continuum at low energies. As the earth orbits the sun, its velocity relative to the galactic dark matter halo will change, resulting in a dynamic dark matter flux. Indirect detection experiments utilize this fact by looking for an annual modulation in WIMP-induced nuclear recoils. Results from indirect detect experiments are usually plotted as exclusion curves showing the 90% confidence limit on the WIMP cross section with the target medium. The most common detector designs used for WIMP searches are germanium bolometers [26] and xenon [27][28] or argon [29] time projection chambers. Figure 1.8 shows the space of exclusion plots and sensitivity projections from past, present, and future experiments. As WIMP experiments get ever more sensitive, they approach the point at which coherent neutrino scattering becomes an irreducible background [30]. While this does not rule WIMP's out, it does provide motivation for considering alternative dark matter candidates to WIMP's.

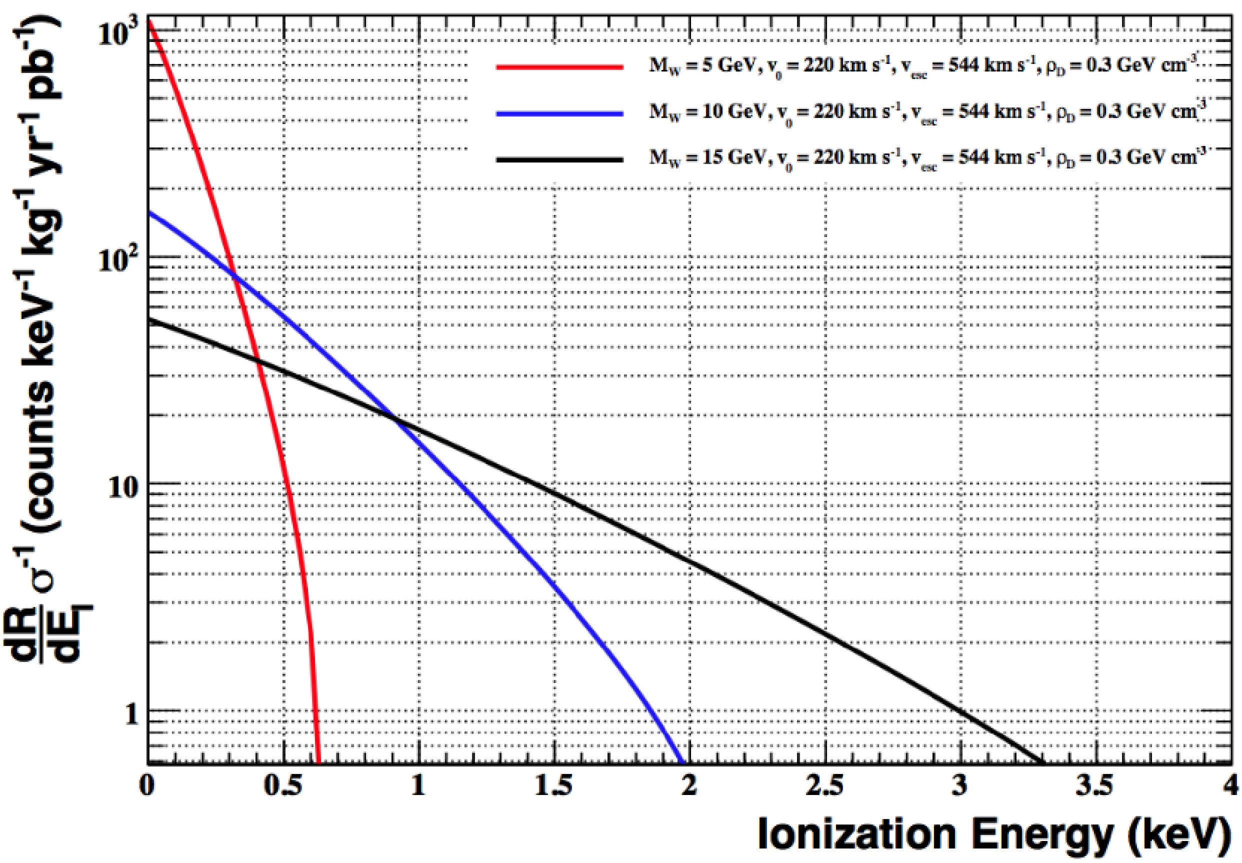

Figure 1.7: WIMP ionization spectrum for varying masses. Figure from [31].

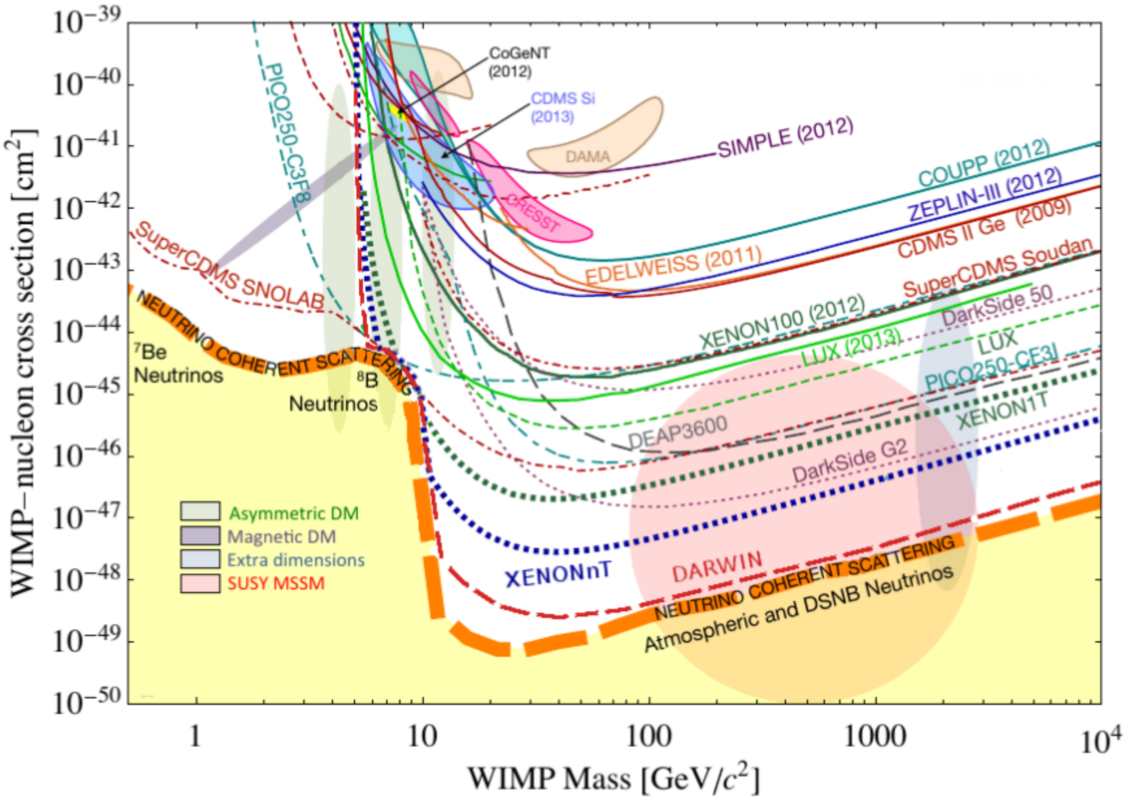

Figure 1.8: 90% confidence limits on the WIMP-nucleon cross section. Each curve excludes the parameter space above it. Solid curves are measured limits and dotted curves are projections. The blobs represent unexplained excesses of events. For cross sections below the orange dotted line, coherent neutrino scattering becomes an irreducible background. Figure from [32].

1.2.2: Axions

Another dark matter candidate that has attracted considerable interest is axions. Axions were originally proposed as a solution to the Strong CP Problem from quantum chromodynamics (QCD) [33][34][35][36]. QCD ostensibly contains the CP violating term in its Lagrangian [37]:

$$L = \frac{\bar{\theta}}{64\pi^2}\epsilon^{\mu\nu\rho\sigma}G^a_{\mu\nu}G^a_{\rho\sigma} \tag{1.2}$$

$G^a_{\mu\nu}$ is the color field strength tensor. The value of the QCD vacuum angle $\bar{\theta}$ is a free parameter not constrained by theory, but one would expect it to be of order 1 from a naturalness standpoint [37]. Precision measurements on the neutron electric dipole moment [38] constrain $\bar{\theta}$ to $\left|\bar{\theta}\right| < 0.7 \times 10^{-11}$ [37], creating a fine-tuning problem. The insight from Peccei and Quinn [33][34], Weinberg [36], and Wilczek [35], was to introduce a symmetry (now called the U(1) Peccei-Quinn symmetry) that is spontaneously broken, resulting in the creation of a pseudoscalar pseudo-Nambu-Goldstone boson known as the axion. $\bar{\theta}$ is dynamically relaxed to $\bar{\theta} = 0$ [37] in the process. The mass of the axion is inversely related to the energy scale of the Peccei-Quinn symmetry breaking. The masses of interest to axion experiments are in the sub-eV range [39], so it is almost more useful to think of the axion as a field rather than as a particle. The two most common channels for axion detection are the axio-electric interaction, explained in the next section, and the Primakoff interaction whereby an axion is converted to a photon (or vice-a-versa) in a strong magnetic field. For an up-to-date review of axion physics, axion experiments, and the bounds set on axions by cosmology and astrophysics, the reader is referred to [39].

1.2.3: Bosonic Dark Matter

The species that this dissertation will focus on is generic dark pseudoscalar and vector bosons. The former are commonly called "axion-like particles" (ALP's) because, like axions, they are massive dark pseudoscalar bosons. However, they differ in that they have no relation to the Strong CP Problem, and should not be confused with axions. Dark vector bosons are analogous to dark photons. The vectors and pseudoscalars interact with ordinary matter through the inelastic vector-electric or axioelectric effect depicted in Figure 1.9, which is similar to the photoelectric effect but with the photon replaced with a dark boson.

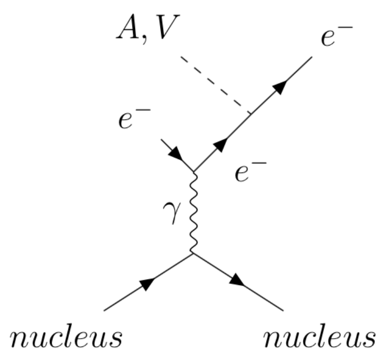

Figure 1.9: A Feynman diagram for the inelastic axioelectric or vector-electric effect.

Bosonic dark matter is produced non-thermally and has negligible kinetic energy, so its signal in an energy spectrum will be a monoenergetic peak from absorption of the photoelectron with energy equal to the rest mass of the absorbed boson, which will be of order 1-100 keV. Because these particles are so much lighter than WIMP's, they need to have a larger number density to achieve the total abundance required by cosmology. The fact that these particles have not yet been observed by the multitude of increasingly more sensitive indirect detection experiments implies that they must have super-weak interaction cross sections, orders of magnitude below weak scale cross sections [40]. There is no enhancement from annual modulation, which is $O(10^{-15})$ and undetectable by current and next-generation experiments [40]. In order to detect these kinds of interactions, it is necessary to have an extremely low background experiment. The MAJORANA DEMONSTRATOR suits this need well, as will be explained in later chapters.

Figure 1.10 shows a number of theoretical constraints on the mass and axio-electric coupling strength of pseudoscalar particles. Decays from bosonic dark matter to standard model particles are not forbidden, and for pseudoscalars, decay to two photons would result in both a galactic and cosmological gamma background analogous to the CMB. From the figure, the strongest constraint on pseudoscalars comes from the galactic gamma background. Astrophysical constraints are the result of the particle's impact on energy loss from stars and supernovae. ALP's are produced within stellar environments via the Compton-like scattering process [40]:

$$e + \gamma \rightarrow e + a \tag{1.3}$$

The abundance line represents the parameters required to produce dark matter in the correct ammount. The axioelectric sensitivity curve arises from the cross-section of ALP's on germanium, assuming a fiducial sensitivity of a detector equivalent to a 1pb cross-section for a 100 GeV WIMP, which roughly represents the sensitivity of an experiment like CDMS II, with 3.75 kg of Ge and 121.3 kg $\cdot$ d of exposure [41], though this is only a benchmark. Though the astrophysical and cosmological bounds exclude the axioelectric sensitivity, it is important to note that these bounds are highly model-dependent. For a further reading on bosonic dark matter, see [40] [39] [42] [43] [44].

Figure 1.11 shows the much more optimistic case of dark vectors. The astrophysical bounds are equivalent in origin to the pseudoscalar case, though it is important to note that production within stellar environments is suppressed for vectors, which is why the astrophysical bounds are so much weaker. The constraint from the galactic gamma background is significantly weaker because two photon decay is forbidden for vectors; they can still decay into three photons, but this is a loop level process [40]. The most important feature of Figure 1.11 is the fact that, from 5 keV to 100 keV, the vector-electric sensitivity (calculated in the same manner as the pseudoscalar case) is competitive with astrophysical bounds. The implication is that current and next-generation dark matter experiments are sensitive to viable parameter space. This makes keV scale dark bosons very attractive dark matter candidates. There have been measurements by numerous experiments since the publication of Figures 1.10 and 1.11 in [40]. These measurements will be presented in Chapter 5.

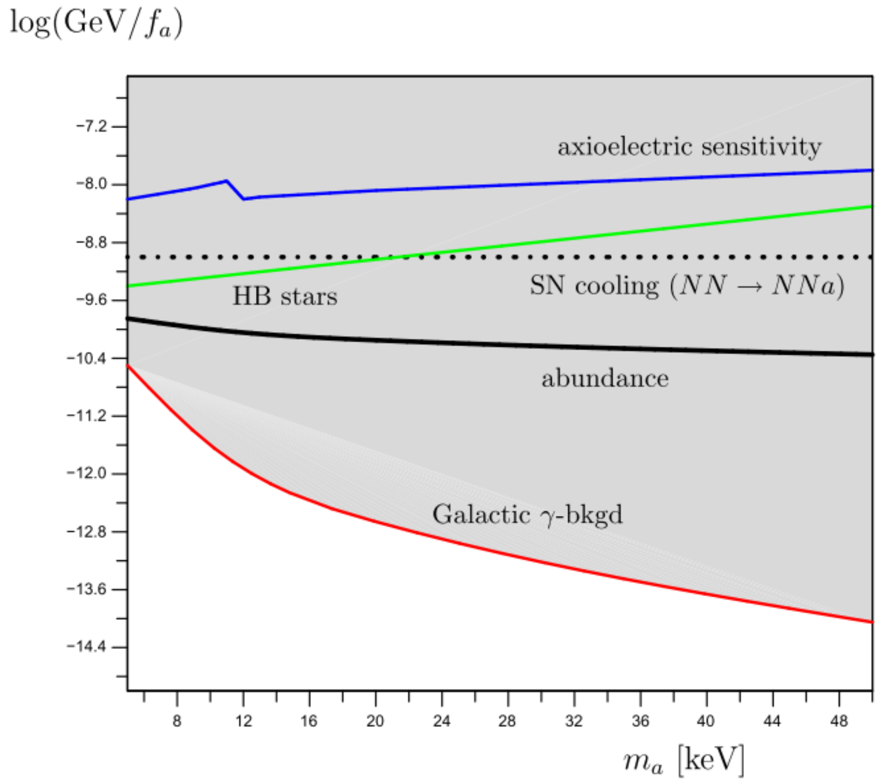

Figure 1.10: The direct detection sensitivity to pseudoscalar dark matter arising from the axioelectric cross-section on Ge, assuming a fiducial sensitivity of the detector equivalent to a 1pb cross-section for a 100 GeV WIMP. Also shown are constraints from He-burning lifetime in HB stars, from supernova cooling, and from the monochromatic γ-background from decays in the Galaxy. Figure from [40].

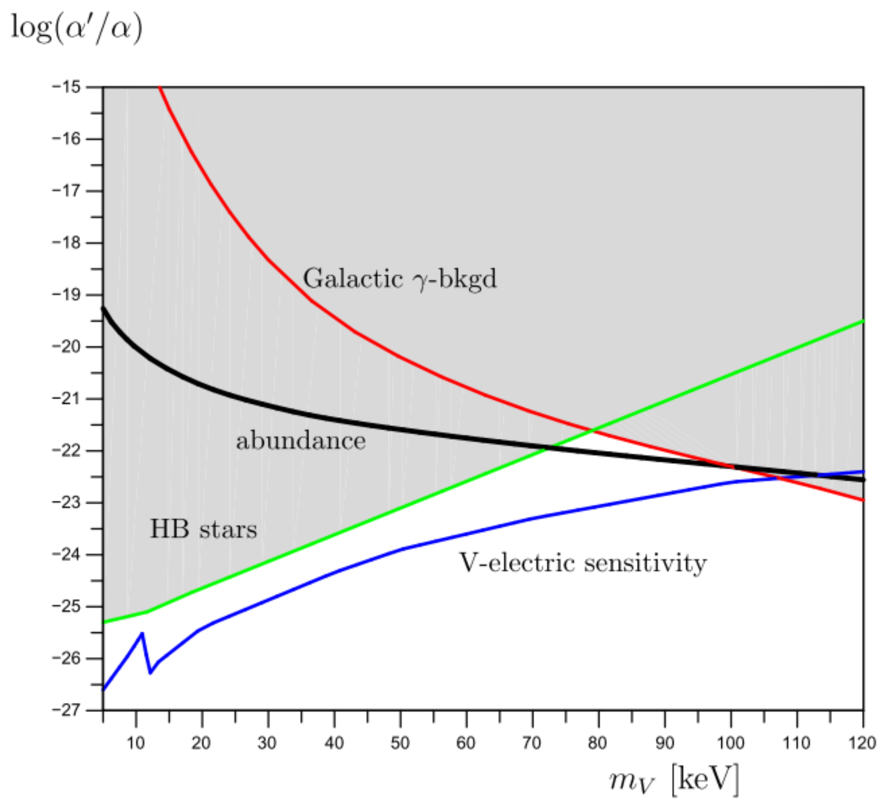

Figure 1.11: The direct detection sensitivity to vector dark matter arising from the vector-electric cross section on Ge, assuming a fiducial sensitivity of the detector equivalent to a 1pb cross section for a 100 GeV WIMP. Also shown are constraints from He-burning lifetime in HB stars and from the γ-background from 3γ-decays in the Galaxy. Figure from [40].

Section 1.3: Neutrinoless Double-beta decay

Because the MAJORANA DEMONSTRATOR is primarily a neutrinoless double-beta decay ($0\nu\beta\beta$) experiment, it is worth saying a few words about neutrinos. The story of the neutrino begins in 1930 with a letter Wolfgang Pauli wrote to Lise Meitner [45]. The continuous shape of the single beta decay spectrum seemed to indicate a violation of energy conservation. To save energy conservation, Pauli hypothesized that the atom contains electrically neutral particles of spin-1/2 and mass no larger than 0.01 times the mass of the proton [45]. Pauli's hypothesis was put on firmer ground when Fermi developed his theory of beta decay in 1934 [46]. Fermi's theory proposed that, in addition to an electron, beta decay also emits a massless, spin-$\frac{1}{2}$ particle with a very small cross section. It was not until 1956 that the neutrino was finally observed by Reines and Cowan in the now famous Savannah River experiment [47].

Before the discovery of the neutrino, a further development for beta decay happened in 1935 when Maria Goeppert-Mayer calculated the probability of double beta decay [48], a process in which a nucleus's atomic number increases by two units, but its mass number stays the same. Double-beta decay is best observed in certain even-even nuclei such as ^{76}Ge, see Figure 1.12. For these specific isotopes, single beta decay is energetically forbidden because it would involve moving to a higher value in mass excess, but double-beta decay gives the nucleus an alternative channel towards a lower energy state. Double-beta decay was first observed in ^{82}Se by Elliot et al. [49].

Neutrinoless double-beta decay was theorized in 1939 by Wendell Furry [51], who proposed that if neutrinos are Majorana fermions, then double-beta decay can proceed without the emission of any neutrinos. To understand this idea, it is instructive to start by writing the most general form of the neutrino mass Lagrangian.

$$-2L_M = \frac{1}{2}(\bar{\psi}m_D\psi + \bar{\psi}^c m_D\psi^c + \bar{\psi}m_M\psi^c + \bar{\psi}^c m_M^*\psi) \tag{1.4}$$

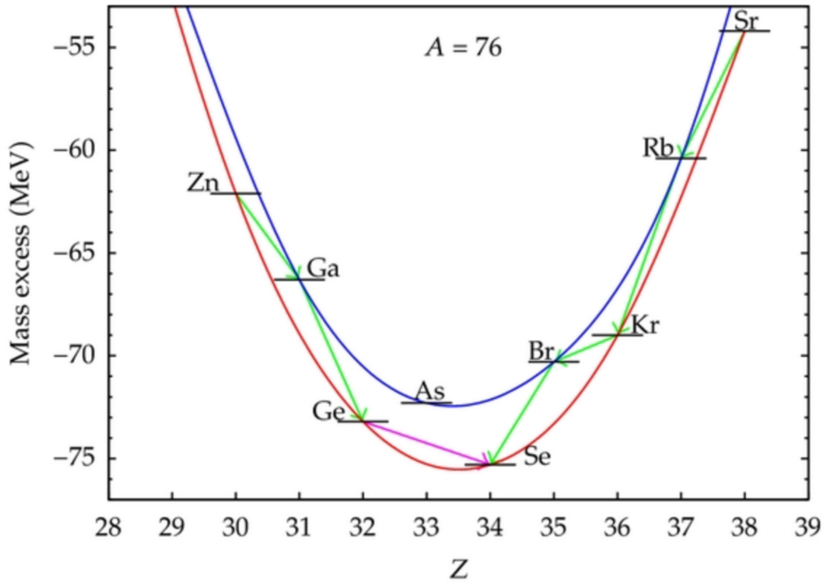

Figure 1.12: Isobars for A = 76 Nuclei. Figure from [50].

where $\bar{\psi}m_D\psi$ and $\bar{\psi}^c m_D \psi^c$ are Dirac mass terms and are invariant under the global phase transition:

$$\psi \rightarrow e^{i\alpha}\psi;\ \psi^c \rightarrow e^{-i\alpha}\psi^c \tag{1.5}$$

By Noether's Theorem, this symmetry can be associated with a conserved quantum number, which is called lepton number in modern particle physics. The terms $\bar{\psi}m_M\psi^c$ and $\bar{\psi}^c m_M^*\psi$ are not invariant under the global phase transition and thus violate lepton number; these are called the Majorana mass terms. It is instructive to rewrite the mass Lagrangian in matrix form:

$$-2L_M = \frac{1}{2}\begin{pmatrix}\bar{\psi} & \bar{\psi}^c\end{pmatrix}\begin{pmatrix} m_D & m_M \\ m_D^* & m_M \end{pmatrix}\begin{pmatrix}\psi \\ \psi^c\end{pmatrix} \tag{1.6}$$

If one diagonalizes this matrix, it will have two real mass eigenvalues of $m_D \pm |m_M|$. If $m_M = 0$, then the mass Lagrangian is already diagonal and we are left with a single degenerate eigenvalue, m_D, whose eigenvectors are not charge conjugation eigenstates. This state of affairs is called a Dirac neutrino. If m_M is nonzero then the eigenvalues are charge conjugation eigenstates and the result is a Majorana neutrino.

To get a more intuitive feel for the difference between a Dirac and Majorana neutrino, it is instructive to consider the successive actions of a Lorentz boost and a CPT transformation on a neutrino with negative (left-handed) helicity, see Figure 1.13.

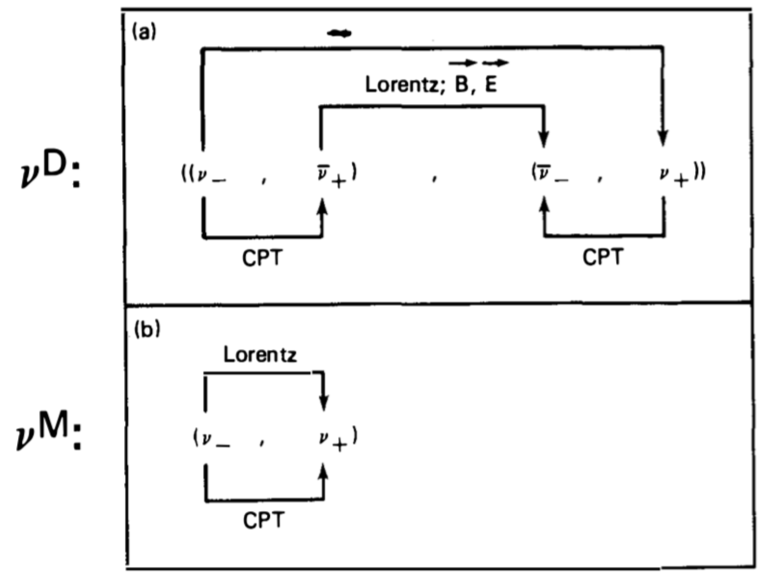

Figure 1.13: Successive CPT and Lorentz transformations applied to Dirac (top) and Majorana (bottom) neutrinos. Figure from [52].

The Dirac neutrino is not a charge conjugation eigenstate, so the operation of C takes ν to $\bar{\nu}$ and vice-a-versa. Parity reverses the sign of velocity but not the spin of the neutrino, and time reversal flips both velocity and spin. Thus, CPT takes the neutrino to its antiparticle (and vice-a-versa) and flips its helicity. Working under the assumption of massive neutrinos which travel slower than the speed of light, it is theoretically possible to Lorentz boost the observer to an inertial reference frame where the velocity of the neutrino is reversed in sign. However, spin remains the same in the boosted frame, so a Lorentz boost takes the neutrino (antineutrino) to a neutrino (antineutrino) of opposite helicity. One can see from Figure 1.13 that the Dirac neutrino requires four nonequivalent states.

The Majorana neutrino is a different story. A Lorentz boost has the same effect as it does in the case of the Dirac neutrino. However, because the Majorana neutrino is a charge conjugation eigenstate[1], the operation of parity takes ν to ν. Thus, CPT takes the left-handed neutrino to a right-handed neutrino, indicating that a Majorana neutrino is its own antiparticle with the addition of a helicity reversal. In this light, $0\nu\beta\beta$ can be interpreted as the exchange of a virtual neutrino between two W^- bosons; this process violates lepton number by two. Though virtual neutrino exchange is the most popular $0\nu\beta\beta$ mechanism, there are other possible mechanisms. As a consequence of Schechter and Valle's "black box theorem" [53], it is known that lepton number is violated regardless of the mechanism. So observation of $0\nu\beta\beta$ indicates definitively that the neutrino is a Majorana fermion.

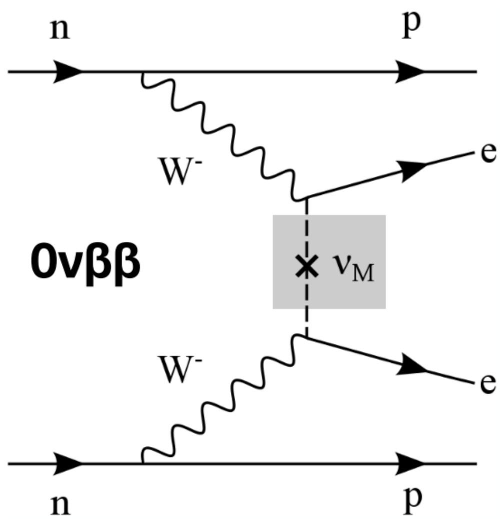

Figure 1.14: Feynman diagram of $0\nu\beta\beta$ with virtual neutrino exchange. Figure from [54].

The lepton number violation of $0\nu\beta\beta$ suggests that leptogenesis could have played a role in the matter-antimatter asymmetry in the universe [55] [56]. The CP violating phase α, picked up by the Majorana neutrino due to its failure to obey the global phase transition in Equation 1.5, could contribute to the total amount of CP violation required by the Sakharov conditions for baryogenesis [57]. Baryogenesis refers to a set of models that attempt to create a matter-antimatter asymmetry from an initially symmetric universe through the framework of elementary particle physics, see [56] [58] and references therein.

[1]This is technically only true for a free Majorana fermion. A Majorana neutrino involved in $0\nu\beta\beta$ experiences the weak interaction, which violates charge conjugation.

The half life for $0\nu\beta\beta$ is given by:

$$(T^{0\nu}_{1/2})^{-1} = G_{0\nu}(Q_{\beta\beta}, Z)|M^{0\nu}|^2 \langle m_{\beta\beta}\rangle^2 \tag{1.7}$$

where $G_{0\nu}$ is a kinematic phase space factor, $M^{0\nu}$ are the nuclear matrix elements for the transition between parent and daughter nucleus, and $m_{\beta\beta}$ is the effective Majorana mass of the electron neutrino.

Atmospheric neutrino experiments have determined the magnitude but not the sign of Δm^2_{23}, the difference between mass eigenstates m_2 and m_3. This results in two different hierarchies for the mass eigenstates: one where $m_3 > m_2$ (normal) and one where $m_3 < m_2$ (inverted), see Figure 1.15. Figure 1.16 shows a plot of $\mathrm{m}_{\beta\beta}$ versus lightest neutrino mass, which could be either m_1 or m_3. By placing a limit on the $0\nu\beta\beta$ half life, it is possible to constrain $m_{\beta\beta}$. With enough sensitivity, $0\nu\beta\beta$ experiments hope to be able to probe the entire portion of this parameter space unique to the inverted and hierarchy. If no discoveries are made in this region, it would rule out the inverted hierarchy.

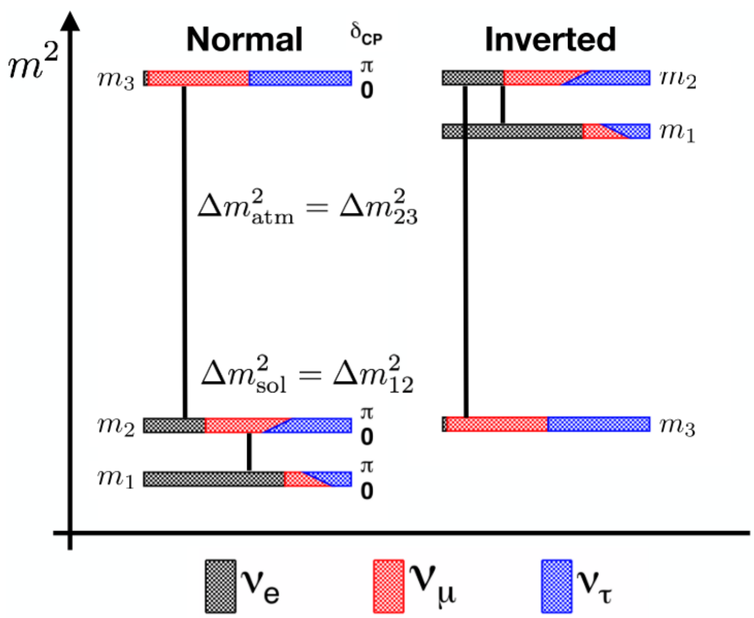

Figure 1.15: Normal and inverted neutrino mass hierarchy. Figure from [54].

The DEMONSTRATOR has produced limits [60] [61] on $0\nu\beta\beta$ in the isotope ^{76}Ge, the

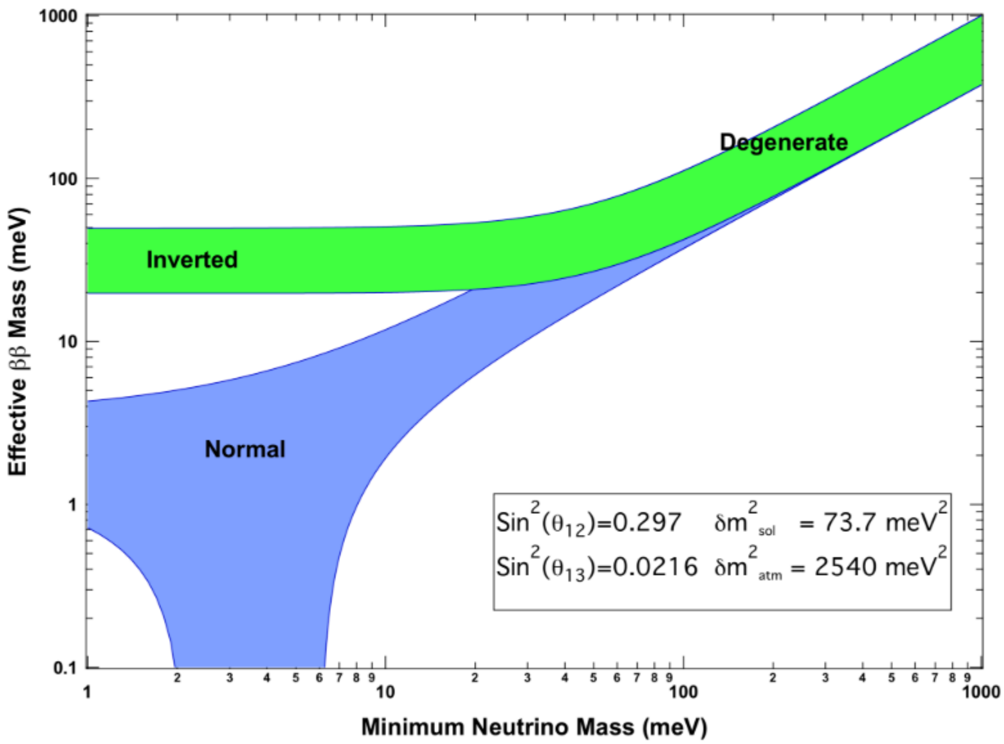

Figure 1.16: Lightest ν mass vs. $m_{\beta\beta}$. Figure from [59].

most recent of which is $T^{0\nu}_{1/2} > 2.7 \times 10^{25}$ yr. Because $0\nu\beta\beta$ is an extremely slow process, it is necessary to build experiments that are very low in background. Figure 1.17 shows the discovery potential of $0\nu\beta\beta$ in ^{76}Ge as a function of exposure (the product of active mass and livetime) for a background free configuration and for various background rates near the 2039 keV region of interest. The DEMONSTRATOR's lowest background configuration was 4.0 ± 2.0 cts/(FWHM · t · yr) [60]. The MAJORANA and GERDA collaborations have formed the core of a new collaboration called LEGEND [59] which is building a $0\nu\beta\beta$ experiment at Laboratori Nazionali del Gran Sasso in Italy that will operate 200 kg of germanium at a background goal of $B < 2 \times 10^4$ cts/(keV · kg · y). The ultimate goal of LEGEND is to build a 1-tonne experiment. MAJORANA, GERDA, and LEGEND are three among many experiments that are probing $0\nu\beta\beta$ in a variety of isotopes. For a theoretical and experimental review of $0\nu\beta\beta$, the author is referred to [62] [63] [64] and the references they contain.

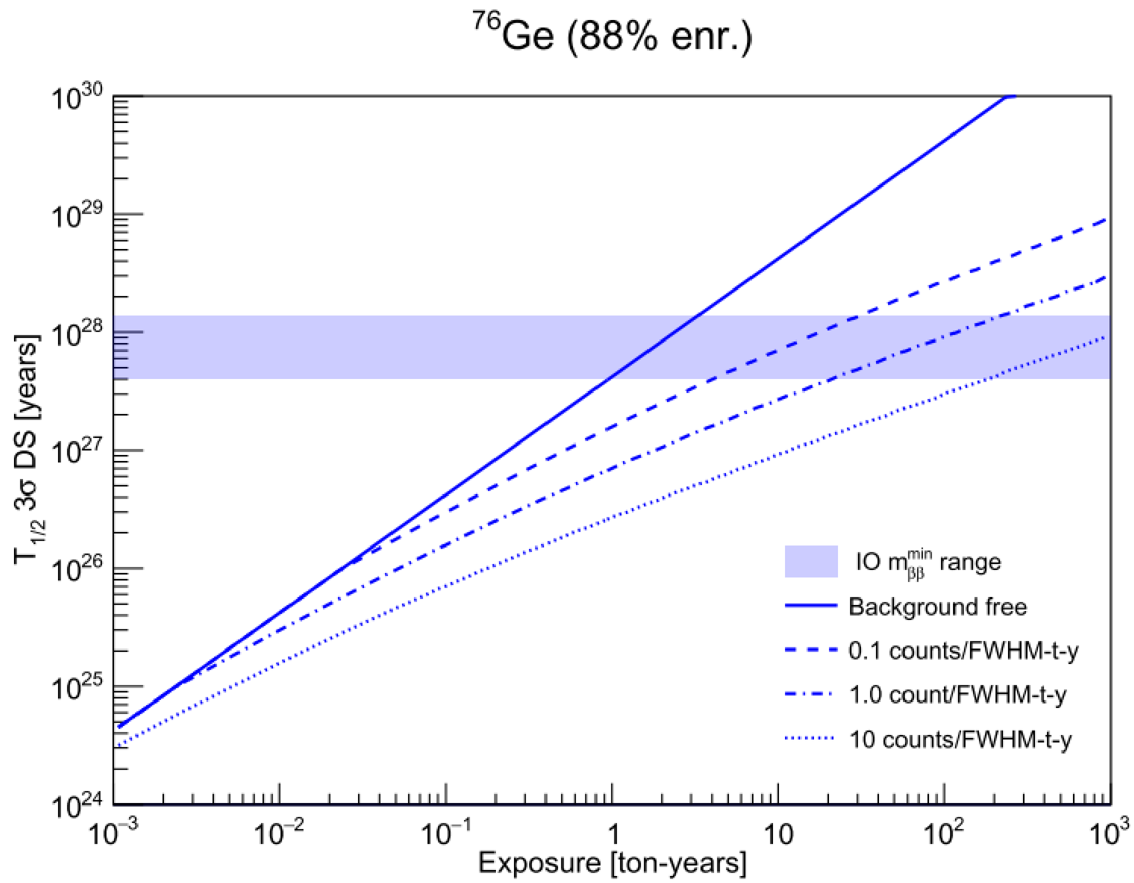

Figure 1.17: 90% discovery potential for ^{76}Ge. Figure produced by J. Detwiler.

CHAPTER 2: The Majorana Demonstrator

Since no neutrinos are emitted in $0\nu\beta\beta$ (see Figure 1.14), the full energy of the decay is carried away by the two electrons emitted. Because of this, the expected signal is a monoenergetic peak at the Q-value of the decay. Since the signal is a peak, there is much benefit in choosing a detector medium with good energy resolution, like high purity germanium detectors (HPGe's). The DEMONSTRATOR uses arrays of HPGe's, with 29.7 kg of 88% enriched in ^{76}Ge crystals as both the source and detector medium, and 14.4 kg of natural germanium crystals that are used for background rejection. The Q-value of $0\nu\beta\beta$ in ^{76}Ge is 2039 keV. There are a number of backgrounds relevant to the 2039 keV region of interest, and each one motivates the design of the DEMONSTRATOR in some way. To reduce cosmic ray flux, the DEMONSTRATOR was built deep underground at Sanford Underground Research Facility. Neutrons from the rock walls in the lab and environmental gammas require shielding. Since the laboratory facility is underground, radon is an issue and must be dealt with. Exposure to cosmic rays can create radioactive, cosmogenic contaminants in both the detectors and the hardware components closest to the detectors, so special handling and fabrication procedures must be followed. Great care must be taken to minimize contaminants from the uranium and thorium decay chains by careful selection of materials and high cleanliness standards. Each of these design aspects are discussed in this chapter.

Like $0\nu\beta\beta$, the expected signal for bosonic dark matter is a monoenergetic peak. The super-weak interaction cross sections involved means that the observed signal would be quite weak. Because of these facts, a search for bosonic dark matter benefits from the use of a low background experiment with excellent energy resolution. So while the MAJORANA DEMONSTRATOR was originally built as a $0\nu\beta\beta$ detector, it also makes an ideal platform for detecting bosonic dark matter.

Section 2.1: SURF and Infrastructure

The MAJORANA DEMONSTRATOR is located at Sanford Underground Research Facility (SURF) [65] in Lead, South Dakota, named in honor of the private donor T. Denny Sanford. SURF utilizes the infrastructure of the former Homestake gold mine. The majority of MAJORANA's activity takes place in SURF's Davis Campus, 4850' under the surface, a map of which is shown in Figure 2.1. The rock overburden at the 4850' level shields the DEMONSTRATOR from cosmic rays and is equivalent to 4290 m of water shielding. The muon flux at 4850' is reduced to $(5.31 \pm 0.17) \times 10^{-9}$ /s/cm^2, as compared to 2.0 ± 0.2 /s/cm^2 on the surface [66].

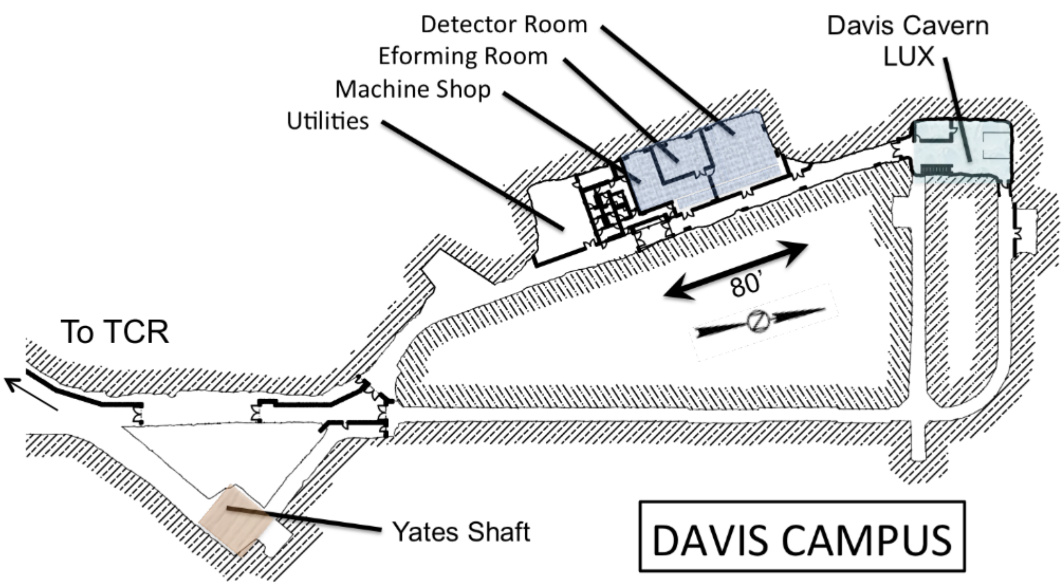

Figure 2.1: A map of the Davis Campus at the 4850' level of SURF. The areas shaded blue and green are the MAJORANA and LUX [28] clean laboratory spaces respectively. The bottom left of the image points in the direction of the TCR facility where copper electroforming took place. Figure from [67].

The Davis Cavern is the cite of the Nobel-prize winning Ray Davis solar neutrino experiment [68], and is also the location of the LUX [28] dark matter experiment, which is being upgraded into the LZ experiment [69]. The Davis Campus is partitioned into the dirty side, which includes the Yates shaft and the mine drifts, and the clean side which contains the laboratory spaces. The clean side contains the MAJORANA machine shop, which is maintained as a class 5000 cleanroom and is where many of the structural components in the DEMONSTRATOR were fabricated from ultrapure, electroformed cooper (EFCu) and clean plastics. The electroformed copper is grown at the TCR facility, also on the 4850' level but not a part of Davis Campus. More details about the EFCu program and clean plastics are given in Chapter 2.5. The Detector Room is a class 1000 cleanroom and is where the DEMONSTRATOR itself is located. A panorama of the Detector Room is shown in Figure 2.2

Prominent features in the panorama, from bottom to top, are the data acquisition system (DAQ), a monolith containing a module of detectors about to be inserted into the shield, the electronics racks, and the glove boxes. The glove boxes are where the HPGe's are assembled into detector units (Figure 2.3), where detector units are stacked into strings (Figure 2.4), and strings are inserted into modular cryostats (Figure 2.5). The glove boxes are kept at a higher cleanliness level than the Detector Room, and a particle counter inside the glove boxes is used to monitor the amount of fine, airborne particulates whenever any work involving the germanium detectors takes place. The glove boxes are also purged with liquid nitrogen (LN) boil-off to protect the detectors from exposure to radon.

Section 2.2: Compact Shield

A cross section of the DEMONSTRATOR's compact shield is shown in Figure 2.6, and Figure 2.7 contains a CAD rendering of the whole DEMONSTRATOR assembly for scale. The outer layer is composed of borated polyethylene which shields neutrons from the cavern's rock walls. Inside the neutron shield are 2.54 cm thick scintillating acrylic sheets. These scintillators allow the analyst to reject the few muons that survive the rock overburden by looking for hits in the veto pannels that coincide with hits in the germanium detectors. Within the muon veto is approximately 54 tons of stacked lead bricks; the thickness of the lead shield is 45 cm. Finally, the inner-most layer of the shield consists of 2" of electroformed copper (described in Chapter 2.5) surrounded by 2" of commercial copper. The copper shields radioactivity from the lead bricks. The lead and copper shields are enclosed within a box

Figure 2.2: A panorama of the MAJORANA detector room showing, from left to right, the DAQ, a module prepared for insertion into the shield, the electronics racks, and the glove boxes.

Figure 2.3: A detector unit containing a germanium detector, cooper and plastic support structures, and preamplifier front end.

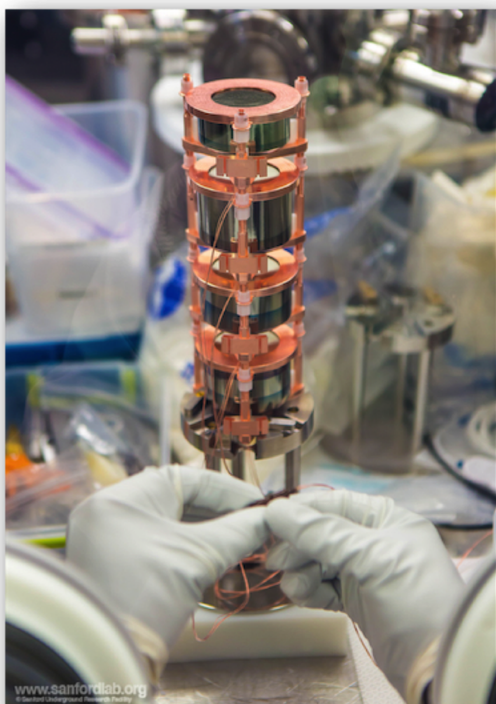

Figure 2.4: A worker assembles a string of detector units and tests the health of the preamplifier front end for one of the detector units.

Figure 2.5: A worker installing strings of detectors in an opened cryostat.

that is continuously purged with liquid nitrogen boil-off to remove radon. For further details about the Demonstrator's shield, see [70].

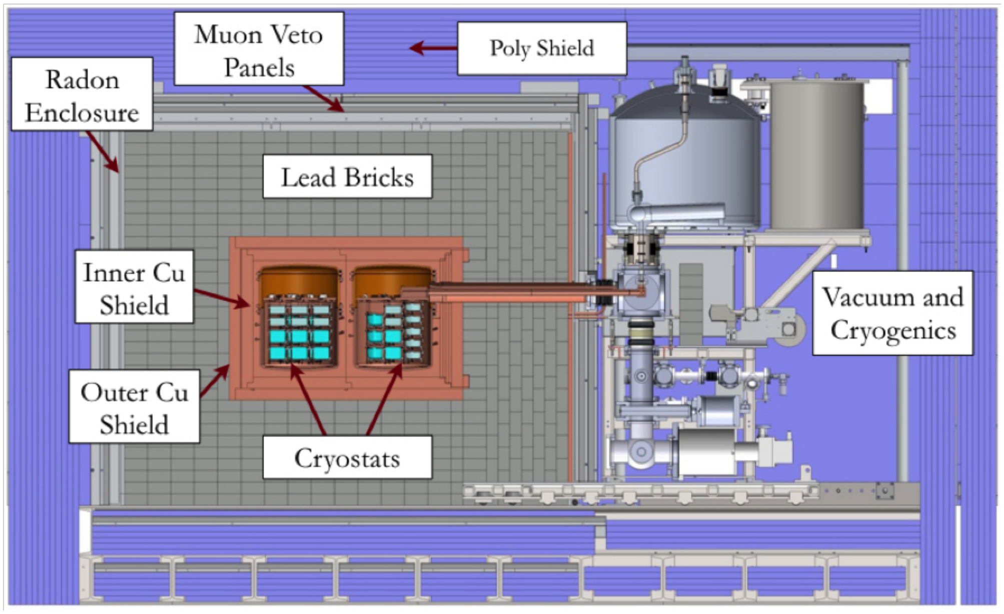

Figure 2.6: A cutaway of the Demonstrator's compact shield design showing the neutron poly shield, the active muon veto, the radon enclosure, the lead shield, and the inner/outer copper shield. On the right side of the image is a module consisting of a cryostat, cross arm tube, electronics box housing the preamplifier electronics, and cryogenic/vacuum service hardware docked in the shield. The entire module is enclosed within the poly shield.

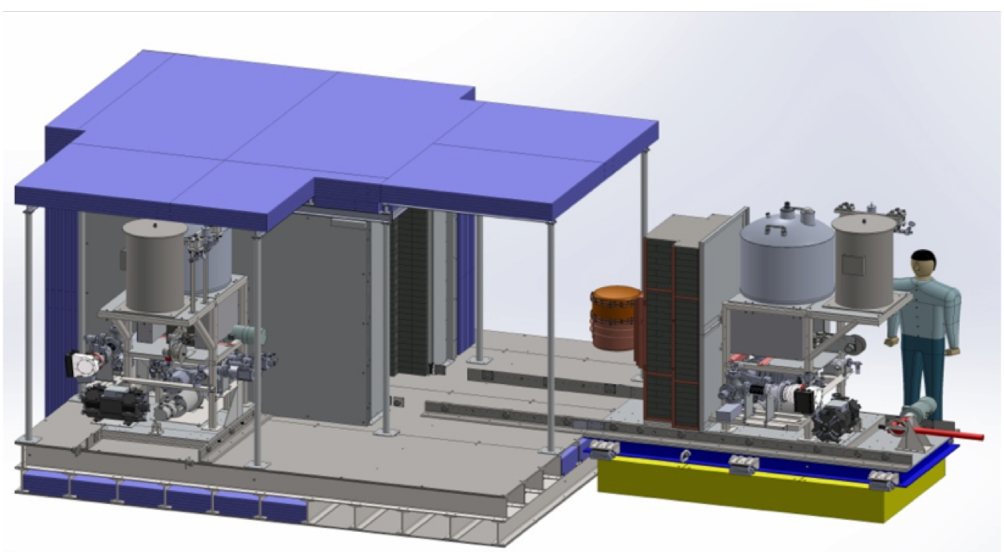

Figure 2.7: A CAD rendering of the entire Demonstrator assembly, showing a module ready for insertion into the compact shield and a CAD person for scale.

Section 2.3: Modules

HPGe's are deployed as strings within two cryostats. Each cryostat contains approximately 22 kg of germanium detectors deployed in seven strings of detector units. The cryostats are electroformed copper vacuum enclosures that include electron-beam-welded vessel assemblies along with removable tops and bottom lids. Detector strings are mounted to a copper coldplate inside the cryostat. The coldplate rests on Vespel pins that provide support and alignment while maintaining a thermal break from the room temperature cryostat. The signal and high-voltage lines from the detectors are routed to the cable management system, which sits on top of the coldplate. An infrared (IR) shield is mounted to the underside of the coldplate to reduce detector leakage current generated by IR radiation. The coldplate attaches to a thermosiphon [71], and the thermosiphon travels down the cross arm tube to interface with the cryogenic system. Liquid nitrogen is used to cool the detectors via the thermosiphon. The cross arm tube attaches to the cryostat and provides a path for vacuum pumping and cables. The cross arm tube makes a transition to stainless steel conflat vacuum hardware at its far end via a copper/stainless explosion-bonded transition flange. All of the stainless steel vacuum and cryogenic hardware, as well as the electronics box housing the preamplifiers, is located outside of the Demonstrators passive shielding (the copper and lead). Figure 2.8 shows a CAD rendering of the cold side and warm side hardware associated with a module. This hardware rests on top of a monolith which can be moved between the gloveboxes, where string insertion and cryostat assembly takes place, to the keyed opening in the compact shield where the cryostat is inserted into the inner copper shield. Figures 2.2 and 2.9 show a monolith about to be inserted into the shield. Figure 2.10 shows a keyed opening in the lead and copper shield where a module docks.

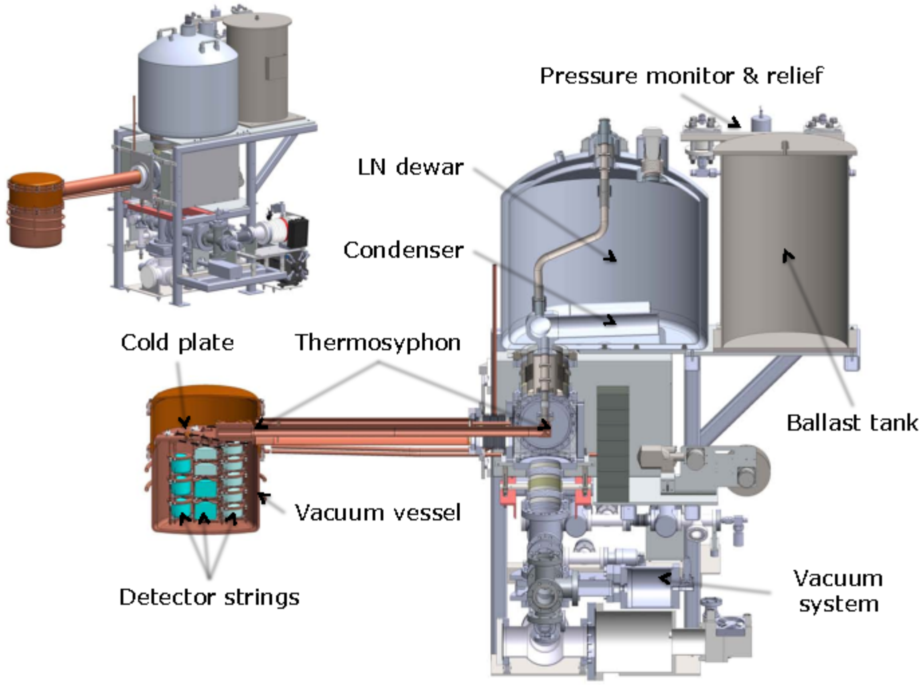

Figure 2.8: CAD rendering of the hardware associated with a module. Shown are strings of HPGe's, a cryostat, a cross arm tube, a thermosiphon, a coldplate, and the cryogenic/vacuum hardware.

Figure 2.9: A monolith whose sealed cryostat has been removed from the glove boxes and is being prepared for insertion into the compact shield in the background. The plastic tube wrapped around the cryostat is the calibration track where calibration line sources are inserted.

Figure 2.10: The lead and copper shielding without the muon veto or poly panels, showing one of the two keyed openings for docking a module.

Section 2.4: Data Acquisition (DAQ) and Data Pipeline

Figure 2.11 contains a high level view of the readout electronics. The DEMONSTRATOR utilizes a resistive-feedback preamplifier design. The first stage begins with a low mass front end (LMFE) which interfaces directly with the detector. The LMFE consits of a JFET in parallel with a feedback resistor and feedback capacitor. The feedback resistor is formed by sputtering a layer of amorphous germanium onto a board substrate of fused silica, and its resistance is approximately 10-100 GΩ at cryogenic temperatures [70]. The feedback capacitance of 0.2 pF [72] is formed by the stray capacitance between traces on the front end. An example of an LMFE is shown in Figure 2.12.

LMFE's have the advantage of being a low noise, low radioactivity design. They are installed close to the detectors in order to minimize stray input capacitance that would otherwise contribute to noise. The FET is a bare Moxtek MX-11 JFET low-noise die with very low-input capacitance of about 0.7 pF [72]. A prototype front-end tested without detector load reached a minimum noise level of 55 eV FWHM [72]. The substrate of fused silica was chosen for its high radiopurity. The board was made with high purity, electroformed copper, which will be described in more detail in Chapter 2.5. The sputtered feedback resistor is made of high purity germanium. Al-Si bonding wire and clean silver epoxy are used to connect the JFET die and coaxial cables to the traces. By using the stray capacitance between traces on the front end, we avoided loading the board with unnecessary components.

The LMFE's are DC coupled to the preamplifier first stages outside of the cryostat via long cables that run through the cross arm tube. The warm preamplifier first stages are AC coupled to the second stages. The preamplifiers are organized by string position on motherboards outside the cryostats. On the motherboards, each detector has a low-gain and a high-gain dual signal output for digitization. Each of these outputs is assigned a channel number such that even numbers correspond to high-gain and odd numbers correspond to low-gain. Detectors will be referenced by their channel number later in this dissertation. It is also common practice within the collaboration to reference detectors by their position within the cryostats. For example, C1P2D3 refers to the third detector from the top, in the second string of the first cryostat. The preamp channel notation and CPD notation are often used interchangeably.

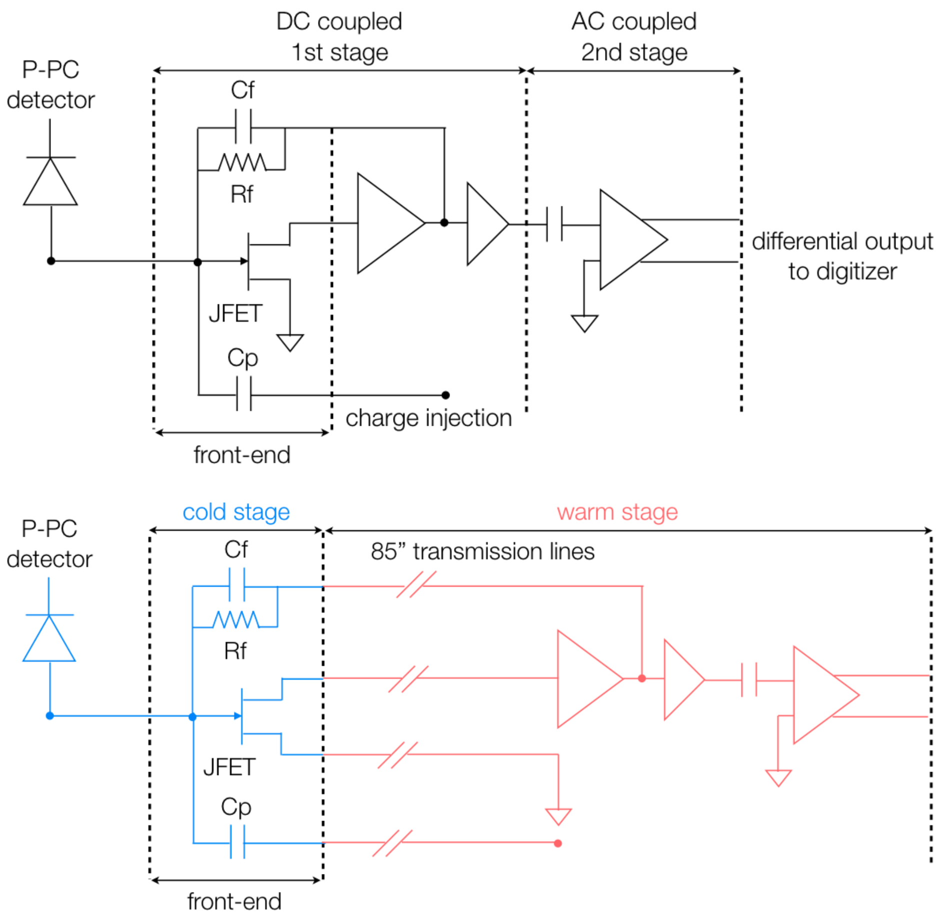

Figure 2.11: The DEMONSTRATOR's resistive-feedback charge-sensitive preamplifier. Top: A simplified picture that distinguishes the first stage from the second stage. Bottom: The actual setup with front end (LMFE) operated at cryogenic temperatures and long transmission lines that run through the cross arm tube. Figure from [72].

The digitizers are GRETINA cards that were developed originally for the GRETINA collaboration [73]. These cards are combination digitizers and FPGA-based digital signal processors, which perform digital trapezoidal shaping and pole-zero correction for online energy calculation. Trapeziodal filters are described in Chapter 2.9. GRETINA cards have 10 channel inputs, are housed within a VME [74] crate, and controlled by a single board computer that also sits within the crate. The signals that are digitized and shaped are

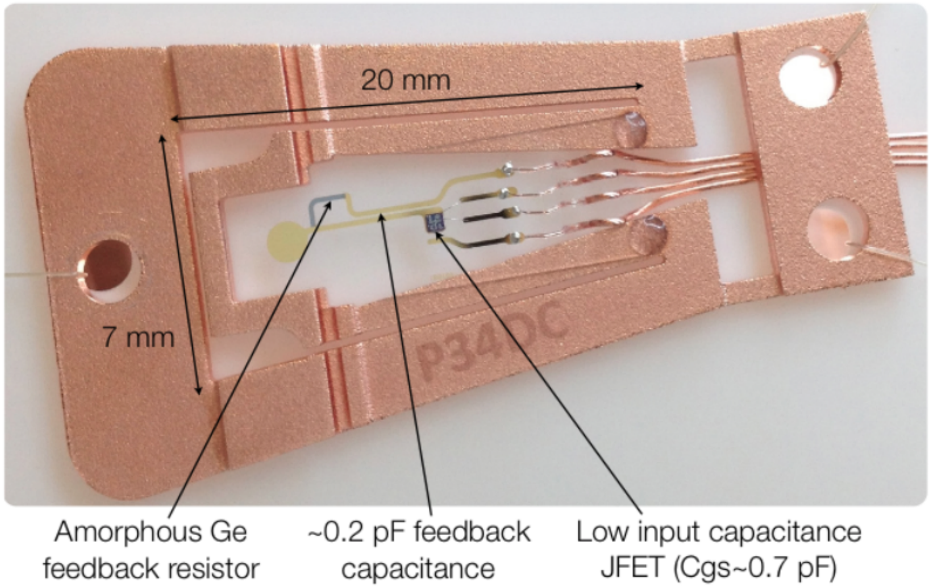

Figure 2.12: A closeup of the first stage front end, or LMFE, showing the feedback resistor, feedback capacitance, and JFET. Figure from [72].

integrated charge signals from the HPGe's rather than current signals. These signals will be explained in Chapter 2.8.

Communication between all components of the DAQ are controlled by ORCA [75]. ORCA is a general purpose, highly modular, object oriented data acquisition and control software. ORCA can be configured at run time into different hardware configurations and data read-out schemes by dragging and dropping items from a catalog of objects into a configuration window through the graphical user interface. This makes ORCA a highly versatile and adaptable system. Each object in ORCA is composed of its own fully encapsulated data structures as well as support and diagnostic code.

Data collection is separated into hour-long runs, except for when the run file exceeds 2 GB as frequently happens with the high data rates in calibration runs. In these cases, the run file is truncated. Data is temporarily stored on a RAID array on site before being transfered to computing clusters at the National Energy Research Scientific Computing Center (NERSC) at Lawrence Berkeley National Laboratory [76]. The data is further subdivided into data sets, corresponding to different physical configurations of the Demonstrator's history.

The very first data set, denoted DS0 (data set zero), was the commissioning data taken with incomplete shielding and temporary, high activity cryostat seals. This data was used to produce the DEMONSTRATOR's first limits on bosonic dark matter [77]. The analysis in this dissertation will utilize seven data sets which are numbered DS1, DS2, DS3, DS4, DS5b, DS5c, DS6a respectively. By the time data taking started for DS1, the shielding had been completed but only one module was inserted. Both modules were in the shield by the time data taking started for DS3 and DS4. These two data sets were taken simultaneously, with DS3 accounting for data from one module and DS4 accounting for data from another. DS5a was the first data set where the DAQ was integrated, so this data set contains data from both modules. However, this data set will be omitted due to excessive rates of transient noise. Transient noise will be discussed in Chapter 3.6. DS5C is the when the blindness scheme was implemented. A blinded analysis was used for the DEMONSTRATOR's second result on $0\nu\beta\beta$ [61], but this analysis only considers open data. Appendix A contains a table of these data sets, the dates over which they were taken, the amount of enriched and natural detector mass that was active during the data set, and the amount of enriched and natural exposure. Exposure is the product of active mass and the livetime over which the detector was actively taking data. The table excludes the most recent two data sets, DS6b and DS6c (ongoing) because they are not considered in this analysis, as well as calibration data. Active mass and exposure numbers are taken from [78]. Throughout data taking, roughly a third of the detectors were inoperative. The two leading causes for detectors being inoperative were due to connectivity issues with the signal and high voltage lines. Much ongoing research and development work is being invested in improving cables and connectors.

Section 2.5: Ultra-clean Materials

The components closest to the detectors were made with materials that were carefully selected for high purity and low radioactivity. Copper was selected as the key structural component in the inner shielding, cryostats, and all detector mounting hardware because it contains no naturally occurring radioactive isotopes [79]. However, ^{60}Co can be created cosmogenically in copper. To solve this problem, all copper components, with the exception of the outer copper shield, were machined out of copper electroformed underground at the temporary cleanroom (TCR) facility at the 4850' level of SURF. A small ammount of copper was electroformed at shallow site at Pacific Northwest National Laboratory. Machining of the electroformed copper (EFCu) took place at the clean machine shop located at the Davis Campus. This machine shop was restricted to clean copper, plastics, and approved stainless steel; the only cutting fluids used were water based lubricants and deionized water [79]. In addition to reducing cosmogenics, the other major benefit to MAJORANA's clean copper program is that the electroformed copper is lower in contaminants from the uranium and thorium decay chains, which are primordial in origin, than commercial copper. The work flow for the EFCu is partially highlighted in Figure 2.13.

The plastic used for detector supports in the detector units was a pure polytetrafluoroethylene (PTFE), DuPont Teflon NXT-85. Weight bearing plastic components requiring higher rigidity used pure stocks of PEEK (polyether ether ketone), produced by Victrex, and Vespel, produced by DuPont. Thin layers of low-radioactivity parylene were used as a coating on copper threads to prevent galling, as well as for the cryostat seal. Chapter 2.4 described the low background materials used to make the LMFE's. Detector contact is made via an electroformed copper pin with beads of low-background tin at either end. Signal high-voltage cables are extremely low-mass miniature coaxial cables. The MAJORANA collaboration worked with the vendor to cleanly fabricate the final product using pure stock that MAJORANA provided for the conductor, insulation, and shield. Cable connectors within the cryostat are made from electroformed copper and Vespel. In order to achieve high levels of radiopurity in the materials, it was necessary to develop precision radioassay capabilities [80] [81] [82] as well as procedures for cleaning surface contamination from components [83] [84] [85] [86].

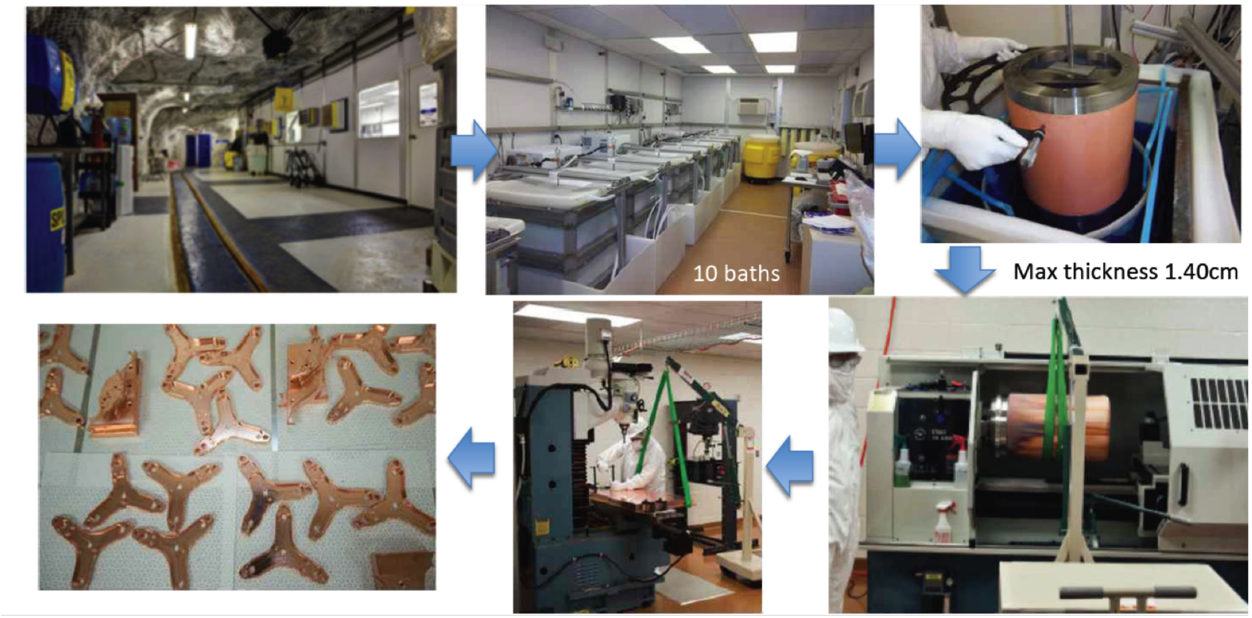

Figure 2.13: Left Row: The ultra-pure copper is grown onto mandrels at the TCR facility on the 4850' level of SURF. Right Top/Middle: Machining of electroformed copper at Davis Campus machine shop. Bottom Right: Structural components of the detector strings machined out of electroplated copper.

Section 2.6: Processing of the Germanium Detectors

When the germanium material used to fabricate the Demonstrator's detectors is exposed to cosmic rays at the surface, it creates radioactive contaminants in the material. Several common mechanisms for cosmogenic activation are spallation of nuclei by high energy nucleons, fragmentation, and induced fision [87]. One such isotope, tritium, has recently been observed in germanium [88][26][89][90]. It's half life is 12.32 years [91], meaning that it will be present for the duration of the Demonstrator's lifetime. Tritium is a beta emitter and its spectral feature in the Demonstrator is a continuum with an endpoint energy of 18.6 keV, see Figure 3.2. Three additional cosmogenic impurities observed in the Demonstrator are ^{51}Cr, ^{55}Fe, ^{65}Zn, and ^{68}Ge. These isotopes decay by k-shell electron capture and manifest as monoenergetic peaks at 5.5 keV, 6.5 keV, 8.9 keV, and 10.36 keV respectively. Cosmogenic backgrounds are irreducible and only diminish as the respective isotopes decay away. For this reason, special precautions were taken in the production and handeling of the detectors enriched in ^{76}Ge to minimize cosmogenic activation [90]. Isotopic enrichment of the germanium material was performed by the Joint Stock Company Production Association Electro-chemical Plant (ECP) in Zelenogorsk, Russia; the product of this enrichment process was in the form of GeO_2. Immediately after production, the GeO_2 was stored under an overburden of concrete, steel, and soil. The GeO_2 was delivered to Oak Ridge, TN, United States, in two shipments. The first 20 kg was delivered in September 2011, and the second in October 2012. Rather than flying, ground transport and shipping were used in order to keep the material at the lowest elevation possible and reduce cosmic ray exposure. The material was moved in a special, cylindrical steel container designed and built in Russia, featuring 72 cm of steel above the material and 43 cm on the sides. According to calculations by Barabanov et al., the shield reduced the cosmogenic production of ^{68}Ge by approximately a factor of 10 [92]. At Oak Ridge, the material was stored underground in space rented at the bottom of Cherokee Caverns with a 40 m rock overburden. Processing of the material by Electrochemical Systems Inc. (ESI) involved reducing the GeO_2 into metal powder, melting the powder down, and then zone refining. Finally, AMETEK-ORTEC Inc. performed a final round of zone refining, pulled the refined material into crystals via a Czochralski crystal puller, and manufactured the crystals into high high purity germanium detectors. When not being processed by ESI or AMETEK-ORTEC, the germanium was stored underground in Cherokee Caverns. Further details are described in the Demonstrator's germanium processing paper [90].

Section 2.7: Background Budget

Figure 3.4 shows the Demonstrator's background budget. The radioactivity from materials is the dominant component. Also included are contributions from the small amount of cosmogenic activation in the germanium and copper, from environmental sources of radiation like external gammas and radon daughters, and muon induced backgrounds. An upper limit on the negligible background from atmospheric and other neutrinos is shown in orange. The background budget is known to be incomplete. In March of 2018, MAJORANA set a lower limit on the $0\nu\beta\beta$ half in ^{76}Ge of 1.9×10^{25} yr (90% C.L.) with 9.95 kg $\cdot$ y of exposure from enriched detectors and a background of 4.0 ± 2.0 cts/(FWHM $\cdot$ t $\cdot$ yr) in the lowest background configuration [60]. This result only utilized open data. In June of the same year, MAJORANA opened its blinded data and released an updated half life limit of 2.7×10^{25} yr (90% C.L.) with an exposure of 26 kg $\cdot$ y from enriched detectors and a background rate of 11.9 ± 2.0 cts/(FWHM $\cdot$ t $\cdot$ yr) in the lowest background configuration [61]. This this additional background from the blinded data was unexpected, and is hypothesized to come from an unknown source of ^{208}Tl contamination.

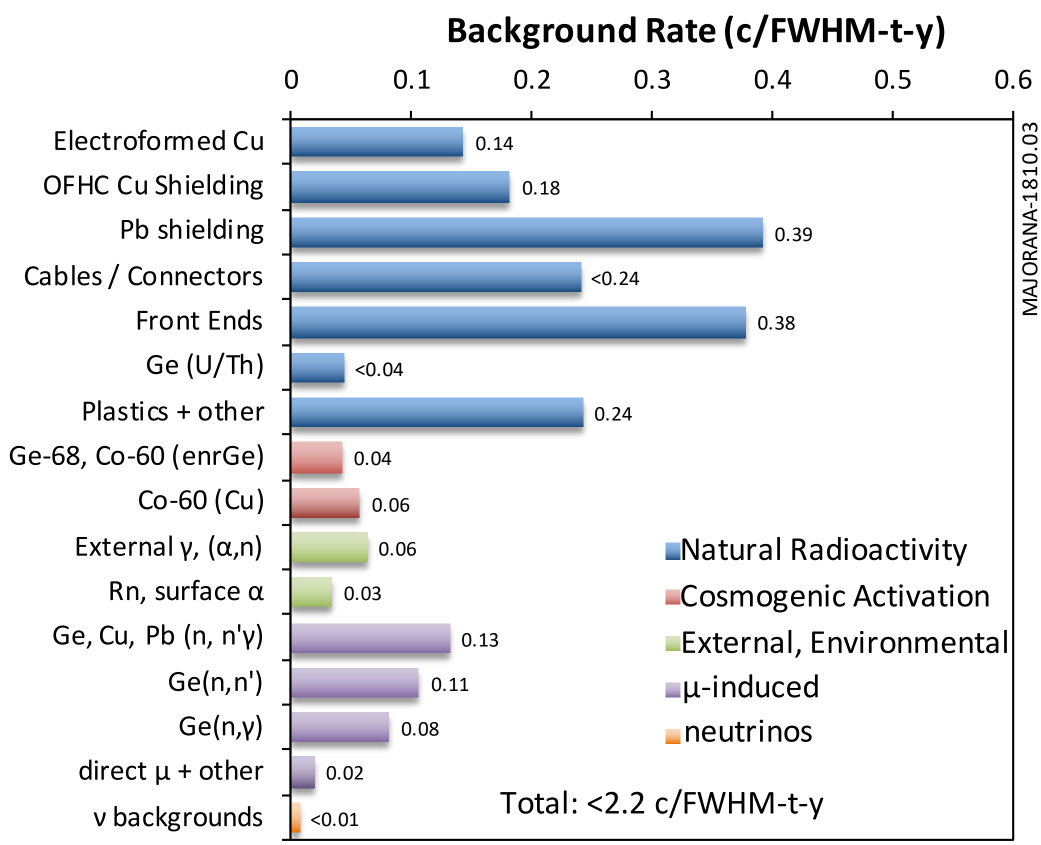

Figure 2.14: The background budget of the MAJORANA DEMONSTRATOR. Though the electroformed copper is extremely radiopure, the fact that it composes most of the structural materials close to the detectors means that its trace amount of radioactivity contributes a nontrivial component of the total background budget. Figure provided by V. Guiseppe.

Section 2.8: Basics of the Germanium Detectors

The heart of the DEMONSTRATOR is its arrays of PPC style HPGe detectors, where PPC stands for p-type point contact. Figure 2.15 shows a cutaway graphic of one of the two types of PPC detector used in the DEMONSTRATOR. The bulk material of a PPC is p-type semiconductor, which means the bulk germanium contains more acceptor impurities (or "holes") than donor impurities. The anode, which surrounds the majority of the surface of the detector, is n+ type and is heavily doped to contain more donor than acceptor impurities (or free electrons). This is accomplished by diffusing the surface of the detector with lithium, creating a 500 μm - 1 mm thick dead layer. The point contact, or cathode, is made by boron implantation and is much thinner, on the order of 0.3 μm. The contact of the n+ layer with the p-type bulk forms a p-n junction. As holes from the p-type material diffuse into the n+ material and free electrons from the n+ material diffuse into the p-type material, a depletion region is formed with an electric field from the ionized lattice. This depletion region can be made to span the entire length and width of the crystal by applying a potential difference, typically a few kV, across the anode and cathode.

PPC's have been used in a variety of experiments [31] [93] [94] [95], but the most popular configuration for germanium detectors is the coaxial design, see Figure 2.16. The capacitance of most PPC's is significantly lower than that of most coax detectors, with a typical capacitance for a PPC at around 1 pF compared to 20 pF for a typical coaxial detector [96]. The lower capacitance results in lower levels of electronic noise, which has a number of benefits for low energy physics analyses such as bosonic dark matter. First of all, lower levels of electronic noise allow for signal detection at lower energies. The energy threshold for this analysis is 5 keV, though some analyses related to the DEMONSTRATOR have pushed down to lower energies [54]. By comparison, a typical energy threshold for coax detectors is around 40 keV [97].

The second benefit that comes from lower electronic noise is superior energy resolution at low energies. The energy resolution of a radiation detector is its ability to resolve peaks

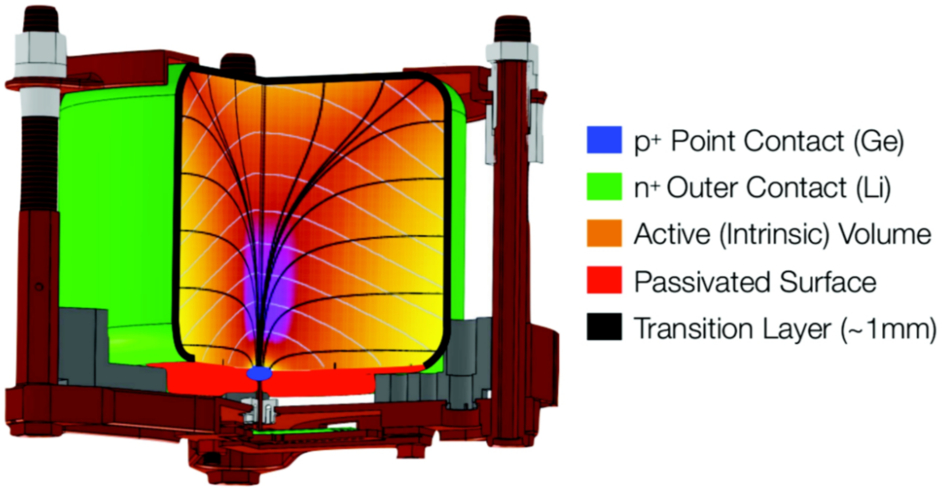

Figure 2.15: A graphic of a PPC detector within a DEMONSTRATOR detector unit. The n+ anode is in green and makes electrical connection with the high-voltage ring on top of the detector. The point contact cathode is the blue dot at the bottom of the detector, from which the signal is read out by a pin. The heat map shows the maximum velocity of drifting charges. Black curves are charge drift trajectories and gray contours are isochrones. Between the active mass and the n+ dead layer is the transition region, or diffusion dominated region. Figure courtesy of B. Shanks and T. Caldwell.

that are close in energy to each other. In a physics analysis that involves a search for a mono-energetic peak, such as bosonic dark matter or $0\nu\beta\beta$, good energy resolution creates a smaller region of interest (ROI). A smaller ROI reduces the impact of background and improves the sensitivity of the measurement. Resolution is often expressed as the full width half maximum (FWHM) versus energy. Sometimes σ is used instead of FWHM, which is equivalent to FWHM/2.355 if the peak is Gaussian. The most commonly quoted formula for the energy resolution of germanium detectors is given by Equation 2.1.

$$\sigma_E(E) = \sqrt{\sigma_\epsilon^2 + \langle\epsilon\rangle FE + c^2E^2} \tag{2.1}$$

where σ_ϵ is the contribution from electronic noise, $\epsilon = 2.96$ eV is the energy required to produce an electron-hole pair in germanium, the Fano Factor F characterizes the fluctuations in the number of electron-hole pairs produced by an incoming gamma ray in germanium, and c is related to charge trapping. At low energies, the terms from electronic noise and charge trapping dominate; at high energies, the charge carrier statistics is more important. Because

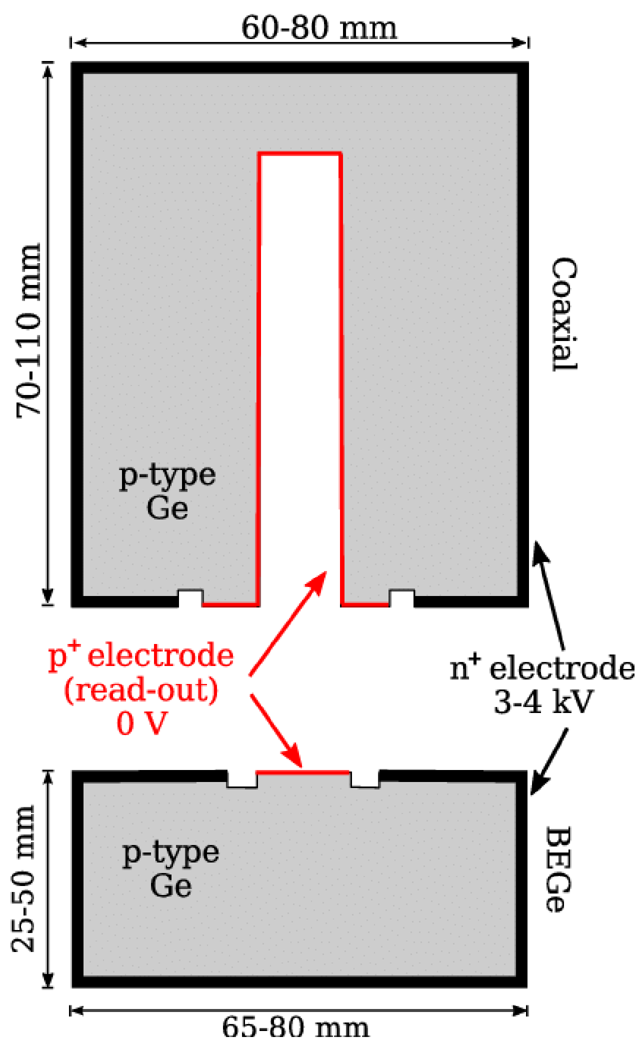

Figure 2.16: Comparison of the cross sections of representative PPC and coaxial germanium detectors. The cathode for the PPC detector is a point contact whereas the cathode for the coaxial detector is a hollowed out bore through the center of the detector. Figure from [98].

PPC's have less electronic noise than coaxial detectors, they have better energy resolution at lower energies. At 662 keV, the average energy resolution across all of the Demonstrator's detectors is about 1.2 keV FWHM, whereas that of a typical coaxial germanium detector is around 2 keV FWHM [99]. For comparison, a representative energy resolution for a NaI scintillating detector is around 25 keV at that energy [100]. This energy resolution advantage, in addition to ultra-low backgrounds, is what allows the Demonstrator to compete with much larger dark matter experiments with more exposure.

There are two types of detectors in the Demonstrator, which will be denoted as "natural" and "enriched" throughout the rest of this dissertation. The enriched detectors are fabricated from germanium that is enriched to 88% in ^{76}Ge, the isotope in which $0\nu\beta\beta$ is thought to occur. Enriched detectors are manufactured by ORTEC [101]. Natural detectors, produced by Canberra (now Mirion) [102], are made out of germanium with natural abundances of ^{76}Ge. These detectors are called BEGe detectors. The term HPGe is used to refer to both enriched and natural detectors throughout this dissertation.

HPGe's can be roughly divided into three separate regions, the active mass, the n+ contact (or dead layer), and the transition layer. See Figure 2.8. As discussed earlier in this chapter, biasing the detector to high-voltage causes the depletion region to fill up the entire bulk of the detector. This region contributes to the Demonstrator's total "active mass." The thick n+ layer on the exterior forms a "dead layer" with zero electric field. At the interface of the high E-field bulk and the dead layer is a region of low electric field called the diffusion dominated region, or the transition layer. When ionizing radiation deposits energy within the bulk of the detector, it liberates electrons and holes. The electrons drift towards the anode and the holes to the cathode as a result of the electric field from the high voltage. As these charges drift through the bulk of the detector, they induce current at the point contact according to the Shockley-Ramo theorem [103] [104]:

$$i = q\vec{v}_d \cdot \vec{E}_0 \tag{2.2}$$

where q is the drifting charge, $\vec{v}_d$ is the drift velocity, and the weighting field $\vec{E}_0$ is defined in terms of the weighting potential ϕ_0:

$$\vec{E}_0 = - \bigtriangledown \phi_0 \tag{2.3}$$

The weighting potential is obtained by solving the Laplace equation for the detector geometry, where the potential of the point contact is set to unity and the potential of the n+ anode is set to zero. A representative weighting potential for a PPC is shown in Figure 2.17. Because the gradient of the weighting potential is greatest near the point contact, most of the signal will be induced as the holes drift near the point contact. The induced signal will depend on the number of locations in which energy is deposited within the detector during an event. This point is illustrated by Figure 2.17 and 2.18. If ionizing radiation deposits energy a single location within the detector, indicated by the single red arrow and single red cloud in Figure 2.17, then a current pulse with a single peak is induced at the point contact similar to the bottom left of Figure 2.18. Integrating this current pulse gives the charge pulse on the top left of the figure. The height of the charge pulse is proportional to the energy of the event. This is called a single-site event. If the incident particle is a gamma which Compton scatters, illustrated by the combination of the red and black arrows/clouds in Figure 2.17, or if two incident particles deposit energy in the same detector simultaneously, then the result is a multi-site event. Because there are two charge clouds drifting through the detector, the current pulse will not be a single peak but will rather have a more complicated structure, as shown at the bottom of Figure 2.18.

Consider a single-site and multi-site event that are equal in energy. Though their charge pulses will be equal in height, the maximum height of the current pulse for the single-site event will be greater than that of the multi-site event. Thus, by taking the ratio of the current pulse height to the energy of the event, it is possible to distinguish between single-site events and multi-site events. The Majorana collaboration automatically calculates a parameter equal to this ratio called A/E. The A/E parameter is very useful, since multi-site events are a source of background near the 2039 keV region of interest for $0\nu\beta\beta$. The A/E method was originally developed by the GERDA collaboration [105]. Rather than taking the ratio of current pulse amplitude A and energy E, more recent MAJORANA analyses have taken to comparing these two parameters against each other independently (A vs E) [106]. It is much more difficult to discriminate single-site and multi-site events in coaxial germanium detectors because the gradient of their weighting potentials is not as localized as it is for PPC's, see Figure 2.19.

If radiation deposits energy in the diffusion dominated transition region, the result will be incomplete charge collection with an energy degraded event [107]. These energy degraded events show up in the region of interest for bosonic dark matter and must be dealt with. More details regarding this will be given in Chapter 3.3.

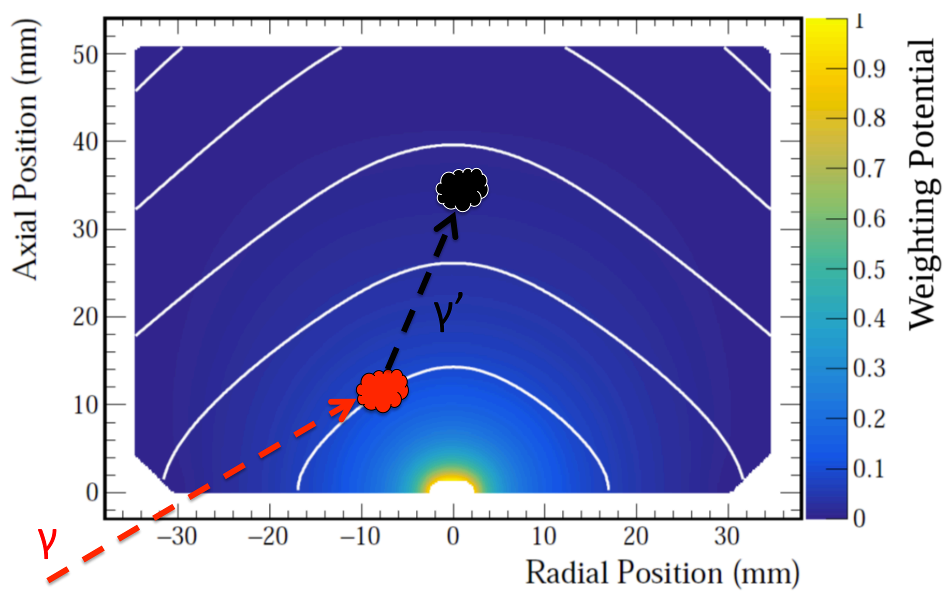

Figure 2.17: Representative weighting potential of a PPC detector. The red arrow and cloud illustrate a single-site event. The combination of the red and black arrows/clouds illustrate a multi-site event. Adapted from a figure by T. Caldwell.

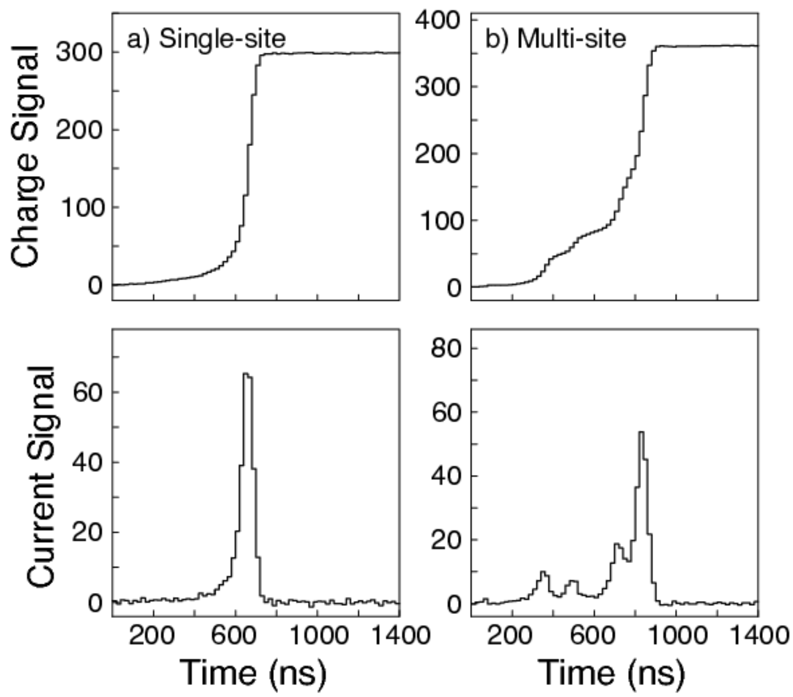

Figure 2.18: Current signal (bottom) and integrated charge signal of a single-site vs. a multi-site event. Figure from [70]

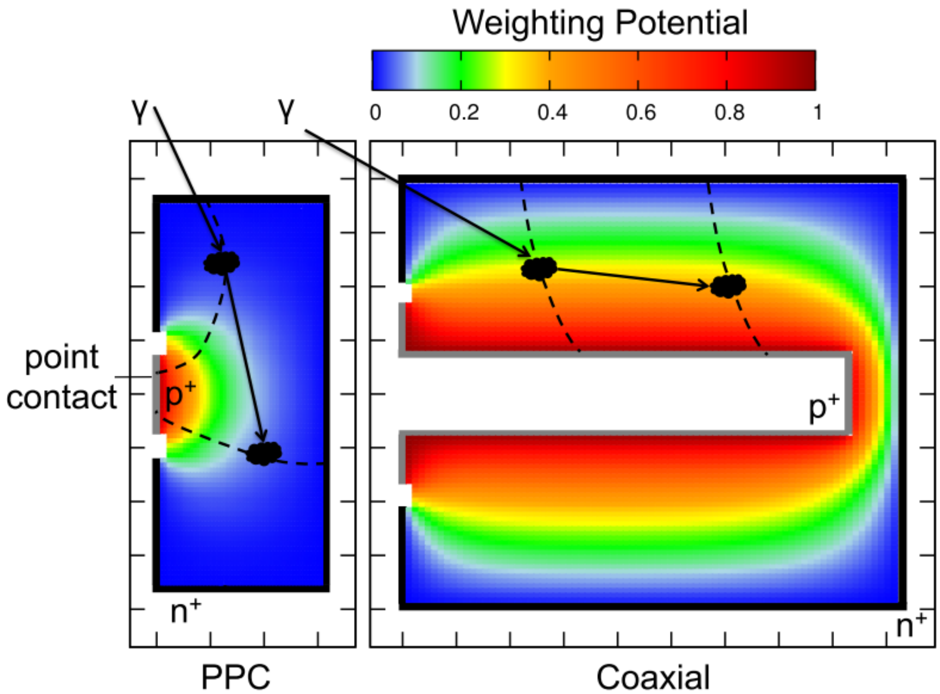

Figure 2.19: Weighting potential of a PPC and coaxial detector with charge drift trajectories for a multisite event. Figure adapted from GERDA PSA [108] [95].

Section 2.9: Energy Construction and Calibration

A trapezoidal filter was applied to the integrated charge signals [109]. The output $s(t)$ of a trapezoidal filtered waveform is given by the convolution integral:

$$s(t) = \int_{-\infty}^{\infty} v(t - t')\, h(t')\, dt' \tag{2.4}$$

where $v(t)$ is the input signal (the integrated charge waveform) and $h(t)$ is the response of the system (the trapezoidal filter). The waveforms can be described by an exponential decay function:

$$v(t) = \begin{cases} 0 & t < 0 \\ e^{-t/\tau} & t \geq 0 \end{cases} \tag{2.5}$$

where τ is the decay time constant, which is replaced by

$$\frac{1}{e^{1/\tau}-1} \tag{2.6}$$

for better precision. The trapezoidal filter is defined in terms of the rectangular function:

$$h_2(t) = \begin{cases} 0 & t < 0 \\ 1 & 0 \leq t \leq T_2 \\ 0 & T_2 \leq t \end{cases} \tag{2.7}$$

and the truncated ramp function

$$h_1(t) = \begin{cases} 0 & t < 0 \\ t & 0 \leq t \leq T_1 \\ 0 & T_1 \leq t \end{cases} \tag{2.8}$$

The impulse response of the trapezoidal filter is defined as:

$$h(t) = h_1(t) + \tau h_2(t) + (T_1 - \tau)\, h_2(t - T_1) - h_1(t - T_2) \tag{2.9}$$

The output $s(t)$ then becomes a symmetric trapezoidal function:

$$s(t) = \begin{cases} 0 & t < 0 \\ \tau t & 0 \leq t \leq T_1 \\ T_1\tau & T_1 \leq t \leq T_2 \\ T_1\tau - \tau(t - T_2) & T_2 \leq t \leq T_2 + T_1 \\ 0 & T_2 + T_1 \leq t \end{cases} \tag{2.10}$$

where the ramp time is T_1 and the flat time is equal to $T_2 - T_1$. This is all under the assumption that $t \ll \tau$. For the case of a triangle filter, which will be discussed in Chapter 3.3, the flat time is equal to zero and the output $s(t)$ reduces to:

$$s(t) = \begin{cases} 0 & t < 0 \\ \tau t & 0 \leq t \leq T_1 \\ T_1\tau - \tau(t - T_2) & T_2 \leq t \leq T_2 + T_1 \\ 0 & T_2 + T_1 \leq t \end{cases} \tag{2.11}$$

As previously mentioned, MAJORANA uses a resistive feedback preamplifier design. A consequence of this fact is that the tails of the charge waveforms have an exponential decay shape, which can be clearly seen in Figure 3.3. Applying a trapeziodal filter to such a pulse shape will result in a negative undershoot on the tail of the output. To get rid of this decaying tail, a pole-zero correction is applied to the waveform before the trapezoidal filter. For a more detailed discussion on trapeziodal filters and pole-zero corrections, see [110] [111] [112] [109]. The ramp time and flat time are the two values that affect the output shape. A shorter ramp time results in a steeper sloped trapezoid, and a longer flat time results in a wider trapezoid. These parameters are set to optimize the energy resolution; for our case, a ramp time of 4 μs and a flat time of 2.5 μs are used. From the trapezoidal output, a variety of energy parameters can be calculated. The energy parameter used in this analysis is called "trapENF," where "ENF" stands for "Energy with Nonlinearity correction at Pick-off time." The raw energy is obtained from the trapezoidal output by taking the height of the trapezoid at a fixed pick-off time, which is roughly 0.5 μs from the falling edge of the trapezoidal filter.

The raw energy is calibrated with a ^{228}Th line source deployed into the calibration track shown if Figure 2.9. A tool called the MultiPeakFitter, developed by I. Guinn, was used to fit the 238, 240, 277, 300, 583, 727, 785, 860, and 2614 keV peaks in the calibration spectrum. The the mean values of these peaks in the raw energy parameter were compared to the peaks' true energies.

Nonlinearities can arise in the ADC chips on the GRETINA cards. These nonlinearities can lead to deviations in the energy estimation of up to 1 keV as well as affect aspects of the pulse shape analysis, leading to degraded energy resolution. Measurements of the ADC nonlinearities are accomplished through application of a ramped voltage signal directly to the front-end inputs of a digitizer. With a linearly ramped input from a well-behaved function generator, one can observe any deviations from linearity in the digitized output of an ADC. A nonlinearity correction is then applied to produce the final "trapENF" energy parameter. For a more detailed discussion on energy construction and calibration, see [109].

CHAPTER 3: Backgrounds and Data Cuts

A description of the various types of backgrounds in the 5-100 keV region of interest for bosonic dark matter is provided in this chapter. The 100 keV upper bound comes from the fact that, above this energy, dark vectors are excluded by the galactic gamma background and by the cosmological requirements for dark matter abundance, as illustrated in Figure 1.11. The 5 keV lower bound comes from the degradation of the background discrimination cuts and acceptance efficiency below this energy, as will be explained in Chapters 3.3 and 4.1.2 respectively. I describe the various techniques used to mitigate these backgrounds. An energy spectrum of events is presented with all background discrimination cuts applied.

Section 3.1: Flat Continuum and Lead X-Rays

Background events in the 19-100 keV energy window come from ^{210}Pb and the flat continuum. ^{210}Pb emits a 46.5 keV X-ray, and while its origin is unknown, it is suspected to come from plate-out of radon daughters on components near the detectors. The flat continuum originates from energy degraded events or from instances in which an external gamma Compton scatters within the active mass of a germanium detector, and the scattered gamma subsequently escapes. Figure 4.1 illustrates the special case of such a Compton event where the scattered gamma is absorbed by a second germanium detector. The 46.5 keV ^{210}Pb line and flat Compton background are shown in the bottom of Figure 3.15.

Section 3.2: Cosmogenics

Below 19 keV, the dominant source of background is cosmogenic activation. Chapters 2.6 and 2.5 describe the precautions that were taken to minimize the production of cosmogenic isotopes in the enriched germanium detectors and copper support structures. The handling history of each detector and of all components of the DEMONSTRATOR was recorded in the Parts Tracking Database [113]. From the handling information, it is possible to estimate the level of cosmogenic contaminants in a detector. Figure 3.1 shows the estimated amount of ^{68}Ge in one DEMONSTRATOR detector as a function of time. Figure 3.2 shows the dramatic improvement in cosmogenic backgrounds in the enriched detectors compared to the natural detectors, for which cosmic ray exposure was less controlled.

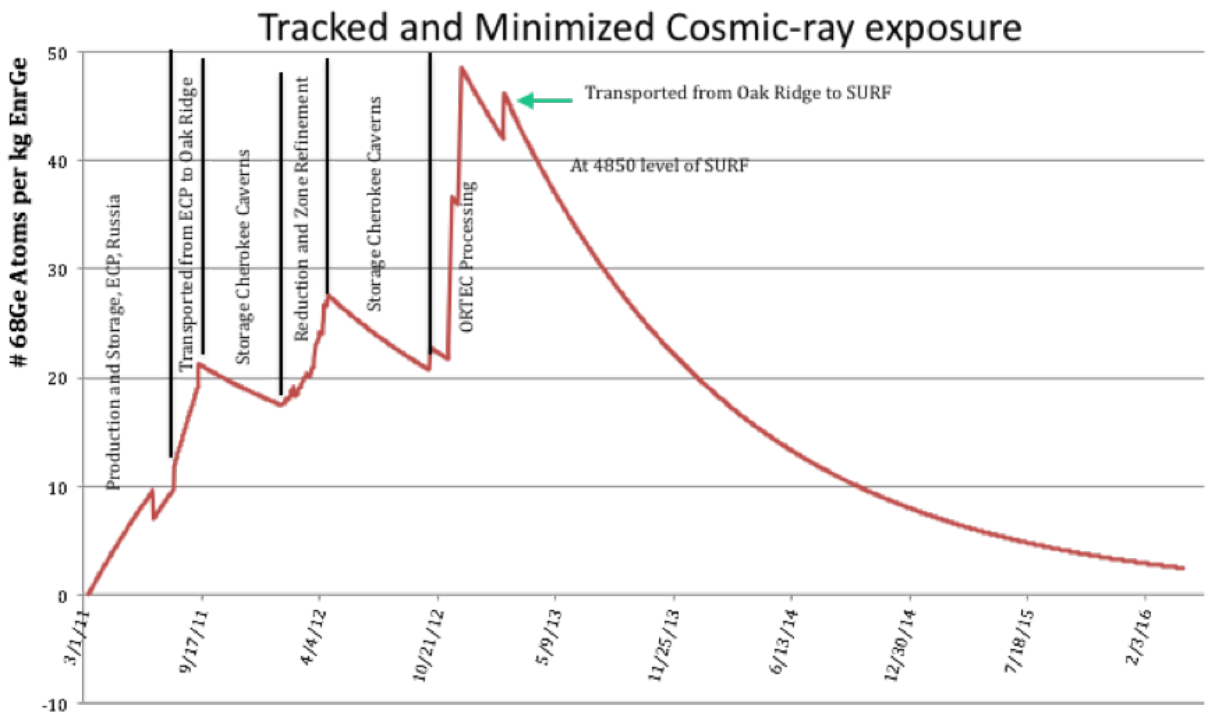

Figure 3.1: Estimated number of ^{68}Ge atoms in a sample DEMONSTRATOR detector. ^{68}Ge increases every time the detector is transported above surface and exponentially decays away when the detector is stored underground. This plot tracks the history of the germanium in the detector from production in Russia to its final location at SURF. Figure generated by B. White.

Section 3.3: Slow Pulses

As explained in the Chapter 2, HPGe PPC's are composed of three main regions: the bulk, the dead layer, and the diffusion dominated transition region. If an event deposits

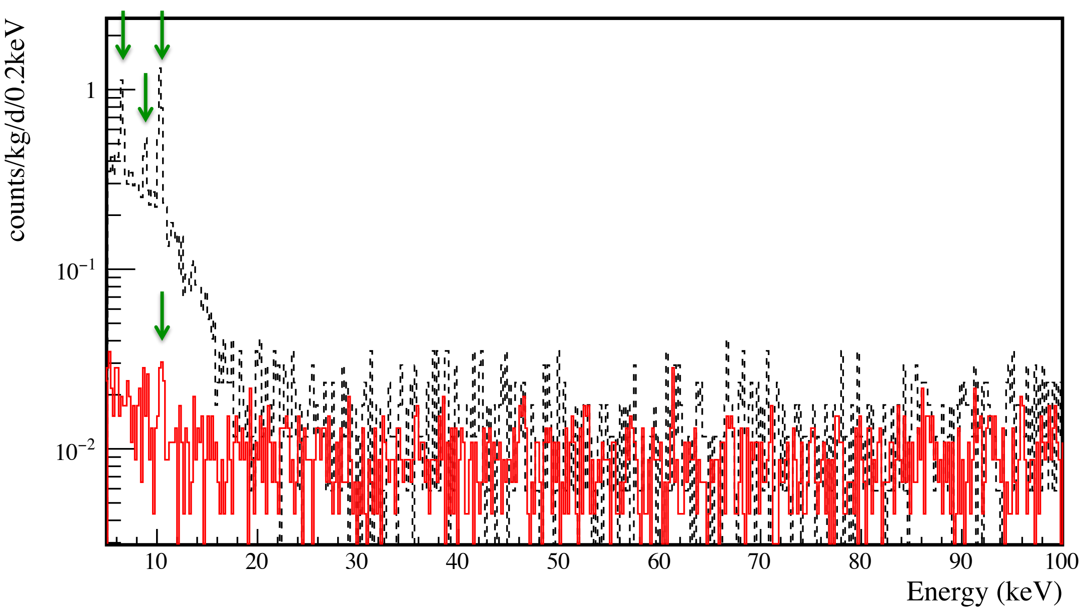

Figure 3.2: The DEMONSTRATOR's commissioning data, DS0, comparing the background spectrum from natural detectors (black dotted line) with enriched detectors (solid red line). Prominent features are the tritium spectrum and the 6.5 keV, 8.9 keV, and 10.36 keV peaks from ^{55}Fe, ^{65}Zn, and ^{68}Ge respectively. One can barely make out the tritium spectrum and ^{68}Ge line in the enriched detectors. The spectrum from natural detectors is scaled by 171 kg $\cdot$ d of exposure, and the enriched spectrum by 460 kg $\cdot$ d.

energy in the bulk, then the result is a pulse with a sharply rising leading edge. But if ionizing radiation deposits energy in the transition region, the liberated charges will slowly diffuse into the depletion region, resulting in incomplete charge collection and an energy degraded pulse with a slow rising edge, depicted in Figure 3.3. These events have been designated "slow pulses." Slow pulses are a significant source of background in the low energy spectrum, below 100 keV.

To remove slow pulses, a technique was developed [67] that makes use of a triangle digital signal filter, which was introduced in Chapter 2.9. For additional reading on triangle filters, see [67]. The triangle filter is chosen to have a ramp time of 100 ns, based on the tuning of the A/E parameter by MAJORANA's data cleaning group [114]. The effects of the triangle filter, which are somewhat analogous to that of a smooth derivative, are shown both on a slow pulse and on a good physics waveform in Figure 3.4.

The maximum value of the triangle filter will depend on the height of the waveform, which is determined by the energy of the event, and on the slope of the pulse's rising edge. To remove the pulse height dependence, the triangle filtered waveform is normalized by the waveform energy "E," which is proportional to the charge pulse height. The maximum value of the energy scaled, triangle filtered waveform, or "T/E," will give a measure of the maximum slope of the original waveform's rising edge. The T/E parameter provides excellent separation between between physics events and slow pulses, allowing one to remove nearly all slow pulses with a high acceptance efficiency for physics events throughout most of the ROI for bosonic dark matter. However, it's performance degrades at lower energy.

To apply the T/E cut, a box cut is set around the range of T/E values corresponding to bulk events, and everything outside of that box is excluded. The box cut derives its name from that fact the T/E values it selects do not vary with respect to energy, and so the cut is box shaped in T/E vs energy parameter space. The box cut used in the DEMONSTRATOR's first bosonic dark matter result [77], published with the commissioning data set, is shown in

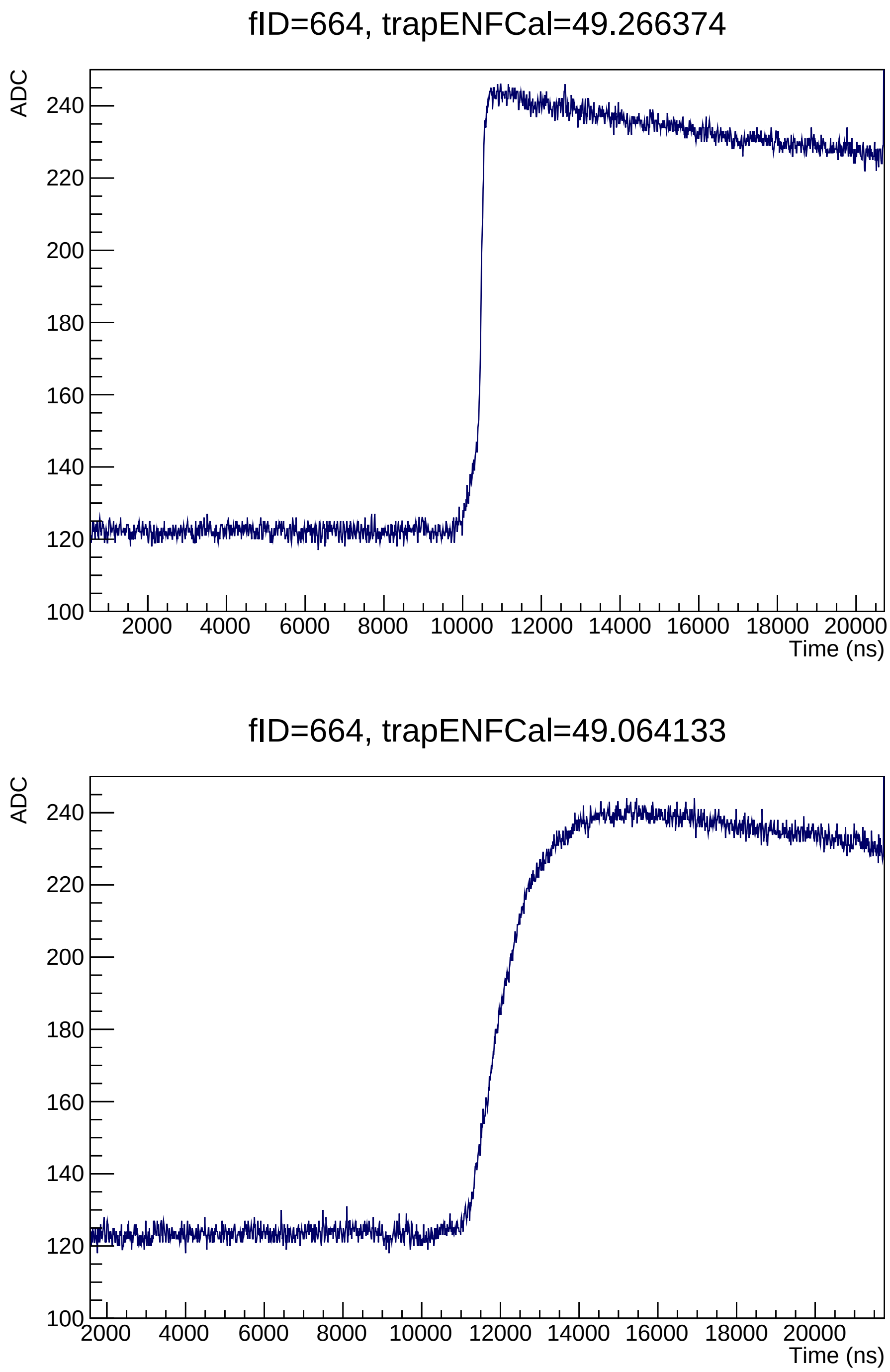

Figure 3.3: Top: A 49 keV waveform from a physics event (or "bulk event") in DS1, detector C1P3D4. Bottom: A 49 keV slow pulse (or "transition region event") in DS1, detector C1P3D4.

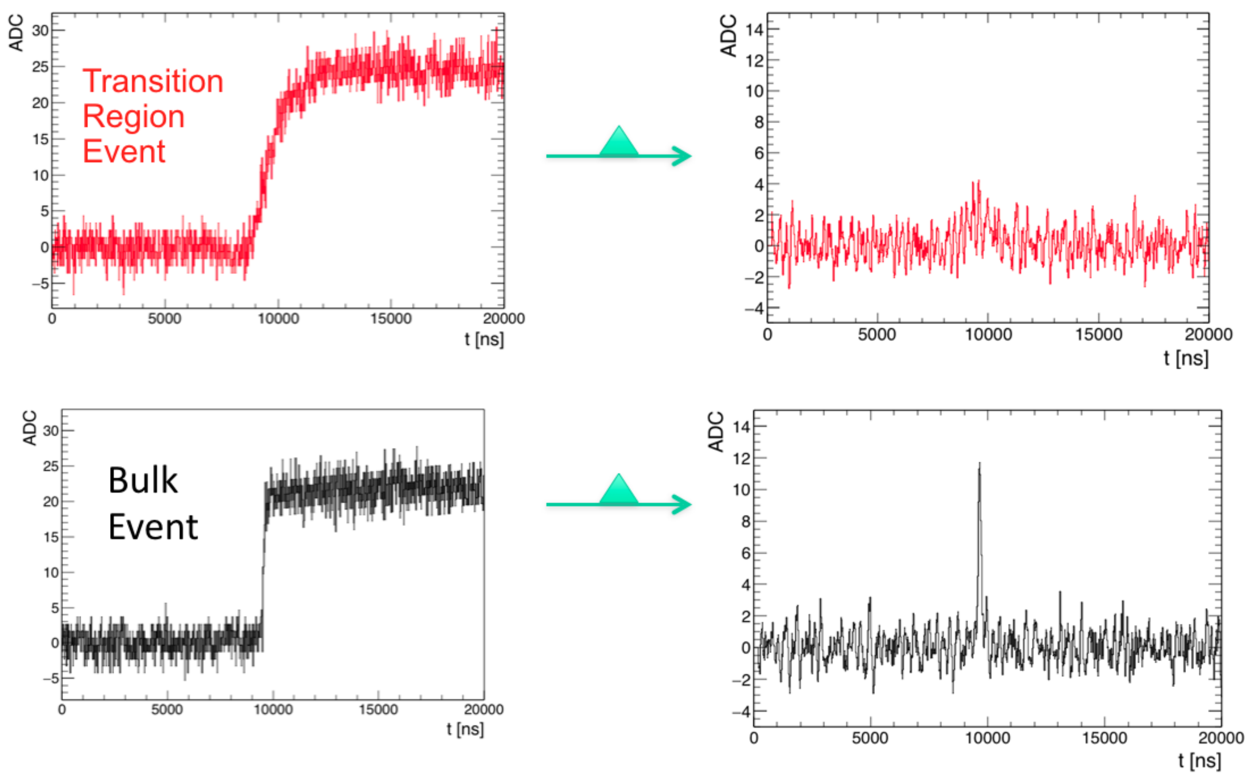

Figure 3.4: A triangle filter applied to a slow pulse (top) and a bulk event (bottom). Because the slope of a slow pulse's rising edge is smaller than that of a good physics event, the maximum value of it's triangle filter (top right) is smaller than that of the good physics pulse of similar energy (bottom right).

Figure 3.5. Prominent features in this plot are the three horizontal bands stemming from physics events, and the banana shaped band of events at low T/E values which comes from slow pulses. The T/E values of the signal bands are constant with respect to energy above 20 keV because, at these energies, the rising edge of signal events in any given detector all have the same slope. From 20 keV down to 5 keV, the signal band expands slightly as the signal to noise ratio deteriorates. Below 5 keV, the T/E parameter blows up and physics events merge with slow pulses. This is because T becomes constant as energy approaches 0 keV, so T/E scales as 1/E. 5 keV was used as the analysis threshold in [77], and the same threshold will be used in this analysis. The blob of events directly above the box cut at 20 keV and 45 keV are due to electronic noise.

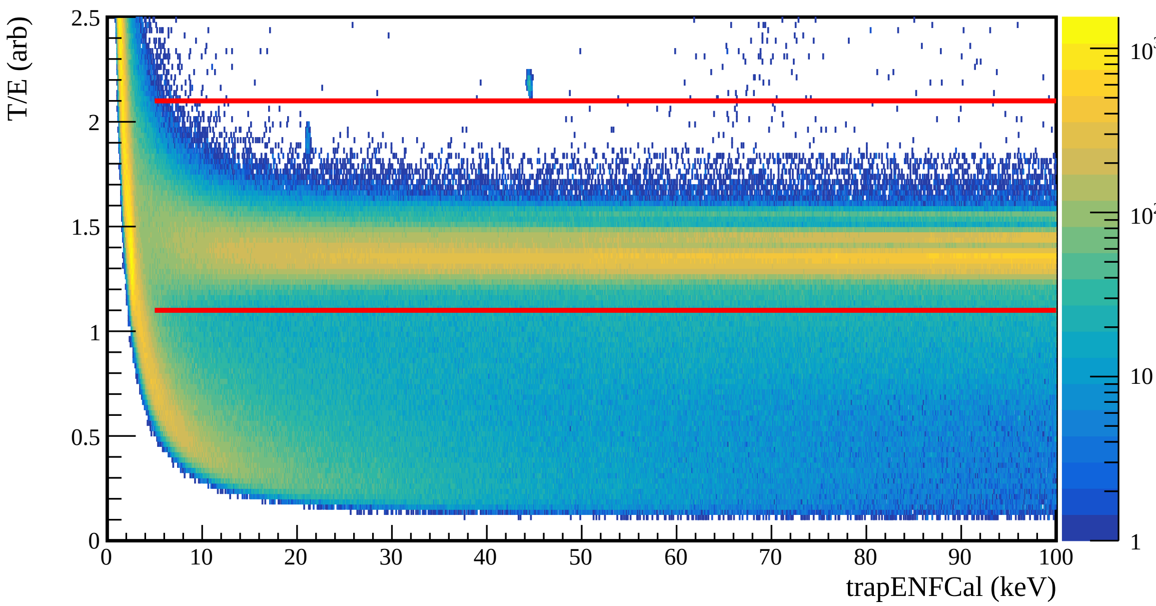

Figure 3.5: T/E vs Energy distribution for DS0 calibration data (whole array) showing the cut used in [77]. Calibration data was used to tune the cut. Events inside horizontal red lines are accepted and those outside are rejected.

Section 3.4: Improved T/E Cut

Since the release of the commissioning data result [77], extensive effort has gone into improving the T/E cut. As previously mentioned, the signal band in the T/E distribution widens slightly at lower energies as the signal to noise ratio deteriorates, but is narrower at higher energies. From Figure 3.5, one can see that the old T/E box cut did not vary with respect to energy over the entire 5 - 100 keV region of interest. In order for the cut to have a reasonable acceptance efficiency at 5 keV, it had to be made overly conservative at higher energies. A new and improved cut, which will be referred to as a composite cut, has been tailored to match the shape of the signal distribution. An example of this composite cut is depicted in Figure 3.6. This cut consists of three adjacent box cuts that get narrower in T/E at higher energy. The lowest energy cut is applied from 5 keV, the analysis threshold, to 9 keV, the analysis threshold used in an earlier version of this analysis. The second cut extends from 9 keV to 20 keV, the point where the trumpet shape of the signal band flattens out. The third cut goes from 20 keV up to 100 keV, the upper limit of this analysis.

A second improvement to the T/E cut pertains to how the detectors are grouped together within the cut definition. From Figure 3.5, one can see three separate signal bands at higher energies. This is because the mean T/E value of the signal band for each detector is unique, and some detector's signal bands overlap more closely than others. The band highest in T/E is from detector channel 608, the middle band comes from 576, 592, 594, 600, and 674, and the lowest band is the composite of the remaining channels. In defining a single cut to apply to all three bands of detectors simultaneously, it is necessary to make the lower bound of the cut overly conservative for the top band of detectors in order to achieve good acceptance efficiency for the lower band. The same applies to the lower band of detectors and the the upper bound of the cut. It would be far better to define a unique composite cut for each band, and this is precisely the strategy applied in this analysis. The procedure for tuning the composite cut begins with making a T/E distribution with calibration data similar to Figure 3.6 for each band of detectors. Then for each of the three box cuts within

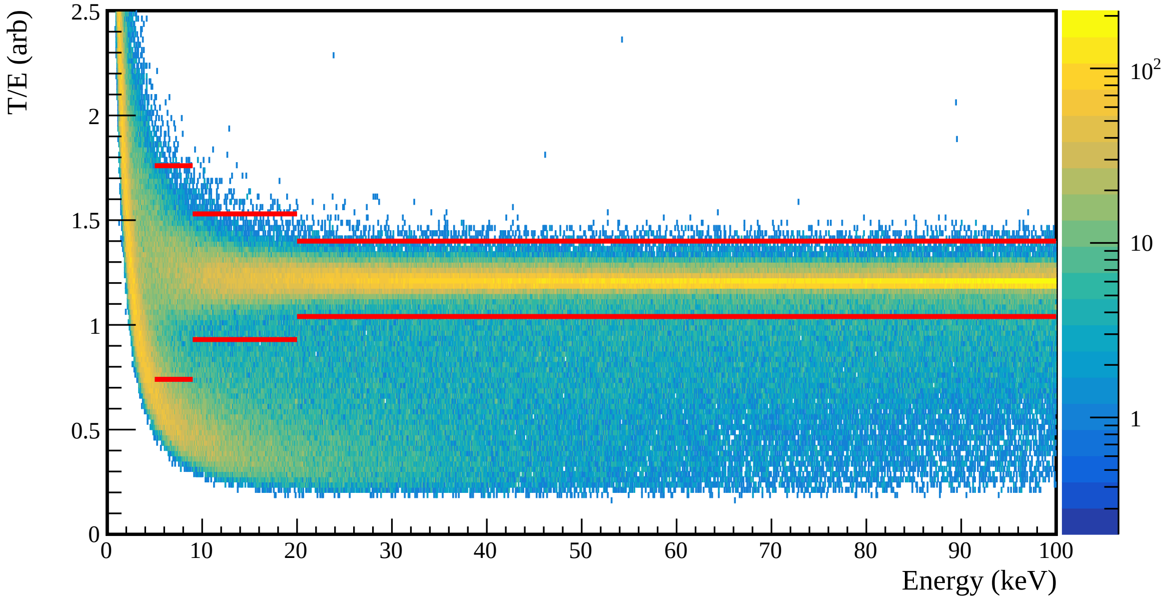

Figure 3.6: Improved version of the T/E cut shown for DS1 detector C1P3D4 on calibration data. Three separate cuts covering energies 5-9 keV, 9-20 keV, and 20-100 keV respectively are defined, which get narrower at higher energy.

the composite cut, a small cross section of the T/E distribution of some width in energy is projected onto the T/E axis to create a one dimensional histogram of T/E, as shown in Figure 3.7. The signal peak in the one dimensional T/E histogram is fit to a Gaussian, and $\pm 3\sigma$ from the fit are taken as the upper and lower limits of the box cut. The width in energy of the projected cross sections were set empirically to maximize the signal to noise ratio. Because the grouping of detectors into bands varies between data sets, this procedure had to repeated for each data set. Appendix B contains a list of the upper and lower limits used in each composite cut, for each band, for each data set.

Section 3.5: Pulser Retriggers

Electronic pulsers are injected directly into the preamplifiers on all detector channels to ensure their readout remains live during data taking and for use in estimating detector livetime. On a few channels, ringing of the pulsers due to impedance mismatch can result in

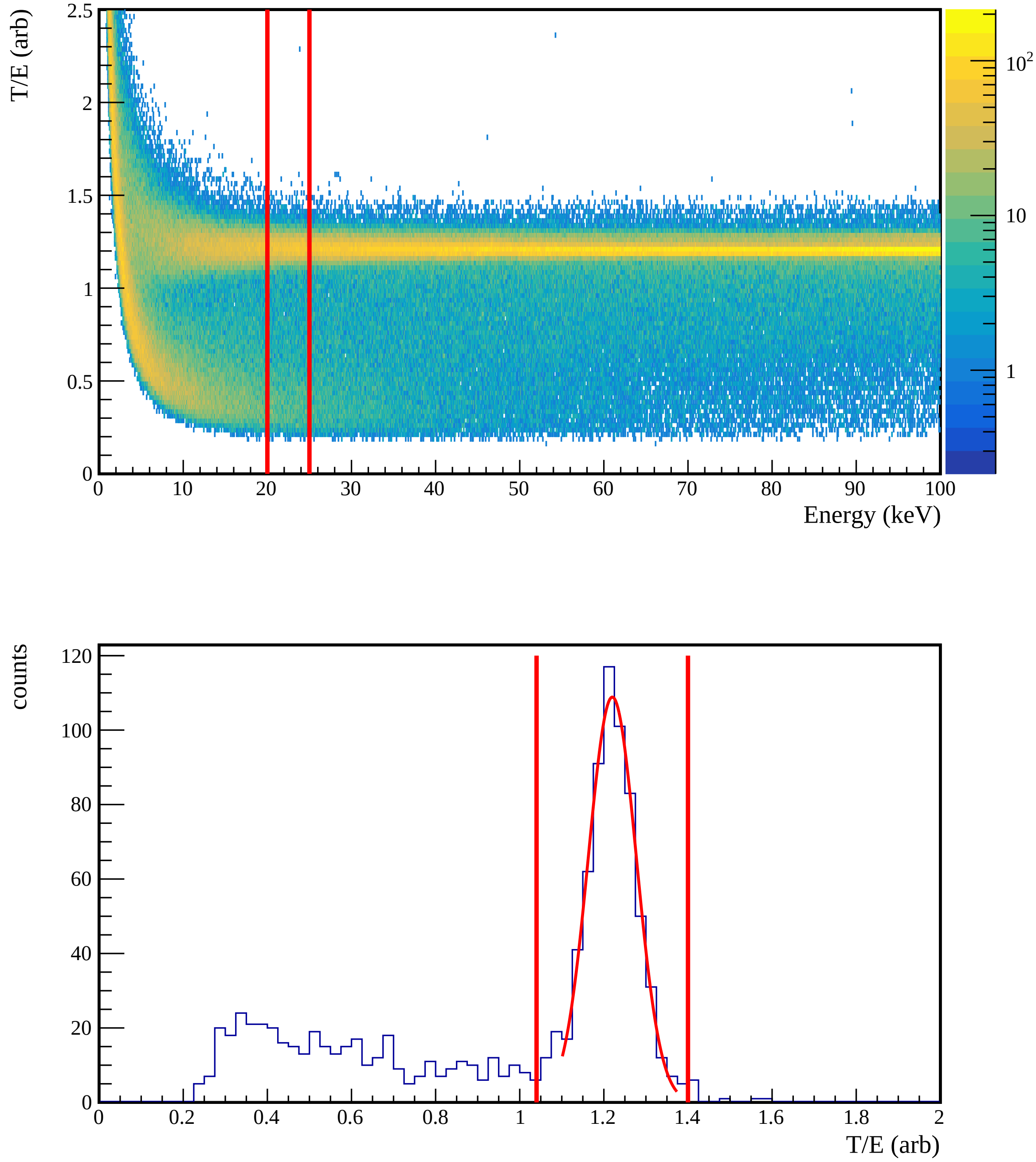

Figure 3.7: Top: C1P3D4 T/E distribution showing the cross section between the red lines that is projected on the y-axis to get the plot on bottom. Bottom: Projected T/E distribution of C1P3D4 from DS1 with calibration data. The signal peak is fit with a Gaussian, and $\pm 3\sigma$ are delineated by the vertical red lines.

a pulse that undershoots the baseline. If the trigger threshold on these channels is set too low, the digitizer can retrigger on the recovering waveform as it decays back to baseline and overshoots, resulting in a slowly rising pulse depicted in Figure 3.8. For further details on pulser retriggers, see [67]. By contrast, the tail of an ordinary physics pulse decreases monotonically as charge decays through the feedback resistor in the first stage of the preamplifier, see Figure 3.3 . Because of this falling tail, applying a trapezoidal filter without a pole-zero correction to a good physics pulse will result in a negative undershoot on the filtered waveform's tail. The monotonically increasing pulser retriggers suffer no such undershoot, and this fact was used to create a parameter called "trapETailMin" to cut pulser retriggers [67]. This parameter calculates the minimum value of the tail of a trapezoidal filtered waveform without a pole zero correction. The negative undershoot on good physics waveforms results in a negative value of trapETailMin whereas the monotonically increasing pulser retriggers have a positive trapETailMin value. Figure 3.9 shows how different events populate the space of trapETailMin vs energy.

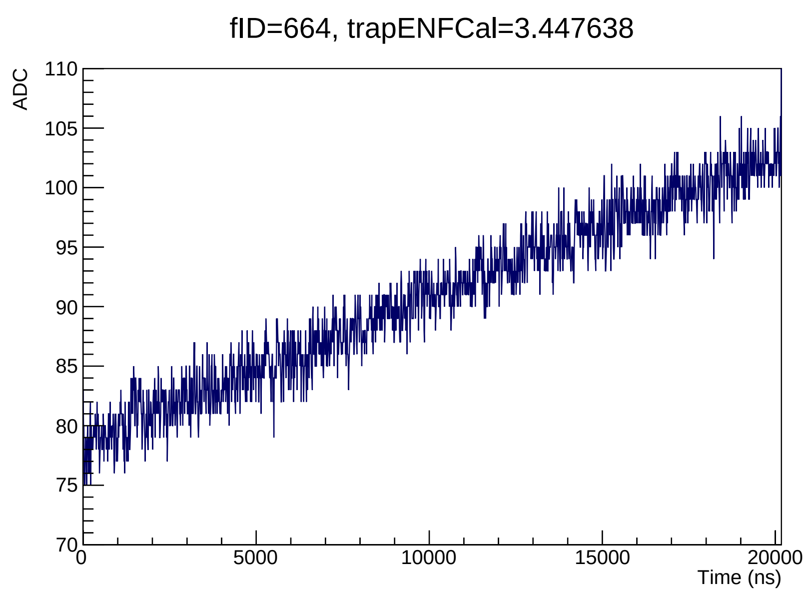

Figure 3.8: Example of a pulser retrigger waveform from DS1, detector C1P3D4 with its characteristic monotonically increasing tail. The parameter trapENFCal is the same as the trapENF parameter described in Chapter 2.9. "fiID" refers to the detector channel.

The pulser retrigger cut is tuned for each detector and for each data set. This is done

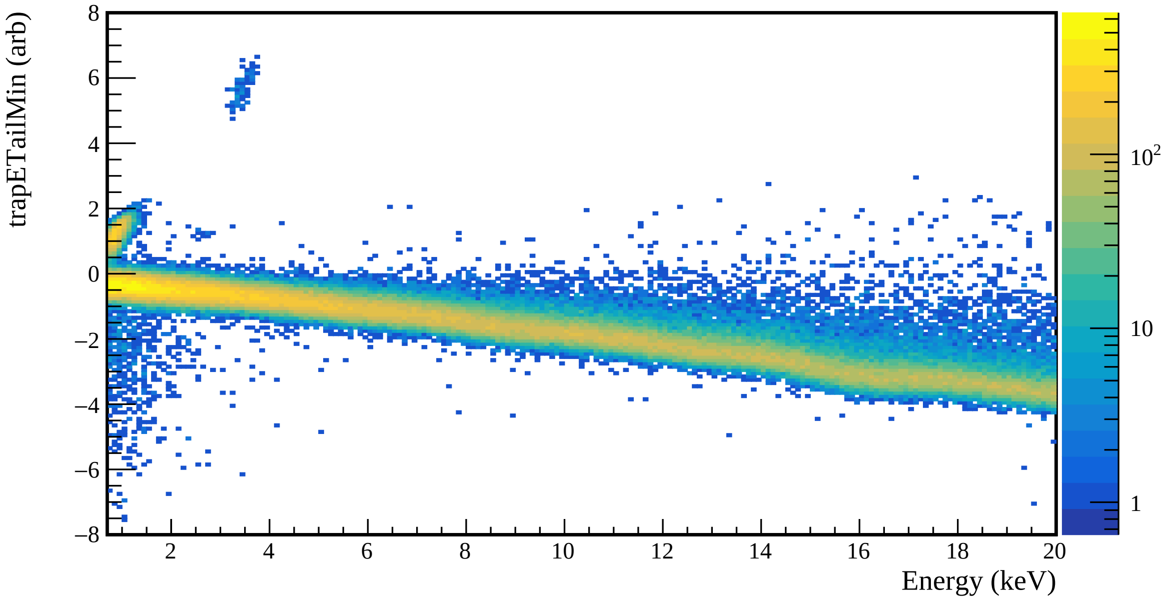

Figure 3.9: trapETailMin vs energy distribution for C1P3D4 in DS1 using calibration data. The diagonal, downward sloping band with negative values of trapETailMin are good physics events, and the two blobs of events at low energy with positive trapETailMin are pulser retriggers.

by projecting Figure 3.9 onto the vertical (trapETailMin) axis, as in Figure 3.10 top. The cut is made by setting a cutoff at the local minimum between the signal and pulser retrigger peaks and rejecting all events with trapETailMin greater than this cutoff. Because physics waveforms have a falling tail and pulser retriggers have a rising tail, one would naively expect there to be a sharp cutoff between the two populations of events at trapETailMin = 0. One can see from the upper-left-hand corner of Figure 3.9 that the signal and noise populations blend together near trapETailMin = 0, so the cutoff will not always equal zero and will vary in value for each detector. Figure 3.10 middle and bottom shows examples of physics pulses with trapETailMin > 0. Appendix C tabulates these cutoff values for all detectors and data sets.

Section 3.6: Transient Noise

Transient noise is believed to be electronic in nature and is called transient because of it's peculiar phenomenology of abruptly showing up in a data set and then disappearing a few runs later. Transient noise is not as well characterized as slow pulses or pulser retriggers and could come from a variety of sources such as HV breakdowns in cabling, microdischarges from detectors, ground loops, and microphonics (high frequency mechanical vibrations). The strategy for getting rid of transient noise is to select runs and detectors that do not have events associated with transient noise, which I call low energy run and detector selection. This is separate from and in addition to the run and detector selection performed by the Data Quality working group [115] [116] [117] [118] [119] [120] [121], because it focuses exclusively on noise in the low energy spectrum, most of which occurs below 10 keV. Usually, the transient noise in a data set can be isolated to a few detectors within a few runs. By removing these, it is possible to completely cut the transient noise without sacrificing much exposure. It is necessary to have a consistent, non-subjective and automated procedure for doing this selection to avoid bias. This procedure begins by making a histogram of counts broken down by detector channel and run number for each data set. An example of such a

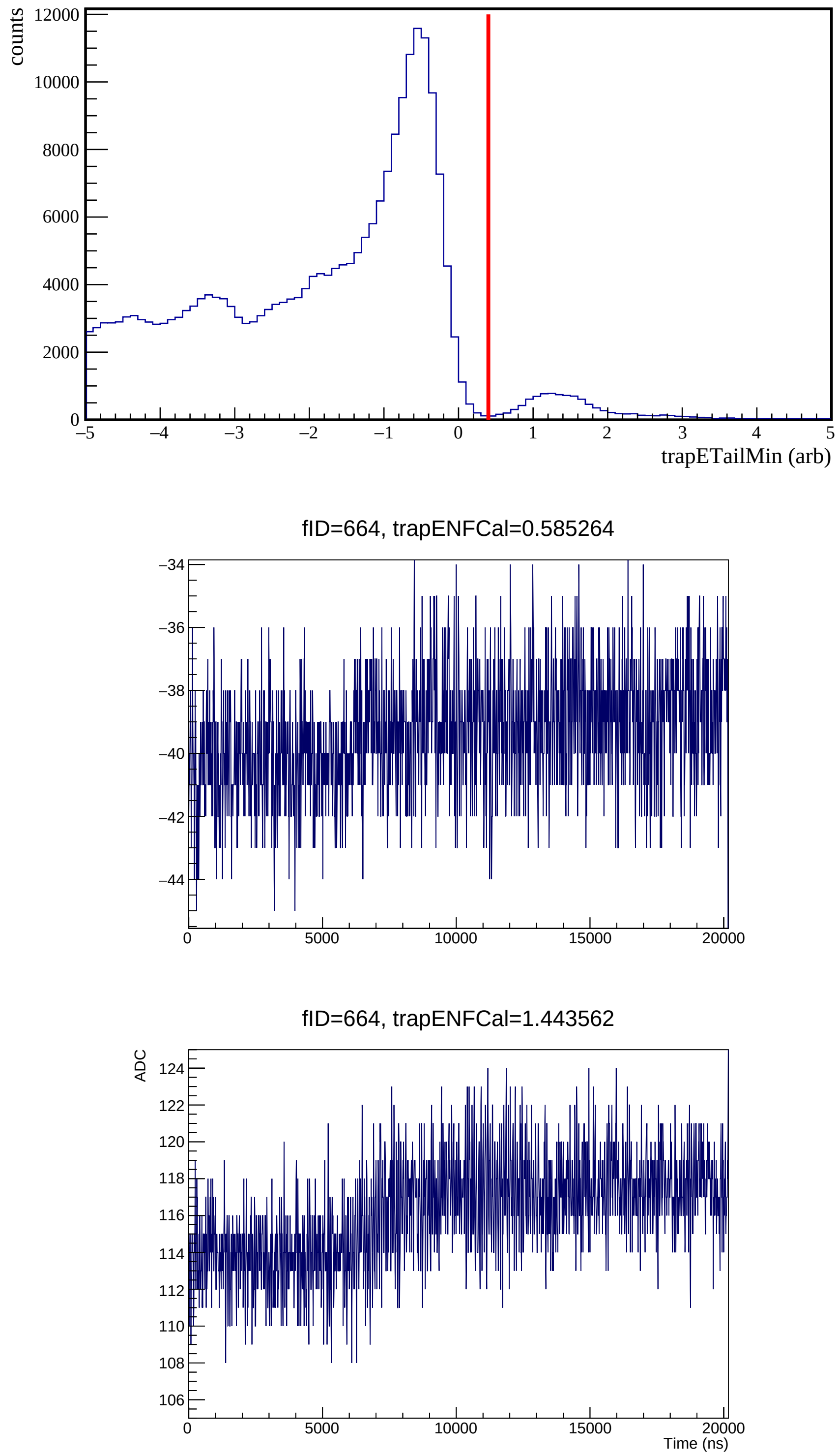

Figure 3.10: Top: Projection of trapETailMin vs energy distribution onto the trapETailMin axis for C1P3D4 in DS1 using calibration data. Events to the right of the vertical red line are rejected in the cut, and events to the left are accepted. Middle: A signal event from C1P3D4 in DS1 with 0 < trapETailMin < cutoff. Bottom: A signal event from C1P3D4 in DS0 with 0 < trapETailMin < cutoff.

histogram is given in the top of Figure 3.11 for DS5b. A script was written that calculates the mean number of counts per bin across all non-empty bins, then searches for bins whose count exceeds the mean by a factor of ten or more and prints out the corresponding run and detector channel numbers, see Figure 3.11 bottom. Finally, the flagged detectors and runs are cross-referenced against the corresponding Run Elog entries and Run Database plots to search for any clue that might explain the excessive rate. This procedure is applied only after all data cleansing cuts (like the pulser retrigger cut and the T/E cut) have been applied. Elogs [122] are the electronic note taking and bookkeeping system that Majorana uses, and the Run Database contains metadata about every single data run that is recorded. An example of how this process works is depicted in figures 3.12 and 3.13. Detector channel 692, or C1P2D1, has been flagged by the algorithm for runs 22937, 22946, 22952 and 22954. Consulting Run Elog 1717 (Figure 3.12), one can see that the threshold on C1P2D1 was raised during run 22909 due to microdischarges, and the Run Database plots in Figure 3.13 show evidence of microdischarge in this detector during run 22954.

Section 3.7: Choosing Which Data Sets To Include

Chapter 2.4 listed 8 data sets consisting of data from both natural and enriched detectors. The question arises as to which data should be included in the bosonic dark matter analysis and which should be excluded. While increasing the exposure tends to improve the final confidence limit, including data with high backgrounds has the opposite effect. The goal is to produce updated limits on the axioelectric coupling constant g_{Ae} and the effective vecor-electric coupling constant α'/α that improve upon the DS0 limit with the commissioning data [77] [67]. Equations 3.1 and 3.2 describe how g_{Ae} and α'/α vary functionally with respect to background rate and exposure:

$$g_{Ae} \propto \sqrt[4]{\frac{b}{MT}} \tag{3.1}$$

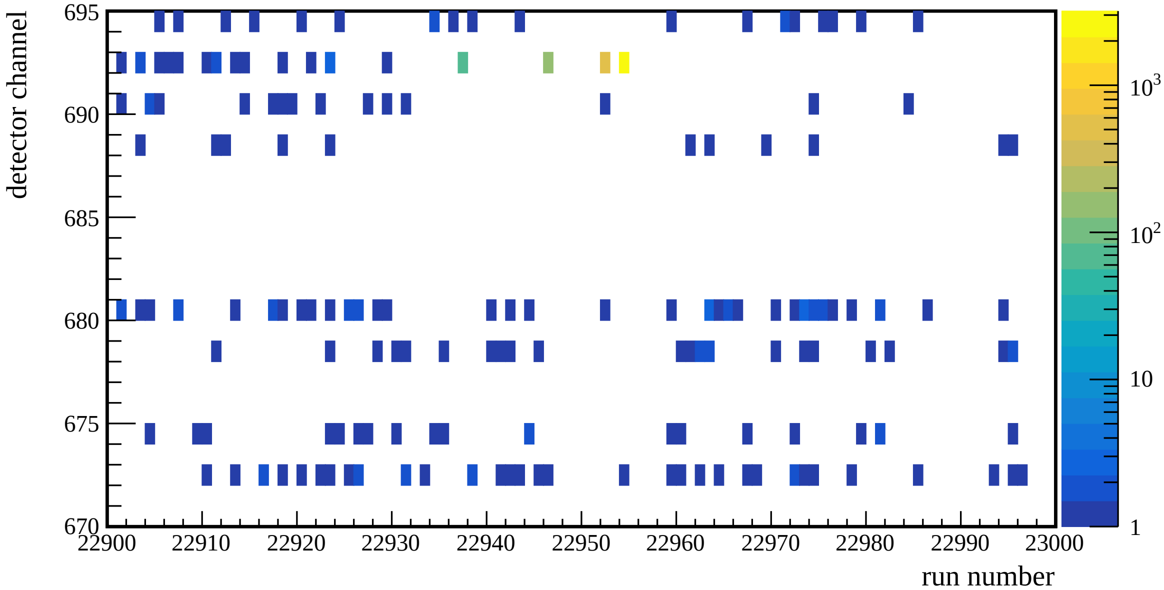

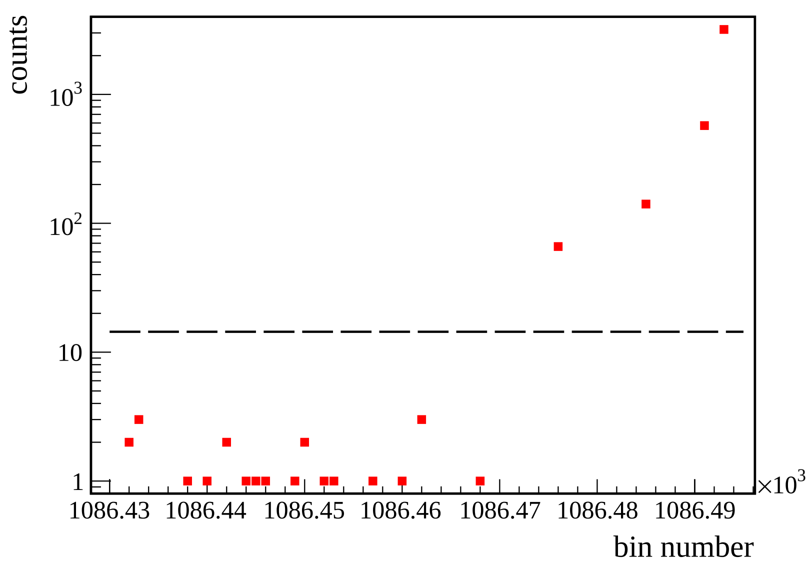

Figure 3.11: Top: Count rates vs. detector channel and run number. The vertical axis is detector channel number, and the horizontal axis is run number. The transient noise in DS5b runs 22937, 22946, 22952 and 22954 is isolated to detector channel 692, or C1P2D1, a natural detector. See the four bins in the top, middle of the plot that are not colored blue. Bottom: Shows the four bins from the top plot whose count rates exceed the mean by a factor of 10.

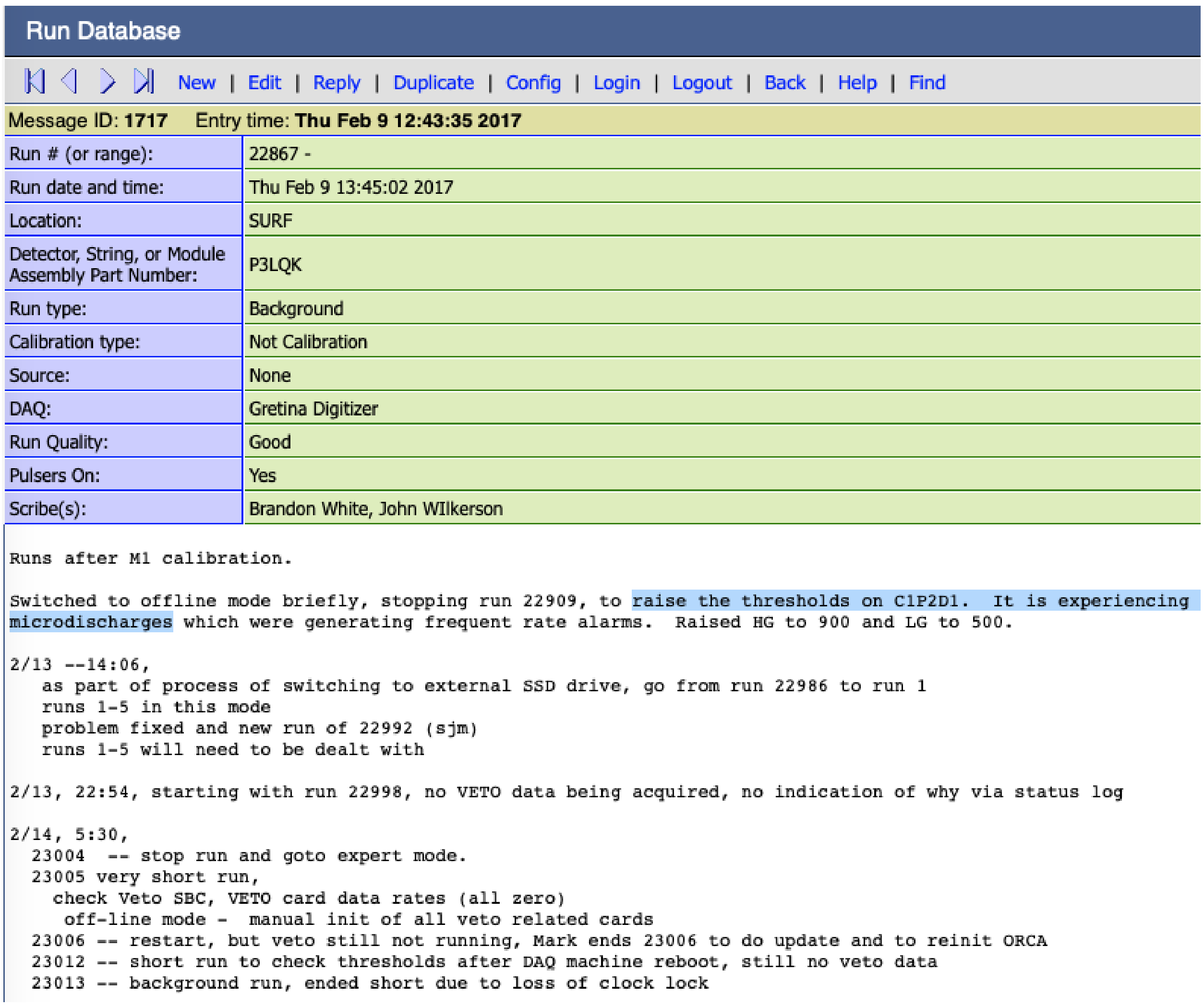

Run Database

New | Edit | Reply | Duplicate | Config | Login | Logout | Back | Help | Find

Message ID: **1717** Entry time: **Thu Feb 9 12:43:35 2017**

Run # (or range):	22867 -
Run date and time:	Thu Feb 9 13:45:02 2017
Location:	SURF
Detector, String, or Module Assembly Part Number:	P3LQK
Run type:	Background
Calibration type:	Not Calibration
Source:	None
DAQ:	Gretina Digitizer
Run Quality:	Good
Pulsers On:	Yes
Scribe(s):	Brandon White, John WIlkerson

```
Runs after M1 calibration.

Switched to offline mode briefly, stopping run 22909, to raise the thresholds on C1P2D1.  It is experiencing
microdischarges which were generating frequent rate alarms.  Raised HG to 900 and LG to 500.

2/13 --14:06,
   as part of process of switching to external SSD drive, go from run 22986 to run 1
   runs 1-5 in this mode
   problem fixed and new run of 22992 (sjm)
   runs 1-5 will need to be dealt with

2/13, 22:54, starting with run 22998, no VETO data being acquired, no indication of why via status log

2/14, 5:30,
  23004  -- stop run and goto expert mode.
  23005 very short run,
    check Veto SBC, VETO card data rates (all zero)
     off-line mode -  manual init of all veto related cards
  23006 -- restart, but veto still not running, Mark ends 23006 to do update and to reinit ORCA
  23012 -- short run to check thresholds after DAQ machine reboot, still no veto data
  23013 -- background run, ended short due to loss of clock lock
```

Figure 3.12: Run Elog 1717 with record of raised trigger threshold on C1P2D1 due to microdischarge.

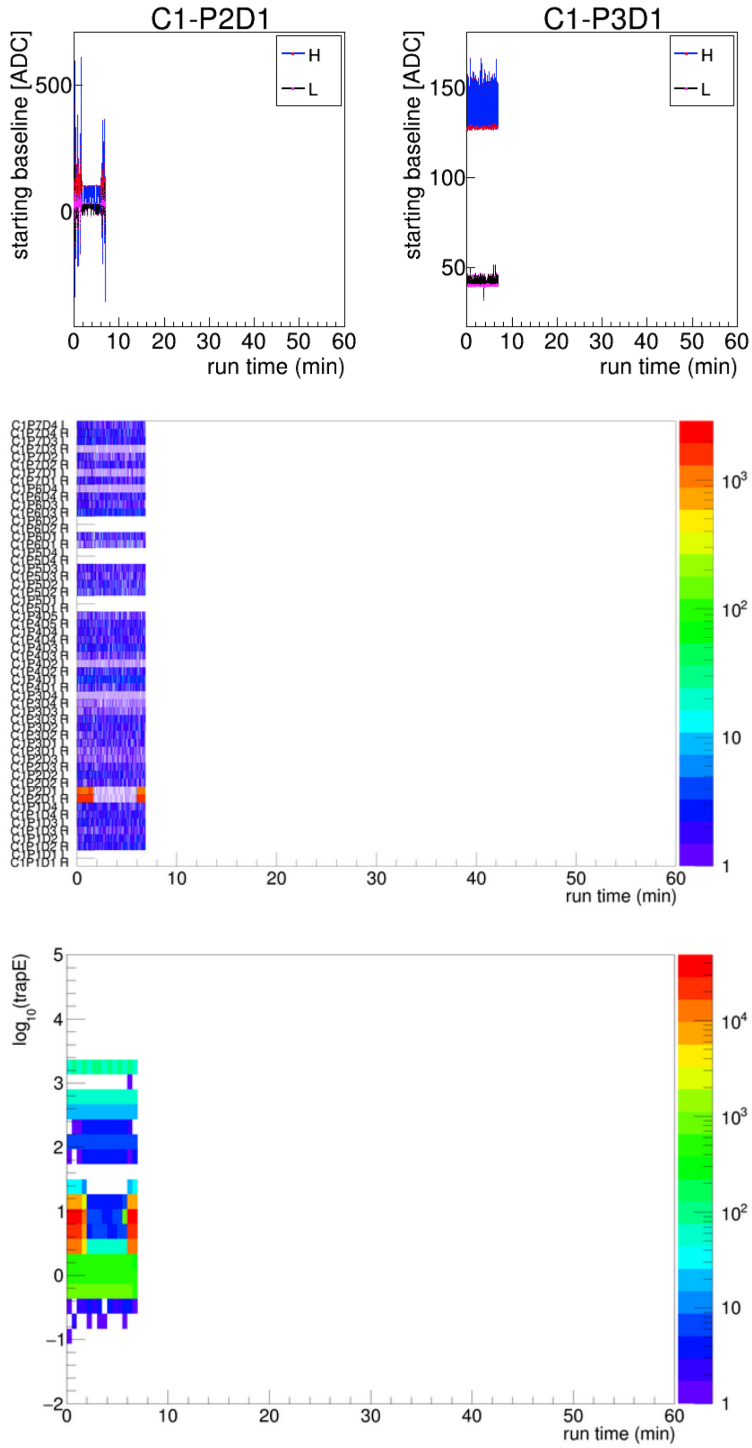

Figure 3.13: Top: A plot from the Run Database comparing the baseline of noisy detector C1P2D1 with normal detector C1P3D1 during run 22954. The spikes in C1P2D1 baseline are characteristic of microdischarge. Middle: Run Database plot of individual detector rates during run 22954 shows bursts of excessively high rate for C1P2D1 on both the high and low gain channels. Bottom: Run Database plot of Module 1 energy spectrum versus time during run 22954 shows intermittent bursts of very high rate.

$$\frac{\alpha'}{\alpha} \propto \sqrt{\frac{b}{MT}} \tag{3.2}$$

where b is the background rate in counts per kg $\cdot$ d and MT is the exposure of the data set in kg $\cdot$ d. Because background rate is equally important as exposure for both pseudoscalars and vectors, the decision was made to exclude the natural detectors from all data sets, as well as DS0 and DS5a. As previously stated, the region of interest for this analysis is 5-100 keV, and one can see from Figure 3.2 that the cosmogenic backgrounds below 19 keV is significantly higher than that of the enriched detectors. DS5a suffered from excessive levels of transient noise which was believed to be partially caused by ground loops [120]. Initial efforts were made to salvage this data set using the transient noise removal technique described in Chapter 3.6. However, even after removing the runs and detectors flagged by the algorithm and applying all data cleansing cuts, a wall of electronic noise remained below 9 keV in the data set's spectrum, see Figure 3.14. This wall obscured the cosmogenic spectral features and would have made the fit in the profile likelihood analysis (described in Chapter 5) extremely difficult. DS0 was excluded because it was taken in a configuration where the shield was not complete. The data sets selected for this analysis are DS1-4, DS5b, DS5c, and DS6a, enriched detectors only, open data only. The blind data is not used in this analysis. No transient noise was identified in the enriched detectors in these data sets, so it was not necessary to cut any runs or detectors. The only transient noise identified in the data was in DS5a (which was not used) and the four runs shown in Figure 3.11 with the natural detector in DS5b. The list of detectors that were used from these data sets and their corresponding livetimes are given in [78]. The exposure for these data sets is summarized in Appendix A, and was taken from [78]. Figure 3.15 shows a comparison of the combined spectrum both before and after the data cleansing cuts are applied. The cuts result in a 85% event reduction in the 5-100 keV ROI, 84% from slow pulses and 1% from pulser retriggers. The reduction of events in the ROI for each data cleansing cut is summarized in Table 3.1. Figure 3.16 shows the final analysis spectrum for the selected data, both below and above

25 keV, with all data cleansing cuts applied. Though enriched detectors have much lower levels of cosmogenic activation than natural detectors, it is still possible to see the tritium beta decay spectrum as well as several cosmogenic peaks.

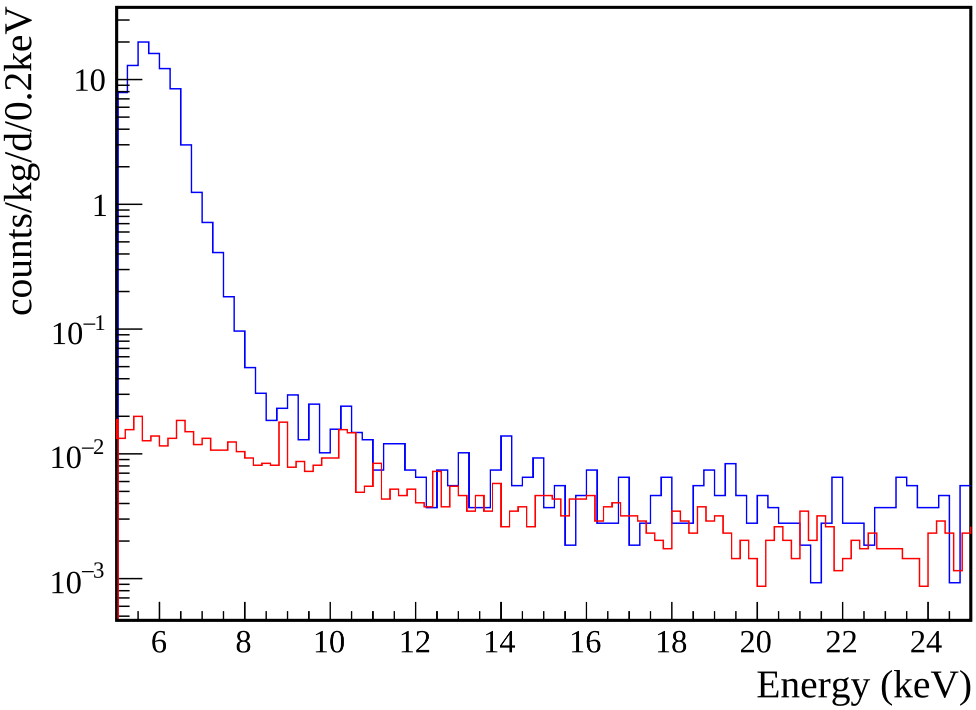

Figure 3.14: In blue: The spectrum of enriched detectors from DS5a after data cleansing cuts and transient noise removal are applied, scaled by the exposure of 1079.5 kg · d. The wall of noise below 9 keV would have required us to raise our analysis threshold had we included DS5a. In Red: The spectrum of enriched detectors from DS1-4, DS5b, DS5c, DS6a open data, scaled by the combined exposure of 3454.7 kg · d.

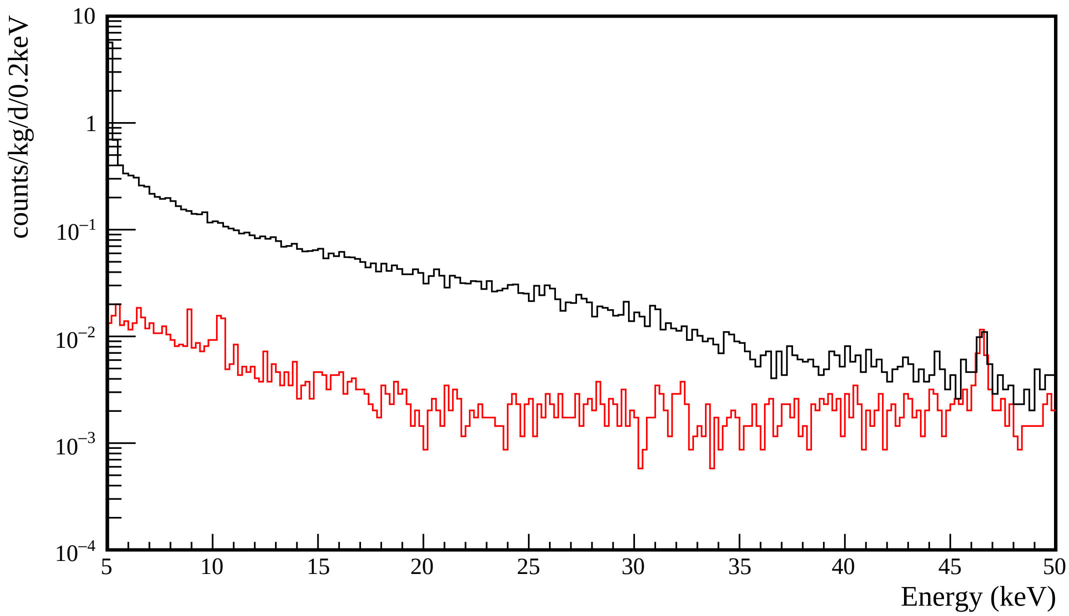

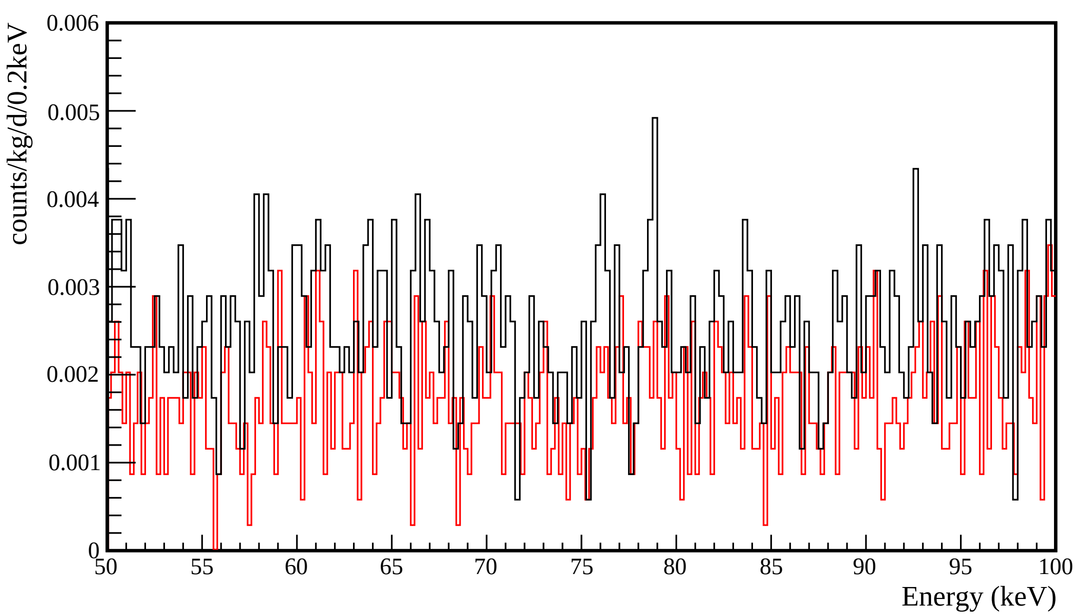

Figure 3.15: The combined spectrum (black) of DS1-4, DS5b, DS5c, DS6a without data cleansing cuts, versus the spectrum (red) with cuts. Scaled by the combined exposure of 3454.7 kg $\cdot$ d. Top: 5-50 keV window. Bottom: 50-100 keV window.

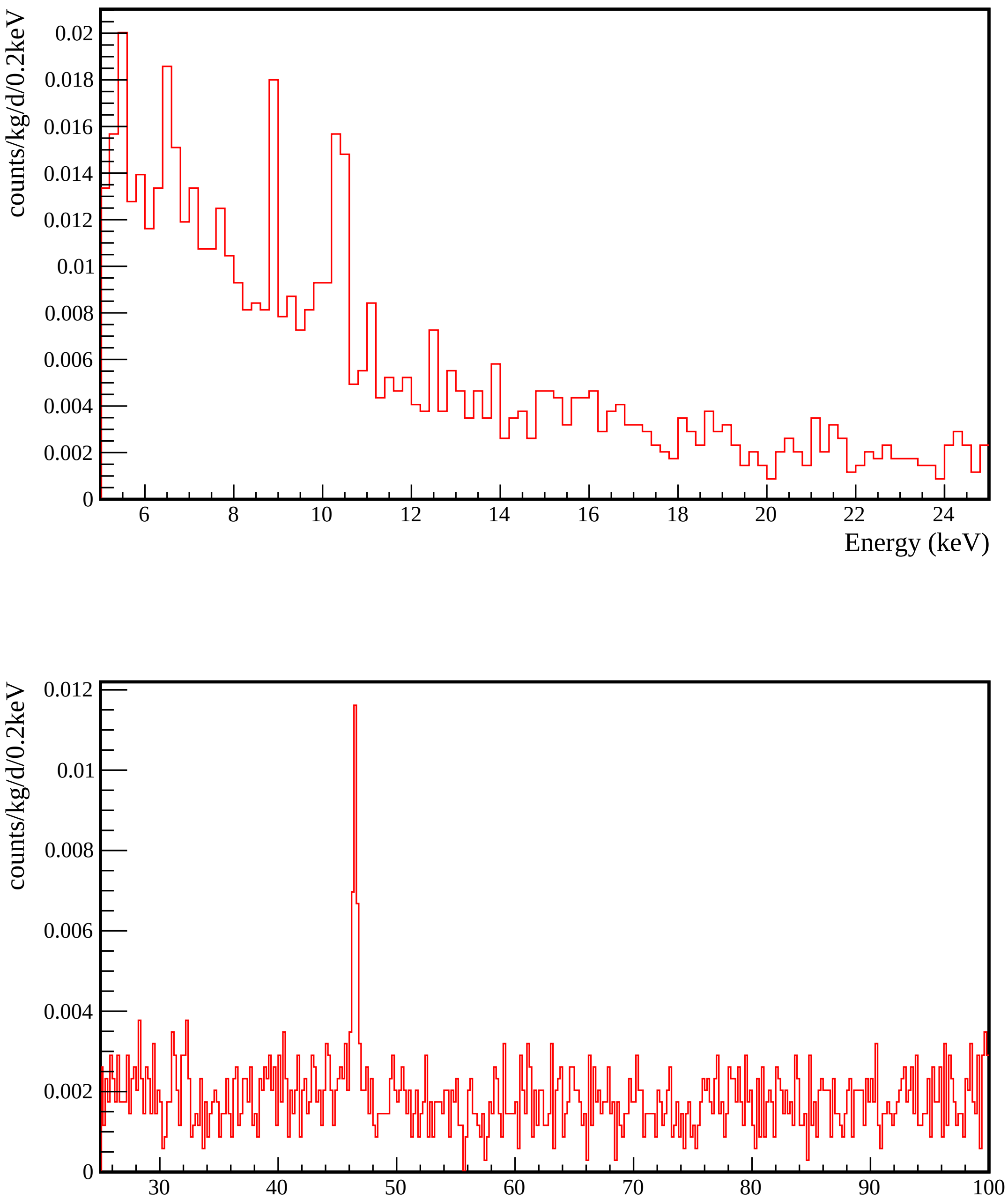

Figure 3.16: Top: Final analysis spectrum in the window 5-25 keV. Visible are the tritium beta decay spectrum which kicks in below 18.6 keV as well as the ^{51}Cr peak at 5.5 keV, ^{55}Fe at 6.5 keV, ^{65}Zn at 8.9 keV, and ^{68}Ge at 10.3 keV. Bottom: Analysis spectrum in the window 25-100 keV. Visible is the linear Compton continuum background as well as the ^{210}Pb X-ray at 46.5 keV from the lead shielding. This spectrum is scaled by the combined exposure of 3454.7 kg $\cdot$ d from the enriched detectors in DS1-4, DS5b, DS5c, DS6a open data.

Event Reduction For Each Cut	
Data Cleansing Cut	Reduction
T/E	84%
Pulser Retrigger	1%
Transient Noise Removal	0%

Table 3.1: The percent event reduction in the 5-100 keV ROI for each data cleansing cut applied. The reduction for transient noise removal is 0% because no transient noise was identified in the enriched detectors in DS1-4, DS5b, DS5c, and DS6a

CHAPTER 4: Systematics

In this chapter, I discuss the three primary systematics pertinent to this analysis: acceptance efficiency, energy resolution, and peak broadening due to the summation of data from different physical configurations. A description is given for how each systematic was estimated. Finally, I present the energy spectrum from Chapter 3 with an acceptance efficiency correction.

Section 4.1: Acceptance Efficiency

A side effect of the data cleansing cuts introduced in Chapter 3 is the sacrifice of a certain fraction of potential dark matter events. To quantify the size of this sacrifice, the fraction of physics events that survive the cuts, called the "acceptance efficiency," is calculated. Because the efficiency varies as a function of energy, it is represented as an energy dependent curve. A requirement for estimating efficiency is a population of pure (or nearly pure) physics events on which to apply the cuts.

4.1.1: Multiplicity 2 Compton scatters of 238 keV ^{212}Pb gammas

To calculate efficiency, a method proposed by R. Henning and implemented by Wiseman and Zhu [123] [54] will be employed that makes use of the Demonstrator's ^{228}Th calibration data. Within the decay chain of ^{228}Th is ^{212}Pb which emits an intense 238 keV gamma line. Small angle Compton scatters of this 238 keV gamma are the events of interest, and a cartoon depicting one is shown in Figure 4.1. The energy deposited by an incident photon as it Compton scatters off of an electron is given by Equation 4.1, which indicates that small angle scatters deposit correspondingly small amounts of energy. Thus, a 238 keV gamma that undergoes a small angle scatter will retain most of its energy.

$$E' = \frac{E}{1 + \frac{E}{mc^2}(1 - cos\theta)} \tag{4.1}$$

Wiseman and Zhu estimate the mean free path of a 238 keV gamma in Germanium to be 14.69 mm, using attenuation coefficients in the XCOM database [124]. A typical radius for a DEMONSTRATOR detector is around 30 mm, and the dead layer is on the order of 1 mm [125], and the transition region is of the order 100μm - 1 mm [31] [93]. From these facts, one can infer that a 238 keV gamma is likely to deposit its energy within the bulk of the detector rather than in the transition region, both when it Compton scatters and when the scattered gamma is absorbed by a second detector. The result is a population of events with very few slow pulses.

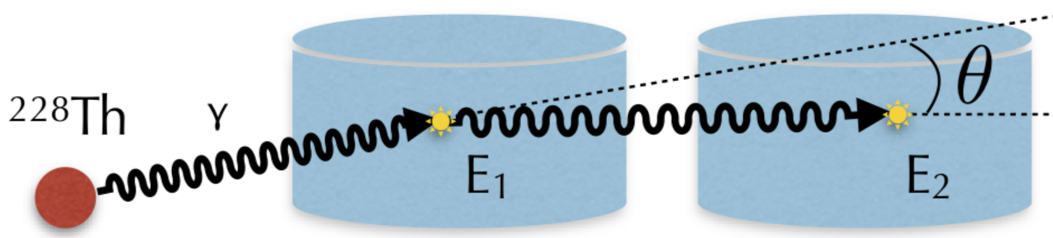

Figure 4.1: Graphic of small angle Compton scatter of a 238 keV ^{212}Pb gamma from the ^{228}Th calibration source.

The procedure for selecting small angle Compton scatters starts by fitting the 238 keV peak in a sum spectrum of multiplicity two events from ^{228}Th calibration data to a Gaussian, as exemplified in Figure 4.2. A multiplicity two event is defined when two hits are registered within two separate detectors within a ± 4 μs time window [123]. This time window is defined by the event builder software for grouping hits together into single events. A cut is then applied that selects multiplicity two events from calibration data with a sum energy of 238 keV $\pm$ 3σ where σ comes from the fit of the sum peak. This process is done for calibration data from each data set. We use the nomenclature "m2s238" to describe these events. A concern naturally arises as to whether a coincidence of two physically unrelated multiplicity one events can artificially register as a multiplicity two event. Wiseman and Zhu calculate from Poisson statistics that contamination from coincidences account for only 1.12% of the multiplicity two population [123] [54]. They also estimate an upper limit of 3.7% slow pulse contamination in the population of m2s238 events, using simulations. Because slow pulses are energy degraded, we expect them to be rejected by requiring the ±3 sigma energy window.

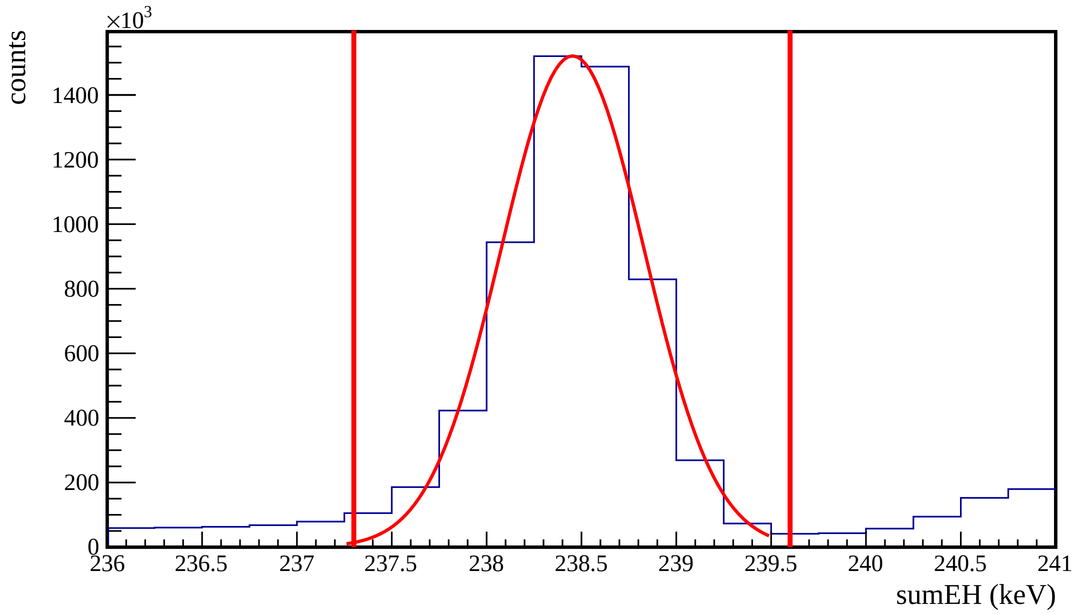

Figure 4.2: Gaussian fit of 238 keV sum peak with ± 3σ in DS1 ^{228}Th calibration data. "sumEH" is the sum energy parameter with a detector threshold cut applied to remove Gaussian noise triggers [123] [54].

Figure 4.3 shows what a spectrum of m2s238 events looks like for the entire array in DS1. From Equation 4.1, the maximum amount of energy deposited by the Compton scatter in a m2s238 event is 123.3 keV, which occurs at $\theta = \pi$. This maximum energy is marked in Figure 4.3 by the vertical red line. The energy spectrum is populated by events from 0 keV to 238 keV, as would be expected from from Compton scatters of a 238 keV gamma.

4.1.2: Calculating Efficiency

Having established a population of nearly pure physics events, it is possible to calculate the efficiency of the data cleansing cuts. A spectrum of the m2s238 events from calibration

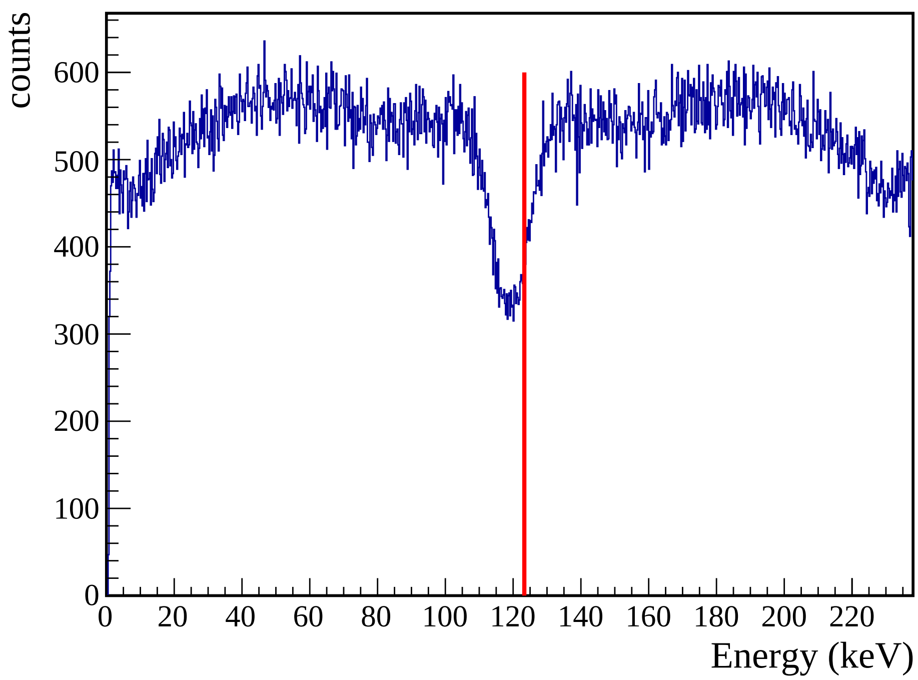

Figure 4.3: Hit spectrum of m2s238 events in DS1. The red line shows the maximum value of energy deposited in the first hit of the Compton scatters: 123.3keV at $\theta = \pi$. This value comes from Equation 4.1.

data that pass the data cleansing cuts and a second spectrum of total m2s238 events without cuts is made for each detector, in each data set. An example is shown in Figure 4.4. The blue spectrum in Figure 4.4 is divided by the red spectrum to give the efficiency curve for the detector in Figure 4.5. The error bars in Figure 4.5 come from Clopper-Pearson 90% confidence intervals.

It is important to note that each event in a m2s238 single detector spectrum is really just one of the two hits (the Compton scatter or the absorption of the scattered gamma) comprising a full m2s238 event, and thus will have a random value of energy between 0 keV and 238 keV. As such, one should not be surprised that the individual detector spectra in Figure 4.4 do not resemble the full DS1 array spectrum in Figure 4.3.

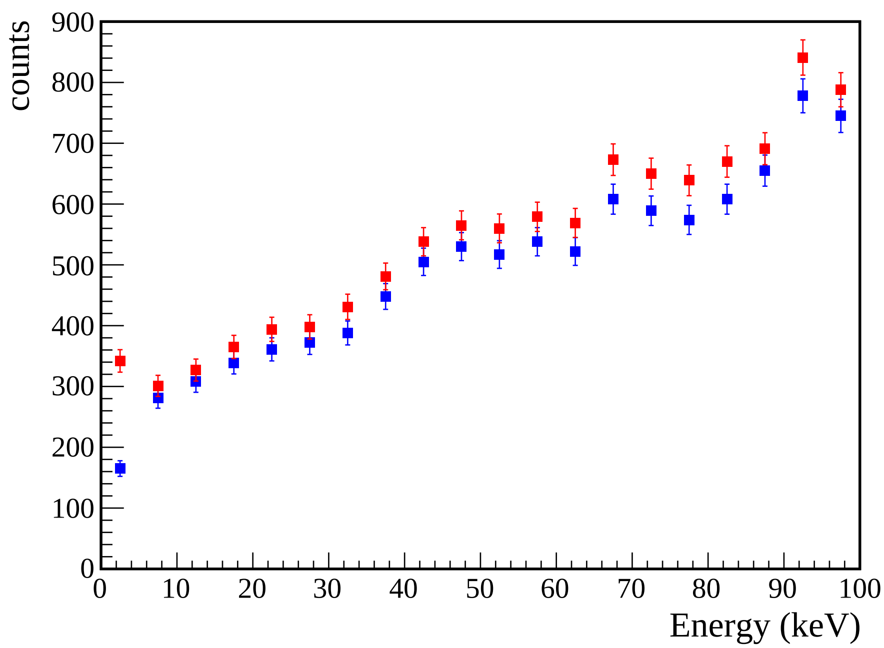

Figure 4.4: In Blue: The spectrum of m2s238 events passing the combined data cleansing cuts for detector C1P1D2 in DS1 with 5 keV binning. In Red: The spectrum of total m2s238 events in DS1 for detector C1P1D2 with 5 keV binning. Error bars are from Poisson counting statistics.

Because different cuts are applied to each detector in each data set, an efficiency curve is generated for each case. The likelihood analysis is performed on a single combined analysis

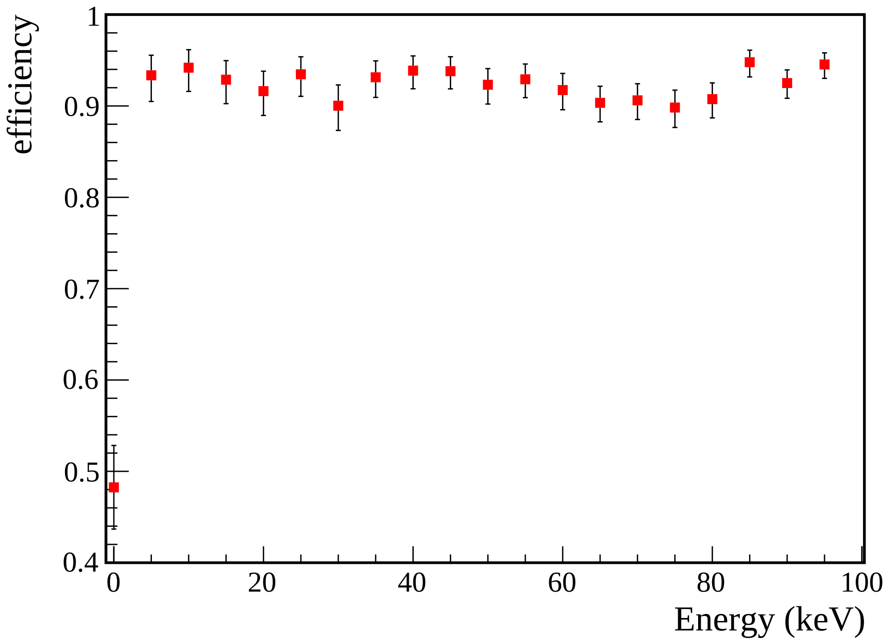

Figure 4.5: Efficiency curve for detector C1P1D2 in DS1. 5 keV binning is used such that the 5-10 keV bin in Figure 4.4 corresponds to the 5 keV data point here, the 10-15 keV bin from Figure 4.4 corresponds to the 10 keV data point here, etc.

spectrum including events from each detector and data set, so it is necessary to somehow combine the individual detector efficiencies into a single combined efficiency for the entire array. One possible approach is to take the average of all the individual detector efficiencies. The problem with this method is that not all detectors contribute equally to the total counts in the combined analysis spectrum, so one would over-estimate the contribution of detectors with low count rate to the overall efficiency. Another possibility is to calculate the efficiency of the whole array over all the data combined rather than treating each detector and each data set separately. In this case, the detectors with the highest count rate would dominate the counts in the combined spectrum and the result would be equivalent to calculating the efficiency of the high rate detectors and applying that efficiency to the low rate detectors, introducing a systematic that is difficult to quantify. The method that this analysis uses is to weight the efficiency of each detector in each data set by it's corresponding active mass and livetime, combine all individual efficiencies together into a weighted sum, and normalize the weighted sum by the total exposure. The result is a weighted average shown in Equation 4.2.

$$\varepsilon = \frac{\sum_{cd} \epsilon_{cd} M_{cd} T_{cd}}{\sum_{cd} M_{cd} T_{cd}} \tag{4.2}$$

ε is the weighted average efficiency, ϵ_{cd} is the efficiency for detector channel c in data set d, M_{cd} is the active mass, and T_{cd} is the live time. Figure 4.6 shows the weighted average efficiency for all combined data sets. Error bars are calculated from propagation of uncertainties, which takes into account the Clopper-Pearson error bars on the individual detector efficiencies as well as the uncertainties on individual detector exposures.

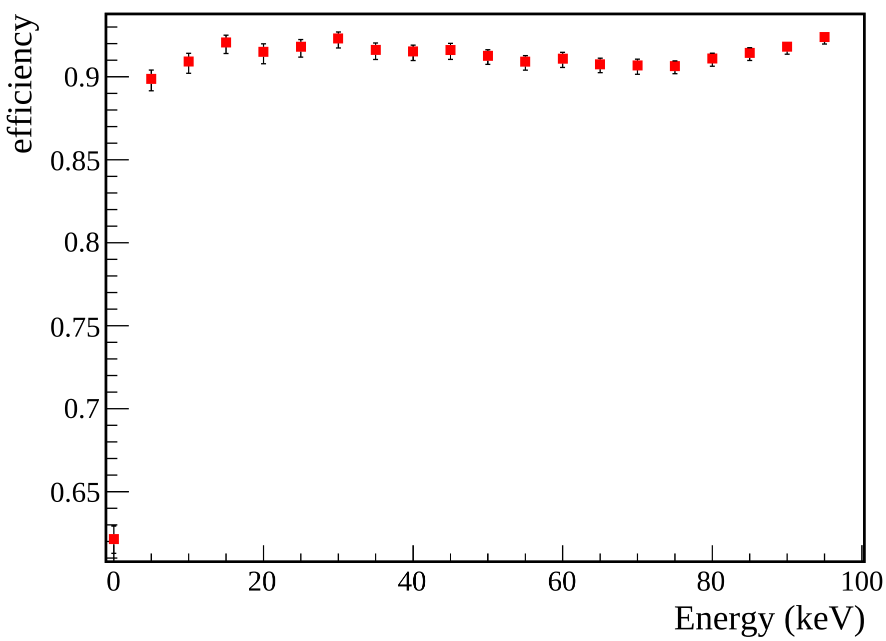

Figure 4.6: Weighted average efficiency for enriched detectors in DS1-4, and 5b-6a combined.

The weighted average efficiency is fitted to an error function in the form of Equation 4.3, where the constants p_0, p_1, and p_2 are floated, E is energy in keV, and η is the efficiency. This efficiency function is used to scale the signal counts in the likelihood analysis. From Figure 4.7, one can see that the efficiency rapidly degrades below 5 keV. The reason for this, as explained in Chapter 3.3, is that the T/E parameter breaks down at energies below 5 keV. This rapid fall-off in efficiency is part of the rationale for setting the analysis threshold at 5 keV.

$$\eta = p_0 \times Erf\left(\frac{E - p_1}{p_2}\right) \tag{4.3}$$

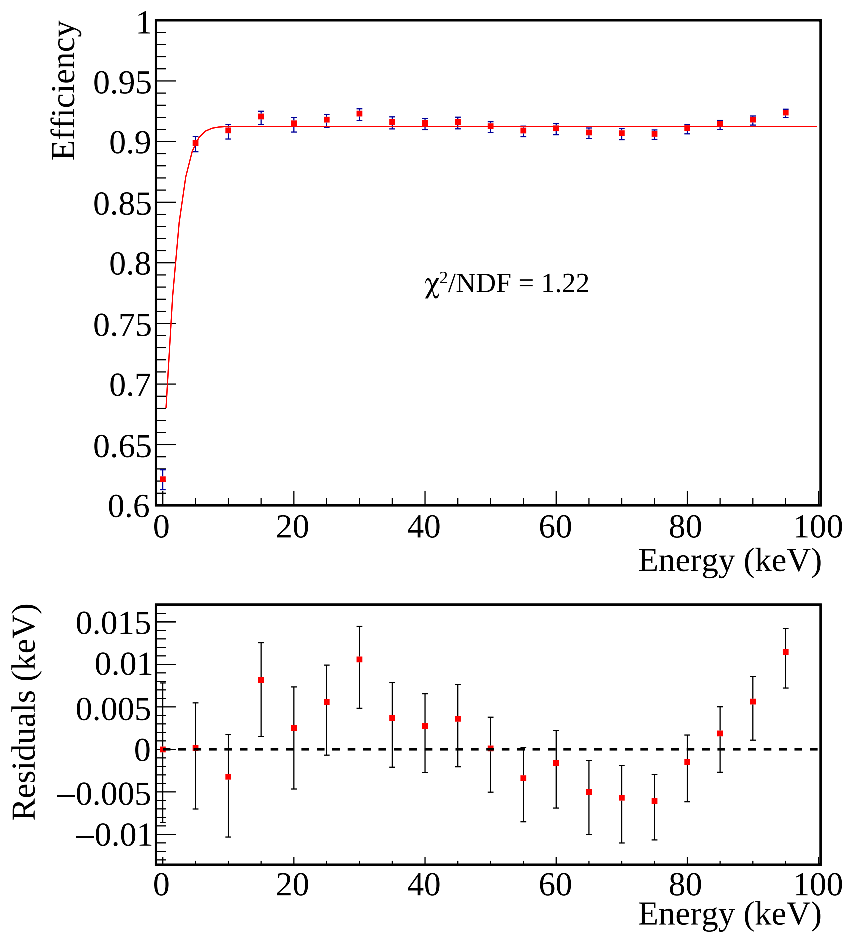

Figure 4.7: Top: Efficiency function that was fitted to Figure 4.6 and used in the likelihood analysis. NDF = 17 (20 data points minus 3 fit parameters). Bottom: Residuals of the fit.

After the weighted average efficiency is calculated, it is possible to obtain the efficiency corrected spectrum in Figure 4.8. Error bars on the corrected spectrum are calculated using the asymmetric error bars on the weighted average efficiency and Poisson counting uncertainties from the uncorrected spectrum.

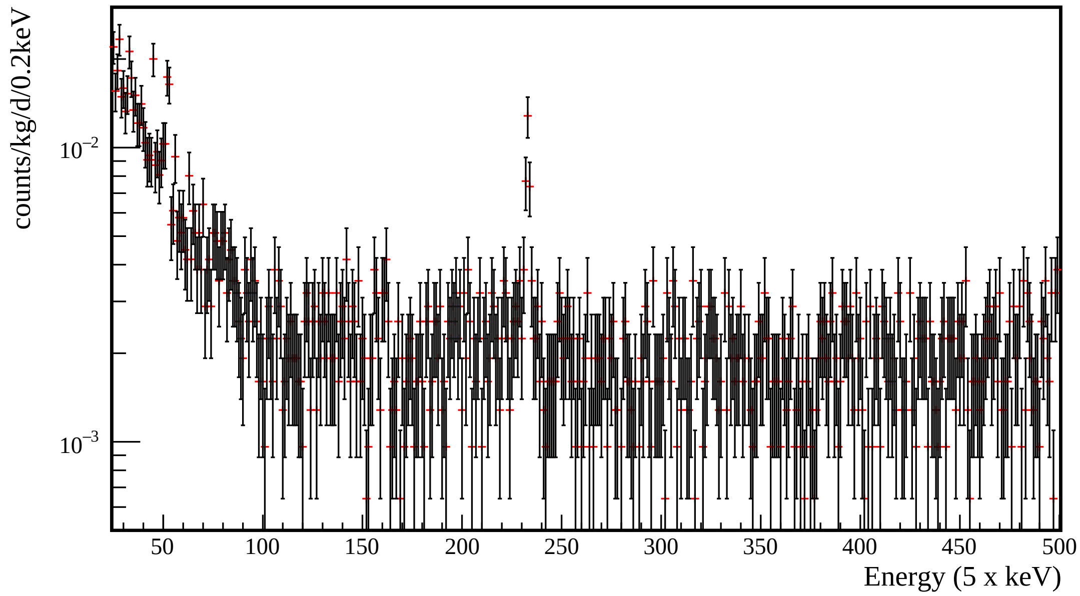

Figure 4.8: Combined efficiency corrected spectrum for data sets used in this analysis, in units of counts/exposure/binning. This spectrum is scaled by the combined exposure of 3454.7 kg $\cdot$ d from the enriched detectors in DS1-4, DS5b, DS5c, DS6a open data.

Section 4.2: Energy Resolution

The energy resolution of a radiation detector determines its ability to resolve peaks that are close in energy. A detector with good energy resolution will have a better ability to distinguish signal from background in a processes like the axioelectric/vector-electric effect and $0\nu\beta\beta$ where the signal manifests as a monoenergetic peak, and this contributes to the sensitivity of the measurement. The formula quoted in Chapter 3 for the energy resolution of germanium detectors is given by Equation 4.4.

$$\sigma_E(E) = \sqrt{\sigma_\epsilon^2 + \langle\epsilon\rangle FE + c^2E^2} \tag{4.4}$$

Characterization of the resolution function was performed by MAJORANA's energy systematics working group [109]. The widths of the 238, 240, 277, 300, 583, 727, 860, and 2614 keV peaks from calibration data were measured with the multi-peak fitter developed by I.

Guinn, and these peak widths were fit to an empirical version of Equation 4.5 of the form:

$$\sigma_E(E) = \sqrt{p_0^2 + p_1^2 E + p_2^2 E^2} \tag{4.5}$$

where the parameters p_0, p_1, and p_2 are floated in the fit. This procedure was performed for each data set individually, but the likelihood analysis described in Chapter 5 was performed on the combined spectrum of enriched detectors from the open data in DS1-4, DS5b, DS5c, and DS6a. Code developed by the analysis coordinator (T. Caldwell) calculated a weighted average FWHM at each peak, where the weights in the sum were taken as the data set exposures. The resolution function was fit to those weighted average FWHM's, as shown in Figure 4.9. Two natural concerns immediately arise. Since the lowest energy peak that was fit in the energy resolution calculation was 238 keV, one wonders if this calibration can be trusted at low energy. The measured FWHM of the 47 keV peak from the combined spectrum of the aforementioned data sets was compared to the predicted FWHM from Equation 4.5 and found to agree within 1%. Secondly, one wonders whether summing multiple data sets together into a single energy spectrum introduces an additional systematic by broadening the peaks. Table 4.1 summarizes the peak width σ of the widest peak in the spectrum, the 2614 keV line, for each data set and for the weighted average. The peak width of the weighted average, 2.98 keV, is less than 1% wider than the widest peak among the individual data sets, 2.96 keV. So this systematic, if it exists, is a sub-dominant effect and will be ignored in this analysis.

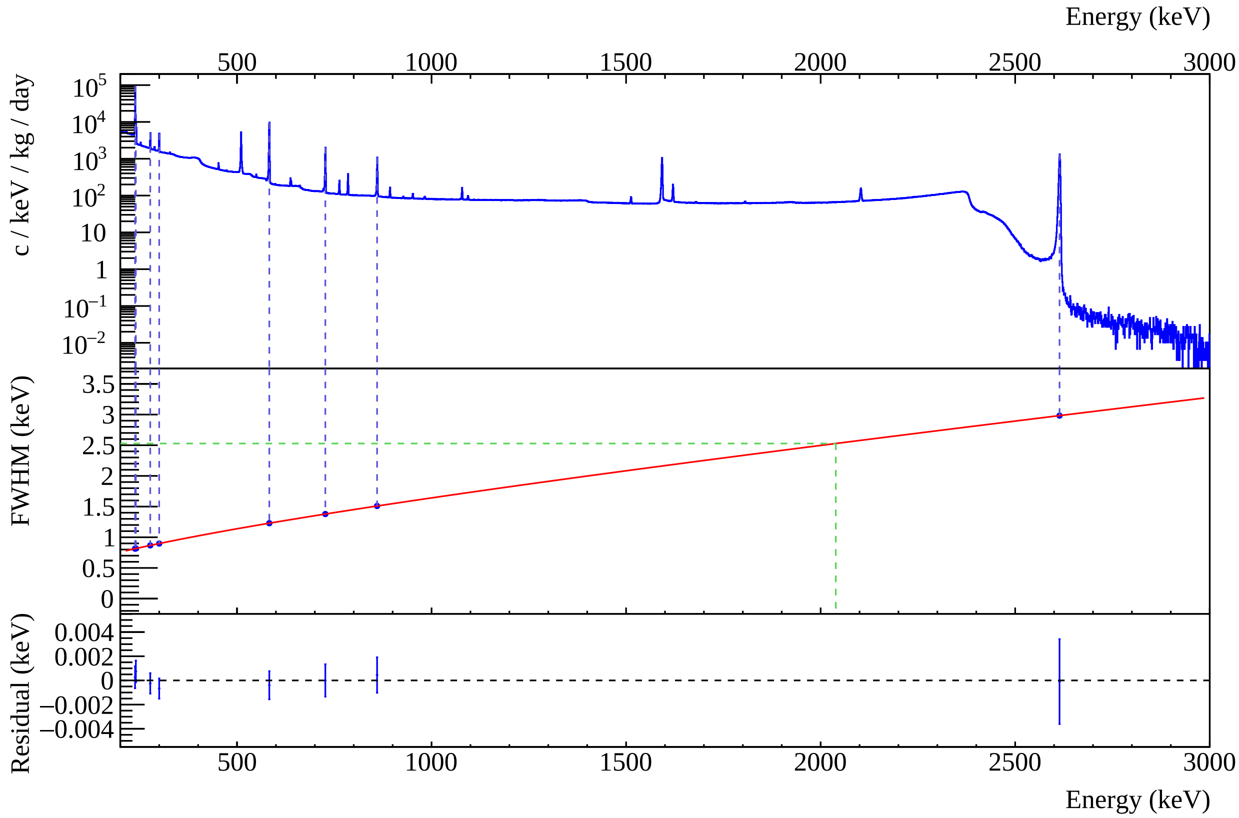

Figure 4.9: Energy resolution function fit to peaks in summed calibration spectrum.

Widths of the 2614 keV Peak by Data Set		
data set	σ_E	σ_{σ_E}
1	1.223	0.001
2	1.255	0.001
3	1.246	0.001
4	1.156	0.001
5b	1.242	0.001
5c	1.224	0.001
6	1.208	0.001
sum	1.267	0.002

Table 4.1: Peak widths for the 2614 keV line broken down by data set.

CHAPTER 5: Likelihood Analysis and Results

I describe the general strategy of maximum likelihood and profile likelihood analysis and how they are pertinent to this work, borrowing notation from [126] and [127]. A model describing the distribution of signal and background counts is constructed and then fit to the combined energy spectrum of open data from DS1-4, DS5b, DS5c, and DS6a using a binned, extended maximum likelihood in RooFit [128]. The upper limit for the 90% confidence interval on signal counts as a function of energy is calculated and used to construct the 90% upper limits on the coupling constants for pseudoscalar and vector dark matter.

Section 5.1: Maximum Likelihood

Suppose we have a set of measurements $\{x_i\}$, such as counts in an energy histogram, which are assumed to follow some probability density function (PDF) P. This density function could be something like a Gaussian peak superimposed on a linear background, or some spectral shape without an analytic, functional expression. And suppose there is a parameter of interest, θ, that we want to characterize, such as counts under the Gaussian peak. In addition to the parameter of interest, there will also be a set of parameters ν_i that we do not care about but which nonetheless come with the PDF, such as the mean μ and width σ of the Gaussian peak. If these nuisance parameters are represented by the vector $\vec{\nu}$, then the PDF can be expressed as $P\left(x_i; \theta, \vec{\nu}\right)$. The likelihood function will be the product of the PDF over the range of measurements, and is a function of θ and $\vec{\nu}$.

$$L\left(\theta, \vec{\nu}\right) = \prod_{i}^{n} P\left(x_i; \theta, \vec{\nu}\right) \tag{5.1}$$

Another way to think of the likelihood function is the joint probability that each data point

$\{x_i\}$ is sampled from our PDF.

The goal of the maximum likelihood method is to find the most probable value of θ, or stated another way, to find the value of θ that maximizes the likelihood function. It is computationally easier to deal with sums rather than products, so rather than maximizing the likelihood function $L(\theta, \vec{\nu})$, we minimize the the negative log likelihood function $-\log L(\theta, \vec{\nu})$. Since log functions are monotonic, we can be sure that the critical points and general characteristics of the likelihood function will be preserved. If additional information is known about a parameter, then the likelihood function can be multiplied by a constraint term. For example, if the mean of ν_i of the Gaussian peak is known to be within the range $\bar{\nu}_i \pm \sigma_{v_i}$, assuming Gaussian error bars, then we can multiply $L(\theta, \vec{\nu})$ by the following:

$$C_{\nu_i}\left(\nu_i; \bar{\nu}_i, \sigma_{\nu_i}\right) = A \cdot \exp\left(\frac{\left(\nu_i - \bar{\nu}_i\right)^2}{2\sigma_{\nu_i}^2}\right) \tag{5.2}$$

The standard approach to maximum likelihood is to normalize the PDF and the data to 1. For an extended maximum likelihood analysis, which will be employed here, the normalization is allowed to vary as a free parameter. This technique is useful when one is interested in the number of counts in a particular distribution, and not just in the distribution's shape. However, one must multiply the likelihood function by the Poisson probability of observing $S + B$ events when n are expected, S and B being the number of signal and background counts respectively.

$$L_{ext}(S, B) = \frac{(S+B)^n}{n!} e^{S+B} \tag{5.3}$$

Section 5.2: Profile Likelihood

Sometimes, it is desirable to know more than just the most probable value of θ, but also an upper limit on its allowed value for the given data. For this purpose, it is useful to write the profile likelihood ratio which is the value of the likelihood function scaled by the global extremum value when all other parameters have been optimized. This ratio can be used as a test statistic.

$$\lambda(\theta) = \frac{L\left(\theta, \hat{\hat{\vec{\nu}}}\right)}{L\left(\hat{\theta}, \hat{\vec{\nu}}\right)} \tag{5.4}$$

where $L\left(\hat{\theta}, \hat{\vec{\nu}}\right)$ is the global extremum and $L\left(\theta, \hat{\hat{\vec{\nu}}}\right)$ is the conditional maximum where L has been maximized for a given θ. One should note that λ is only a function of θ. We take the negative log of the profile likelihood ratio, $-\log\lambda(\theta)$, for the same reason that we took the negative log likelihood function. According to Wilk's theorem [129], the quantity $-\log\lambda(\theta)$ follows a chi-square distribution with number of degrees of freedom (NDF) equal to the number of parameters of interest. In our case, we are only interested in θ so $NDF = 1$.

$$\frac{\chi^2}{2} = -\log\lambda(\theta) \tag{5.5}$$

We then scan upwards from the minimum value $\hat{\theta}$, which corresponds to the minimum of the χ^2 distribution, until $-\log\lambda(\theta)$ reaches the desired χ^2 confidence level, as shown in Figure 5.1. The $100(1-\alpha)\,\%$ confidence interval (CI) corresponds to $\frac{\chi^2_\alpha}{2}$. For the 90% CI used here:

$$\frac{\chi^2_{0.1}}{2} = \frac{2.71}{2} = 1.355 \tag{5.6}$$

In the event of a non-physical best fit value, such as $\hat{\theta} < 0$, one can define a new profile likelihood curve:

$$-\log\lambda'(\theta) = -\log\lambda(\theta) + \log\lambda(0)\,|\, -\log\lambda'(\theta = 0) = 0 \tag{5.7}$$

The upper limit is then found by scanning from $-\log\lambda'(\theta = 0)$ upward on the χ^2 curve until the desired CI is reached.

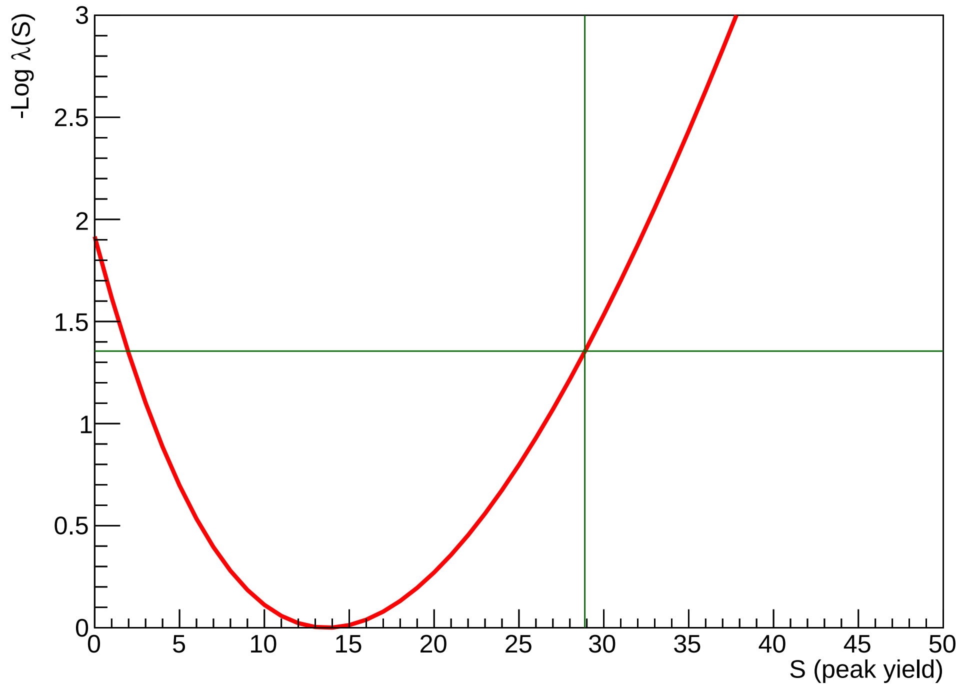

Figure 5.1: A profile curve for a 15 keV particle in the combined spectrum of enriched detectors from DS1-4,5b-6. The green lines show the 90% confidence limit.

Section 5.3: The Signal and Background Models

As discussed in Chapter 1.2.3, bosonic dark matter has negligible kinetic energy and interacts with ordinary matter via the axioelectric or vector-electric mechanism. The expected signal in the spectrum is a monoenergetic peak. We will model this peak as a Gaussian.

$$P_{sig}\left(E_i; E_{mean}, \sigma_E\right) = \frac{1}{\sqrt{2\pi}\sigma_E} \exp\left[\frac{-\left(E_i - E_{mean}\right)^2}{2\sigma_E^2}\right] \tag{5.8}$$

E_{mean} is the mean of the signal peak and σ_E is the width of the signal peak. σ_E is floated, and its initial guess comes from the energy resolution function, discussed in Chapter 4.2. The floated σ_E is constrained by its uncertainty, as will be explained shortly.

There are multiple components to the background model, including the tritium beta decay spectrum, the linear background, and five background peaks. Figures 3.16 and 4.8 show the beta decay spectrum for tritium, which kicks in below 20 keV. The PDF describing the tritium spectral shape can be written [130]:

$$P_T\left(E; m_e, E_0\right) = C \cdot F\left(E, Z=2\right) \cdot p \cdot \left(E + m_e\right) \cdot \left(E_0 - E\right)\sqrt{\left(E_0 - E\right)^2 - m_\nu^2} \tag{5.9}$$

where C is a normalization factor, F is the Fermi function that describes the Coulomb force between the emitted electron and and the final state nucleus, p is the momentum of the outgoing electron, m_e and m_ν are the electron and neutrino masses respectively, and E_0 is the endpoint energy of the beta decay spectrum, 18.6 keV. Because the Fermi function is complex valued, it is not possible to write a closed form PDF for the beta decay spectrum. As an alternative, the shape of the tritium spectrum was sampled in 0.2 keV binning [131] and saved as a histogram, with it's normalization allowed to float.

The flat continuum described in Chapter 3.1 was modeled by a straight line:

$$P_{linear}\left(E_i; m, b\right) = \frac{1}{b}\left[mE_i + b\right] \tag{5.10}$$

where b is the linear background count rate and m is the slope of the line. Both b and m were floated. The five background peaks are the ^{51}Cr peak at 5.5 keV, ^{55}Fe at 6.5 keV, ^{65}Zn at 8.9 keV, ^{68}Ge at 10.3 keV and ^{210}Pb at 46.5 keV. Each peak is modeled by a Gaussian of the same form as the Equation 5.8, where E_{mean} and σ_E are allowed to float, but their initial guesses come from the true values of the peak energies and the energy resolution function respectively. The full spectral model is of the form:

$$P_{spec}\left(E_i; \Xi, \vec{v}\right) = \frac{\sum_{n\in\Xi} n \times P_n\left(E_i; \vec{v}\right)}{\sum_{n\in\Xi} n} \tag{5.11}$$

Ξ is the set $\{\eta_E S, T, B, C, F, Z, G, P\}$ where η_E is the acceptance efficiency, S is the yield in signal peak, T is tritium counts, B is counts from the linear background, C is counts under the ^{51}Cr peak, F is ^{55}Fe, Z is ^{65}Zn, G is ^{68}Ge, and P is ^{210}Pb. The vector $\vec{v} = (\sigma_E, \eta_E)$ treats the energy resolution σ_E and acceptance efficiency as nuisance parameters. The spectral component of the likelihood function is given by Equation 5.12. Figure 5.2 shows the best fit of the spectral model to the data, assuming a signal peak at a randomly chosen energy within the 5-100 keV region of interest, 15 keV.

$$L_{spec}\left(S, \vec{v}\right) = \prod_i P_{spec}\left(E_i; S, \vec{v}\right) \tag{5.12}$$

Section 5.4: Constraints

As previously mentioned, constructing an extended likelihood function requires one to incorporate the Poisson probability term to ensure that the signal and background counts are properly anti-correlated and that the proper number of counts in the data are attributed

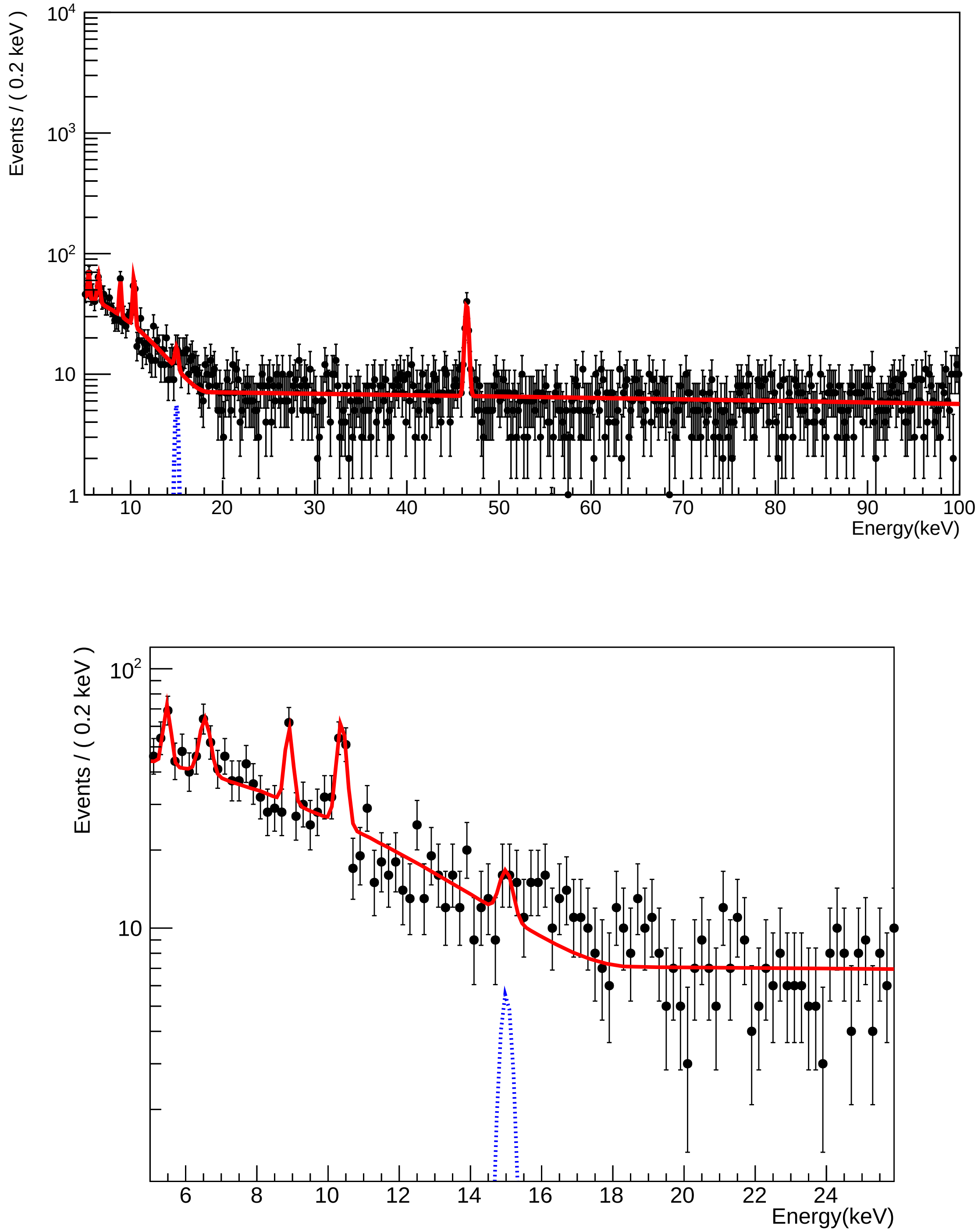

Figure 5.2: Top: Best fit of the full spectral model to the data, assuming a signal peak at 15 keV in blue. The red curve incorporates the linear background, the tritium spectrum, the signal peak, and the five background peaks at ^{51}Cr, ^{55}Fe, ^{65}Zn, ^{68}Ge, and ^{210}Pb. Bottom: A zoom-in of the spectral model fit from 5 keV to 25 keV.

to each. For our model, the Poisson term looks like the following:

$$L_{exended}\left(\eta_E S, T, B, C, F, Z, G, P\right) = \frac{\left(\xi\right)^n}{n!}e^{\xi} \tag{5.13}$$

where ξ is the sum $\eta_E S{+}T{+}B{+}C{+}F{+}Z{+}G{+}P$. Since we can estimate the uncertainty on the energy resolution and the acceptance efficiency, we can incorporate a constraint term similar to Equation 5.2 on the vector $\vec{v} = (\sigma_E, \eta_E)$. Since we are constraining a vector, the Gaussian from Equation 5.2 will be replaced with a multi-variate Gaussian:

$$L_{constraint}\left(\vec{v}; \vec{\bar{v}}, \Sigma^2\right) = \frac{1}{\sqrt{\left|2\pi\Sigma_{ij}^2\right|}} \exp\left(-\frac{1}{2}\left(v_i - \bar{v}_i\right)\Sigma_{ij}^2\left(v_i - \bar{v}_i\right)\right) \tag{5.14}$$

where $\vec{\bar{v}}_i$ contains the mean values of the quantities in $\vec{v}$. The Σ_{ij}^2 is a covariance matrix of the form:

$$\Sigma_{ij}^2 = \begin{pmatrix} \sigma_{\sigma_E}^2 & 0 \\ 0 & \sigma_{\eta_E}^2 \end{pmatrix} \tag{5.15}$$

The total likelihood is given by Equation 5.16. Table 5.1 contains a summary of the parameters used in the likelihood analysis.

$$L = L_{extended} \times L_{spec} \times L_{constraint} \tag{5.16}$$

Section 5.5: Bosonic Dark Matter Interactions

First we will consider the case of pseudoscalar particles, or ALP's. The dark matter flux $\Phi_A\left(m_A\right)$ depends on the mean dark matter particle velocity relative to earth v_A, the dark matter halo density ρ_A, and the ALP mass m_A. $\Phi_A\left(m_A\right)$ can be written [132]:

$$\Phi_A\left(m_A\right) = \rho_A \frac{v_A}{m_A} \tag{5.17}$$

Fit parameters in the likelihood analysis.					
parameter	description	initial value	final value	float range	notes
S	dark matter signal counts	0.5	7.1	0-50000	range limited in RooFit
T	tritium counts	9000	7808	0-100000	range limited in RooFit
B	linear background counts	4400	4182	0-100000	range limited in RooFit
C	^{51}Cr counts	100	81	0-100000	range limited in RooFit
F	^{55}Fe counts	600	642	0-100000	range limited in RooFit
Z	^{65}Zn	300	99	0-100000	range limited in RooFit
G	^{68}Ge	300	414	0-100000	range limited in RooFit
P	^{210}Pb	100	96	0-100000	range limited in RooFit
m	linear background slope	2×10^{-5}	-3×10^{-3}	-1.0-1.0	range limited in RooFit
η_E	acceptance efficiency	Eqn. 4.3	n.a.	$\pm\sigma_{\eta_E}$	constrained by $L_{constraint}$
σ_E	energy resolution	Eqn. 4.5	n.a.	$\pm\sigma_{\sigma_E}$	constrained by $L_{constraint}$

Table 5.1: Parameters that were floated in the likelihood analysis. Final values from the fit were calculated for a 15 keV dark matter particle, the same mass used to generate Figures 5.1 and 5.2.

Using $v_A \approx 230\ km/s$ and $\rho_A \approx 0.3\ GeV/cm^3$ [133], equation 5.17 can be rewritten [67]:

$$\Phi_A\left(m_A\right) = 7.8 \times 10^{-4}\left(\frac{1}{m_A}\right) \cdot \beta\left[/barn/day\right] \tag{5.18}$$

where $\beta \approx 0.001$ from the non-relativistic halo velocity [132].

The strength of the signal from bosonic dark matter in our energy spectrum is expected to be the product of flux Φ_A, the axio-electric cross section ρ_{Ae}, and exposure MT. As discussed previously, the peak shape of the signal is expected to be a Gaussian of the form of Equation 5.8, scaled by the acceptance efficiency $\eta\left(E\right)$ which is a function of energy. Taking into account the spectral shape of the signal and the efficiency, the differential rate for bosonic dark matter becomes:

$$\frac{dN}{dE}\left(E; m_A\right) = \Phi_A \sigma_{Ae} \sum_i M_i T_i \frac{\eta\left(E\right)}{\sqrt{2\pi}\sigma_E} \exp\left[\frac{-\left(E - E_A\right)^2}{2\sigma_E^2}\right] \tag{5.19}$$

The summation covers each detector in each data set used in the analysis. From [132], the axio-electric cross section σ_{Ae} can be rewritten in terms of the energy-dependent photoelectric cross section in germanium, $\sigma_{pe}\left(E\right)$.

$$\sigma_{Ae}\left(E_A\right) = \sigma_{pe}\left(E_A\right) \frac{g_{Ae}^2}{\beta} \frac{3E_A^2}{16\pi\alpha m_e^2}\left(1 - \frac{\beta^{2/3}}{3}\right) \tag{5.20}$$

α is the fine structure constant 1/137, m_e is the mass of an electron in units if keV, and g_{Ae} is the axio-electric coupling constant, which is the parameter we wish to set a limit on. As previously stated, $\beta \approx 0.001$. So the energy E_A of the pseudoscalar particle can be rewritten.

$$E_A = \sqrt{m_A^2 + \gamma^2 m_A^2 \beta^2} \approx m_A \tag{5.21}$$

So each instance of E_A in Equations 5.19 and 5.20, whether it be as a variable or argument of a function, can be replaced with m_A. The photoelectric cross section in germanium is shown in Figure 5.2 and was generated by a collaborator [67].

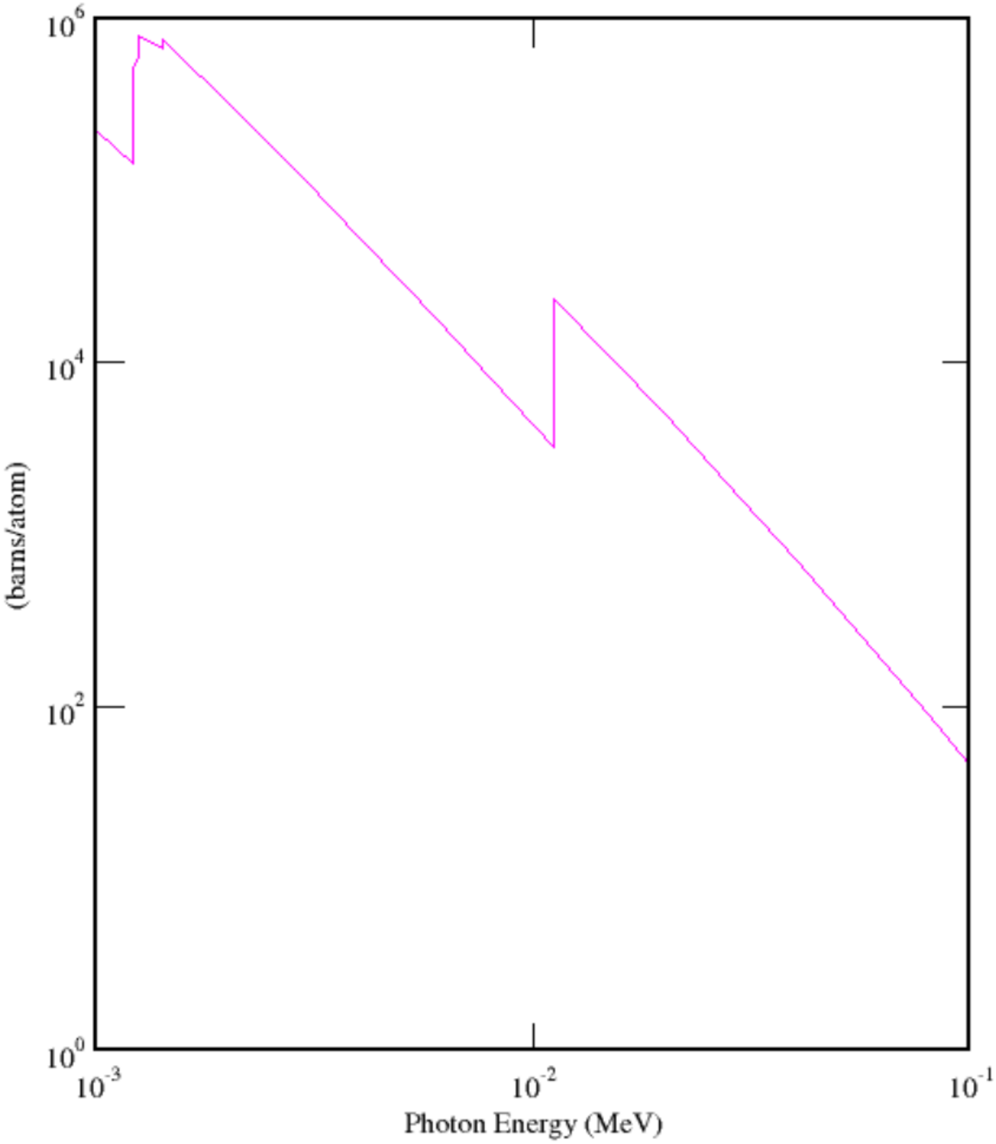

Figure 5.3: Photoelectric absorption cross section in germanium versus energy. The cusp at 10.36 keV is due to K-shell resonance. Figure generated by K. Vorren in [67] with a tool from [124].

For vector particles, Equation 5.19 holds but with Φ_A replaced by the flux of vector particles $\Phi_V(m_V)$, E_A replaced by the energy of the vector particle E_V, m_A by the mass of the vector particle m_V, and σ_{Ae} replaced by the vector-electric cross section σ_{Ve}. Following the formalism presented in [134], we can rewrite the product of the vector dark matter flux Φ_V and vector-electric cross section σ_{Ve} as such:

$$\Phi_V(m_V)\,\sigma_{Ve}(m_V) = \frac{4\times10^{23}}{m_V}\frac{\alpha'}{\alpha}\frac{\sigma_{pe}(m_V)}{A}\,[/kg/d] \tag{5.22}$$

A is the atomic mass of the germanium detectors enriched to 88% in ^{76}Ge, α is the fine structure constant, and α' is the modified fine structure constant for massive dark photons (or vector bosonic dark matter).

$$\alpha' = \frac{(e\kappa)^2}{4\pi} \tag{5.23}$$

κ is the effective coupling constant of dark vector bosons to the Standard Model and e is the charge of the electron. Using natural units from high energy physics where $\epsilon_0 = \hbar = c = 1$, the ratio $\frac{\alpha'}{\alpha}$ can be rewritten:

$$\frac{\alpha'}{\alpha} = \kappa^2 \tag{5.24}$$

This is a useful conversion because some authors [135] [136] choose to express their exclusion limits for dark vector bosons in terms of κ rather than $\frac{\alpha'}{\alpha}$.

Section 5.6: Updated Limits

Figures 5.4 and 5.5 show the updated 90% exclusion curves for g_{Ae} and α'/α as a function of particle mass respectively, with a comparison to limits from other experiments. In the combined energy spectrum of enriched detectors from DS1-4 and DS5b-6a, no evidence was found for an anomalous peak consistent with bosonic dark matter. Within the range 5-20 keV, the limit was calculated in 0.2 keV steps to provide fine enough binning for fitting the tritium spectrum and cosmogenic background peaks. From 20 keV to 100 keV, the limit was calculated in 1 keV steps because the only features in this energy range are the linear background and the 46.5 keV ^{210}Pb peak, so fine binning was not needed.

For pseudoscalar particles, we set the world-leading limit from approximately 25 keV to 40 keV. Above 40 keV, the most stringent limit is set by XMASS [137] due to their exceptional background rate of 5×10^{-4} kg^{-1}keV^{-1}d^{-1} and sizable exposure of 800 live-days with 327 kg of liquid xenon, although their fiducial cut results in an active mass lower than this quoted number. Below 25 keV, the leading limit is set by PandaX [138] with an immense exposure of 27,000 kg $\cdot$ d and a quoted background of $2.0 \cdot 10^{-3}$ evt/kg/d. By comparison, the exposure of the data used in this analysis is 3,454.7 kg $\cdot$ d with a linear background rate of $7.0 \cdot 10^{-3}$ kg^{-1}keV^{-1}d^{-1} in the 20-100 keV energy window. Our most stringent limit was $g_{Ae} < 2.00 \times 10^{-13}$ at 11.6 keV.

For vector particles, we set the leading limit from 5 to 8 keV, from 11 keV to 15 keV, and from 17 keV to 37 keV. Above 37 keV, the leading limit is set by XMASS. Our limit rises above the Xenon100 curve [139] below 11 keV due to the aforementioned cosmogenic peaks in this region, and from 15 keV to 17 keV because of a statistical fluctuation. Our most stringent limit on vectors was $\alpha'/\alpha < 1.91 \times 10^{-28}$ at 11.6 keV.

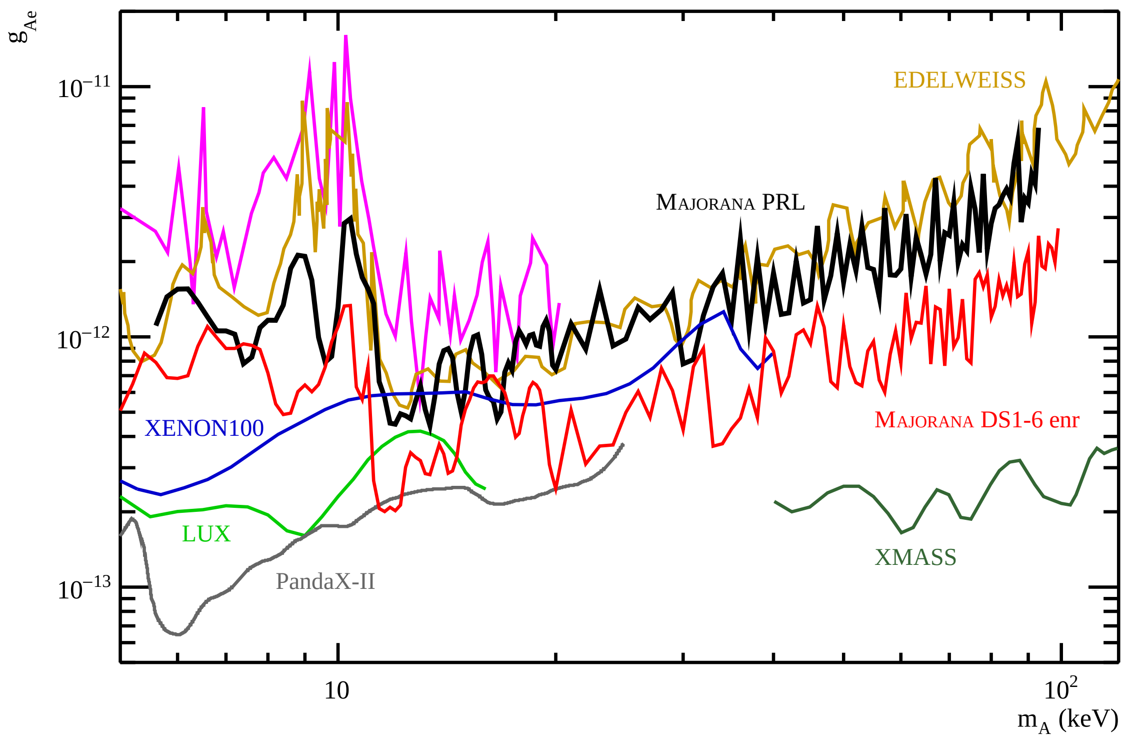

Figure 5.4: The upper limit from the 90% CI on g_{Ae} as a function of ALP mass m_A. The curve in black is the limit previously set by MAJORANA with the commissioning data [67]. In red is the updated limit from this work. Also shown are limits from XMASS [137], PandaX [138], Edelweiss [136], Xenon-100 [139], CDEX [140], and LUX [141] The most stringent MAJORANA limit from this analysis is $\alpha'/\alpha < 1.91 \times 10^{-28}$ at 11.6 keV.

.

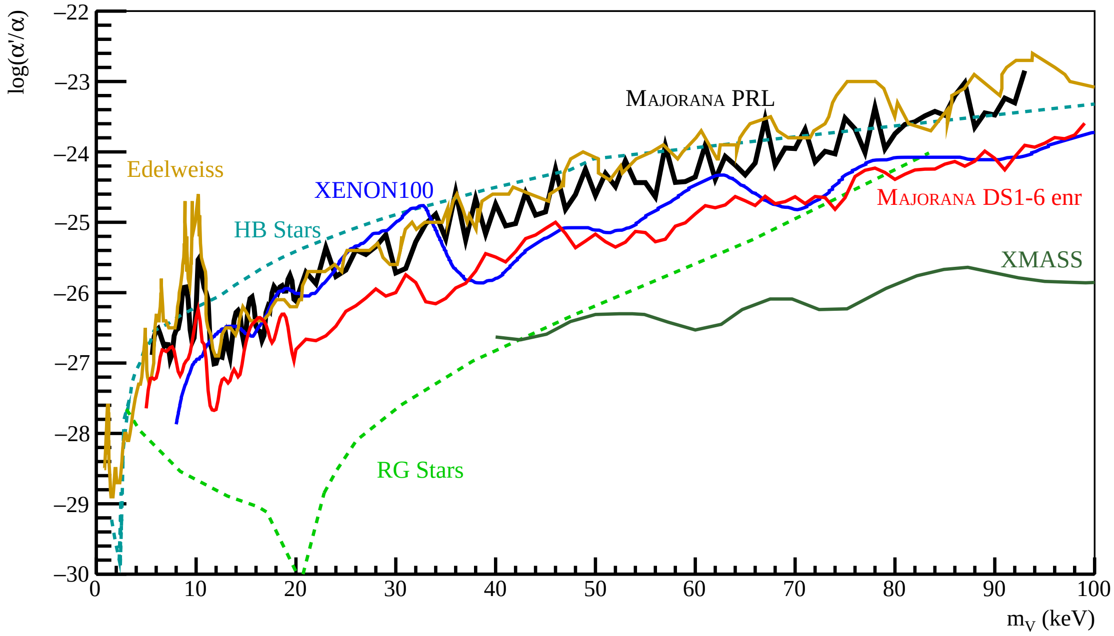

Figure 5.5: The upper limit from the 90% CI on α'/α as a function of vector mass m_V. The curve in black is the limit previously set by Majorana with the commissioning data [67]. In red is the updated limit from this work. Also shown are limits from XMASS [137], Edelweiss [136], and Xenon-100 [139]. Dashed lines show model dependent astrophysical limits from horizontal branch stars (cyan) [134] and red giant stars (green) [135]. The most stringent Majorana limit from this analysis is $\alpha'/\alpha < 1.91 \times 10^{-28}$ at 11.6 keV.

CHAPTER 6: Conclusion

Section 6.1: Overview

The case for dark matter is compelling and comes from a variety of indirect observational evidence, such as galactic rotation curves, gravitational lensing, and the CMP temperature power spectrum. WIMP's have traditionally been the favored dark matter candidate because of the "Wimp Miracle." However, newer generations of ever more sensitive WIMP detection experiments are rapidly approaching the neutrino floor, motivating an interest in alternative theories. Axions and generic bosonic dark matter are an interesting alternative to WIMP's. Dark vector bosons, or massive dark photons, are especially interesting because current generation dark matter and double-beta decay experiments are competitive with the weak model dependent astrophysical and cosmological constraints on vectors. Due to the extremely small cross sections involved, experiments searching for bosonic dark matter must have very low backgrounds.

Though built as a double-beta decay experiment, the Majorana Demonstrator is an ideal platform for probing bosonic dark matter. The carefully controlled environment, compact shield, and location deep underground at SURF reduces environmental environmental backgrounds like radon, fast neutrons from the cavern walls, as well as cosmic rays. Careful handling of the enriched detectors minimizes cosmogenic activation. Contaminants from the thorium and uranium decay chains are minimized within the structural materials closest to the germanium detectors. Their superior energy resolution, low energy thresholds, and low levels of electronic noise make the PPC style germanium detectors deployed in the Demonstrator well suited to probing keV scale physics.

Pulse shape analysis tools and run/detector selection tools were developed to mitigate various sources of background, from energy degraded events to various kinds of electronic artifacts. Systematics such as energy resolution and the acceptance efficiency of the PSA-based data cleansing cuts were characterized. A check was done to ensure that summing energy spectra from different data sets did not introduce an additional systematic by widening peaks.

Data from the enriched detectors in data sets 1-4 and 5b-6a were combined into an energy spectrum, with 3454.7 kg $\cdot$ d of exposure and a background rate of $7.0 \cdot 10^{-3}$ kg^{-1}keV^{-1}d^{-1} in the 20-100 keV linear background energy window. A profile likelihood analysis was performed on this spectrum, resulting in world-leading confidence limits on both pseudoscalar and vector dark matter. The most stringent limits of $g_{Ae} < 2.00 \times 10^{-13}$ for pseudoscalars and $\alpha'/\alpha < 1.91 \times 10^{-28}$ for vectors were set at 11.6 keV.

Section 6.2: Outlook

Before this material is published, the Majorana collaboration has agreed that we want to extend this analysis to include our blinded data. This would introduce an additional 4330 kg $\cdot$ d of exposure from enriched detectors. Based upon our sensitivity estimates, it is expected that this additional exposure would improve the limit on ALP's and vectors by 20% and 45% respectively. To do this, it will be necessary to apply the automated run and detector selection described in Chapter 3.6 to this blind data. Depending on the amount and nature of the transient noise present, it might even be necessary to improve the algorithm for run and detector selection. Improvements this algorithm might conceivably allow us to utilize DS5a.

APPENDIX A: THE DATA SETS

The DEMONSTRATOR's Data Sets					
DS	Time Frame	Enr Active Mass (kg)	Nat Active Mass (kg)	Enr Expos. (kg-d)	Nat Expos. (kg-d)
0	June 27 - Oct. 7, 2015	10.6948	3.905	460.052	171.021
1 open	Dec. 31, 2015 - May 24, 2016	11.901	1.121	661.811	63.2937
1 blind	Dec. 31, 2015 - May 24, 2016	11.901	1.121	184.914	16.7833
2 open	May 24 - July 14, 2016	11.3102	1.121	106.286	10.6791
2 blind	May 24 - July 14, 2016	11.3102	1.121	338.608	33.1995
3	Aug. 25 - Sept. 27, 2016	12.631	2.781	368.523	81.7413
4	Aug. 25 - Sept. 27, 2016	5.4712	3.95	102.858	73.8446
5a	Oct. 13, 2016 - Jan. 27, 2017	17.478	8.997	1260.584	342.168
5b	Jan. 27 - Mar. 17, 2017	18.442	8.997	1260.584	627.585
5c open	Mar. 17 - May 11, 2017	16.963	7.87	674.351	336.23

The Demonstrator's Data Sets Continued					
DS	Time Frame	Enr Active Mass (kg)	Nat Active Mass (kg)	Enr Expos. (kg-d)	Nat Expos. (kg-d)
5c blind	Mar. 17 - May 11, 2017	16.963	7.87	545.716	266.383
6a open	May 11, 2017 - April 18, 2018	17.411	7.881	1366.016	511.882
6a blind	May 11, 2017 - April 18, 2018	17.411	7.881	3260.547	1172.351

Table A.1: The time spans, active masses, and exposures of the Demonstrator's data sets from DS0 up through DS6, the last data set considered in this analysis. This list excludes calibration data, DS6b, and DS6c. Active mass and exposure numbers from [78].

APPENDIX B: T/E CUTS

T/E Cuts For DS1-3,5-6				
data set	E window	detector channels	lower cut	upper cut
6	5-9	660,1302	0.49	1.63
6	5-9	remaining	0.83	1.97
6	9-20	660,1302	0.70	1.42
6	9-20	remaining	1.00	1.79
6	20-100	660,1302	0.82	1.24
6	20-100	remaining	1.12	1.66
5c	5-9	660,1302	0.57	1.59
5c	5-9	628	0.81	1.71
5c	5-9	remaining	0.87	1.95
5c	9-20	660,1302	0.69	1.41
5c	9-20	628	0.96	1.50
5c	9-20	remaining	1.01	1.79
5c	20-100	660,1302	0.82	1.24
5c	20-100	628	1.02	1.38
5c	20-100	remaining	1.12	1.66
5b	5-9	660,1302	0.52	1.60
5b	5-9	628	0.83	1.67
5b	5-9	remaining	0.89	1.91
5b	9-20	660,1302	0.69	1.41
5b	9-20	628	0.94	1.48
5b	9-20	remaining	1.03	1.75
5b	20-100	660,1302	0.81	1.23

T/E Cuts For DS1-3,5-6 Continued				
data set	E window	detector channels	lower cut	upper cut
5b	20-100	628	1.09	1.33
5b	20-100	remaining	1.12	1.66
5a	5-9	660	0.56	1.40
5a	5-9	remaining	0.87	1.95
5a	9-20	660	0.71	1.25
5a	9-20	remaining	0.94	1.84
5a	20-100	660	0.82	1.12
5a	20-100	remaining	1.11	1.65
3	5-9	624	1.06	2.08
3	5-9	592	0.71	1.67
3	5-9	580	0.64	1.36
3	5-9	664	0.77	1.73
3	5-9	remaining	0.87	1.89
3	9-20	624	1.20	1.86
3	9-20	592	0.87	1.47
3	9-20	580	0.79	1.21
3	9-20	664	0.91	1.51
3	9-20	remaining	1.04	1.70
3	20-100	624	1.32	1.74
3	20-100	592	1.00	1.30
3	20-100	580	0.84	1.14
3	20-100	664	1.03	1.39
3	20-100	remaining	1.13	1.61
2	5-9	580	0.65	1.37

T/E Cuts For DS1-3,5-6 Continued				
data set	E window	detector channels	lower cut	upper cut
2	5-9	664	0.75	1.77
2	5-9	remaining	0.87	1.89
2	9-20	580	0.76	1.24
2	9-20	664	0.93	1.53
2	9-20	remaining	1.01	1.73
2	20-100	580	0.84	1.14
2	20-100	664	1.07	1.37
2	20-100	remaining	1.15	1.57
1	5-9	580	0.65	1.37
1	5-9	664	0.74	1.76
1	5-9	remaining	0.84	1.92
1	9-20	580	0.76	1.24
1	9-20	664	0.93	1.53
1	9-20	remaining	1.01	1.73
1	20-100	580	0.84	1.14
1	20-100	664	1.04	1.40
1	20-100	remaining	1.16	1.64

Table B.1: The T/E cuts used for each detector in data sets 1-3 and 5-6. The column "E window" refers to the energy range of the three box cuts shown in Figure 3.8. The "detector channels" column refers to the way in which detectors are grouped together into bands within each data set, as described in Chapter 3.3. The columns "lower cut" and "upper cut" are the upper and lower bounds of the box cut at each energy range.

T/E Cuts For DS4					
data set	E window	run range	detector channels	lower cut	upper cut
4	5-9	60000550-60001868	1106,1144,1236,1332	0.83	1.97
4	5-9	60000550-60001868	1174,1330	0.87	1.71
4	5-9	60000550-60001868	1232	0.84	1.50
4	5-9	60000550-60001868	1136,1170,1172,1176,1204	0.68	1.40
4	5-9	60000550-60001868	1298	0.63	1.29
4	5-9	60001914-60002394	1136,1144,1172,1232	1.01	1.85
4	5-9	60001914-60002394	1106,1170,1174,1176,1204,1236,1298, 1330,1332	0.83	1.85
4	9-20	60000550-60001868	1106,1144,1236,1332	1.06	1.66
4	9-20	60000550-60001868	1174,1330	0.99	1.53
4	9-20	60000550-60001868	1232	0.93	1.35
4	9-20	60000550-60001868	1136,1170,1172,1176,1204	0.78	1.26

T/E Cuts For DS4 Continued					
data set	E window	run range	detector channels	lower cut	upper cut
4	9-20	60000550-60001868	1298	0.74	1.16
4	9-20	60001914-60002394	1136,1144,1172,1232	1.14	1.74
4	9-20	60001914-60002394	1106,1170,1174,1176,1204,1236,1298, 1330,1332	1.01	1.67
4	20-100	60000550-60001868	1106,1144,1236,1332	1.18	1.54
4	20-100	60000550-60001868	1174,1330	1.09	1.39
4	20-100	60000550-60001868	1232	1.00	1.24
4	20-100	60000550-60001868	1136,1170,1172,1176,1204	0.88	1.18
4	20-100	60000550-60001868	1298	0.82	1.06
4	20-100	60001914-60002394	1136,1144,1172,1232	1.21	1.69
4	20-100	60001914-60002394	1106,1170,1174,1176,1204,1236,1298, 1330,1332	1.14	1.56

Table B.2: The DS4 T/E cuts have different definitions for different run ranges because a gain shift occurred part of the way through the data set which shifted the T/E vs energy distributions for many of the detectors.

APPENDIX C: PULSER RETRIGGER CUTS

Pulser Retrigger Cuts For DS1-6		
data set	detector channels	trapETailMin cutoff
6	678	0.1
6	584, 610, 658, 660, 1172, 1176,	-0.1
6	592, 608, 624, 626, 628, 632, 640, 648, 662, 672, 674, 680, 688, 690, 694, 1106, 1124, 1128, 1204, 1232, 1236, 1298, 1302, 1330, 1332	-0.2
6	598, 1120, 1174, 1208, 1332	-0.3
6	614	-0.4
5c	628	1.8
5c	624, 1128	1
5c	1120	0.7
5c	680, 1124, 1170, 1174, 1208, 1302, 1330	0.5
5c	592, 614, 626, 640, 688, 1106	0.4
5c	608, 610, 632, 658, 672, 674, 690, 694, 1172	0.3
5c	584, 598, 648, 660, 678, 1176, 1298, 1332	0.2
5c	662	0.1
5b	628	1.3
5b	1330	0.9
5b	1128, 1232	0.8
5b	1106, 1302	0.7
5b	624, 1176	0.6
5b	592, 626, 1120, 1124, 1170, 1208, 1236, 1298	0.5

Pulser Retrigger Cuts For DS1-6 Continued		
data set	detector channels	trapETailMin cutoff
5b	614, 688, 1174, 1204	0.4
5b	598, 640, 658, 680, 690, 692, 694	0.3
5b	584, 608, 610, 648, 660, 672, 674, 67, 1172	0.2
5b	632, 662	0.1
5a	628	1.5
5a	592, 624, 680, 692, 1128	1
5a	688	0.7
5a	1120, 1176, 1204, 1330, 1332	0.6
5a	658, 694, 1106, 1174, 1232, 1236, 1302	0.5
5a	584, 610, 640, 1170, 1208	0.4
5a	608, 626, 674, 690, 1124	0.3
5a	598, 614, 648, 660, 662, 678, 1172	0.2
5a	632, 1168, 1298	0
4	1106	0.7
4	1144, 1170	0.6
4	1204, 1236, 1298	0.5
4	1136, 1172, 1174, 1232, 1330	0.4
4	1176	0.3
4	1332	0.2
4	1296	0
3	692	1
3	592, 624	0.8

Pulser Retrigger Cuts For DS1-6 Continued		
data set	detector channels	trapETailMin cutoff
3	594, 610, 614, 690, 694	0.6
3	626, 672	0.5
3	578, 580, 600, 608, 640	0.4
3	582, 648, 664	0.3
3	632	0.2
3	678	-0.1
2	610, 672	0
2	578, 592, 608, 632, 648, 664, 692	-0.1
2	580, 598, 600, 626, 640, 690	-0.2
2	582	-0.3
1	578, 594, 626, 690	0.6
1	640, 672	0.5
1	580, 592, 598, 600, 608, 610, 648, 664, 692	0.4
1	582, 632	0.3

Table C.1: Table of pulser retrigger cuts, organized by the data sets and detector channels they are applied to.

BIBLIOGRAPHY

[1] D. J. Eisenstein et al., "Detection of the Baryon Acoustic Peak in the Large-Scale Correlation Function of SDSS Luminous Red Galaxies," *The Astrophysical Journal* **633** (2005) .

[2] J. M. Kovac et al., "Detection of polarization in the cosmic microwave background using DASI," *Nature* **420** (2002) 772787.

[3] P. A. R. Ade, "Planck 2015 results," *Astronomy and Astrophysics* **594** (2016) .

[4] T. Nakama, J. Chluba, and M. Kamionkowski, "Shedding light on the small-scale crisis with CMB spectral distortions," *Phys. Rev. D* **95** (2017) 121302(R).

[5] D. N. Spergel, "The dark side of cosmology: Dark matter and dark energy," *Science* **347** (2015) 1100–1102.

[6] R. Buta, "The structure and dynamics of ringed galaxies. III - Surface photometry and kinematics of the ringed nonbarred spiral NGC 7531," *Astrophysical Journal Supplement Series* **64** (1987) 1–37.

[7] V. C. Rubin and W. K. Ford Jr., "Rotation of the Andromeda Nebula from a Spectroscopic Survey of Emission Regions," *Astrophysical Journal* **159** (1970) 379.

[8] D. H. Rogstad, "Aperture synthesis study of neutral hydrogen in the galaxy M101: II. Discussion," *Astronomy and Astrophysics* **13** (1971) 108–115.

[9] D. H. Rogstad and G. S. Shostak, "Gross Properties of Five Scd Galaxies as Determined from 21-CENTIMETER Observations," *Astrophysical Journal* **176** (1972) 315.

[10] M. S. Roberts and A. H. Rots, "Comparison of Rotation Curves of Different Galaxy Types," *Astronomy and Astrophysics* **26** (1973) 483–485.

[11] K. C. Freeman, "On the Disks of Spiral and S0 Galaxies," *Astrophysical Journal* **160** (1970) 811.

[12] P. J. E. Peebles, *Physical Cosmology*. Princeton University Press, 1971.

[13] K. G. Begeman, A. H. Broeils, and R. H. Sanders, "Extended rotation curves of spiral galaxies - Dark haloes and modified dynamics," *MNRAS* **249** (1991) 523–537.

[14] L. Calada, NASA, and ESA, "Gravitational lensing in action." `https://www.spacetelescope.org/images/heic1106c/`. Accessed: 2019-03-16.

[15] R. Massey, T. Kitching, and J. Richard, "The dark matter of gravitational lensing," *Reports on Progress in Physics* **73** (2010) .

[16] M. J. Jee, H. Ford, NASA, and ESA, "Astronomers Find Ring of Dark Matter." `https://www.nasa.gov/mission_pages/hubble/news/dark_matter_ring_mm.html`. Accessed: 2019-03-17.

[17] D. Clowe, M. Bradac, A. H. Gonzalez, M. Markevitch, S. W. Randall, C. Jones, and D. Zaritsky, "A Direct Empirical Proof of the Existence of Dark Matter," *The Astrophysical Journal Letters* **648** (2006) .

[18] M. Milgrom, "A modification of the Newtonian dynamics as a possible alternative to the hidden mass hypothesis," *Astrophysical Journal* **270** (1983) 365–370.

[19] R. H. Sanders and M. A. W. Verheijen, "Rotation Curves of Ursa Major Galaxies in the Context of Modified Newtonian Dynamics," *Astrophysical Journal* **503** (1998) 97.

[20] F. Zwicky, "Die Rotverschiebung von extragalaktischen Nebeln," *Helvetica Physica Acta* **6** (1933) 110127.

[21] F. Zwicky, "On the Masses of Nebulae and of Clusters of Nebulae," *ApJ* **86** (1937) 217.

[22] K. Freese, "Review of Observational Evidence for Dark Matter in the Universe and in upcoming searches for Dark Stars," *EAS Publications Series* **36** (2009) 113126.

[23] A. Kravtsov and S. Borgani, "Formation of Galaxy Clusters," *Annual Review of Astronomy and Astrophysics 50* **50** (2012) 353409.

[24] J. Ellis, J. S. Hagelin, D. V. Nanopoulos, K. Olive, and M. Srednicki, "Supersymmetric relics from the big bang," *Nuc. Phys. B* **238** (1984) 453–476.

[25] G. Bertone, D. Hooper, and J. Silk, "Particle dark matter: evidence, candidates and constraints," *Physics Reports* **405** (2005) 279–390.

[26] E. Armengaud et al., "Measurement of the cosmogenic activation of germanium detectors in EDELWEISS-III," *Astropart. Phys.* **91** (2017) 5164.

[27] E. Aprile et al., "First Dark Matter Search Results from the XENON1T Experiment," *Phys. Rev. Lett.* **119** (2017) 181301.

[28] P. Akerib et al., "First Results from the LUX Dark Matter Experiment at the Sanford Underground Research Facility," *Phys. Rev. Lett.* **112** (2014) 091303.

[29] P. Agnes et al., "First results from the DarkSide-50 dark matter experiment at Laboratori Nazionali del Gran Sasso," *Phys. Lett. B* **743** (2015) 456–466.

[30] J. Billard, E. Figueroa-Feliciano, and L. Strigari, "Implication of neutrino backgrounds on the reach of next generation dark matter direct detection

experiments," *Phys. Rev. D* **89** (2014) 023524.

[31] P. S. Finnerty, *A Direct Dark Matter Search with the* MAJORANA *Low-Background Broad Energy Germanium Detector*. PhD thesis, UNC-Chapel Hill, 2013.

[32] L. Baudis, "WIMP Dark Matter Direct-Detection Searches in Noble Gases," *Phys. Dark Univ.* **4** (2014) 5059.

[33] R. D. Peccei and H. R. Quinn, "CP conservation in the presence of pseudoparticles," *Phys. Rev. Lett.* **38** (1977) 1440–1443.

[34] R. D. Peccei and H. R. Quinn, "Constraints imposed by CP conservation in the presence of pseudoparticles," *Phys. Rev. D* **16** (1977) 1791.

[35] F. Wilczek, "Problem of Strong P and T Invariance in the Presence of Instantons," *Phys. Rev. Lett.* **40** (1978) 279–282.

[36] S. Weinberg, "A New Light Boson?," *Phys. Rev. Lett.* **40** (1978) 223.

[37] J. E. Kim and G. Carosi, "Axions and the strong CP problem," *Rev. Mod. Phys.* **82** (2010) 557.

[38] C. A. Baker et al., "Improved Experimental Limit on the Electric Dipole Moment of the Neutron," *Phys. Rev. Lett.* **97** (2006) 131801.

[39] I. G. Irastorza and J. Redondo, "New experimental approaches in the search for axion-like particles," *Progress in Particle and Nuclear Physics* **102** (2018) 89–159.

[40] M. Pospelov, A. Ritz, and M. Voloshin, "Bosonic super-WIMPs as keV-scale dark matter," *Phys. Rev. D* **78** (2008) 115012.

[41] Z. Ahmed et al., "Search for Weakly Interacting Massive Particles with the First Five-Tower Data from the Cryogenic Dark Matter Search at the Soudan Underground Laboratory," *Phys. Rev. Lett.* **102** (2009) 011301.

[42] P. Akerib et al., "Exploring the Role of Axions and Other WISPs in the Dark Universe," *ArXiv e-prints* (2012) . arXiv:1210.5081 [hep-ph].

[43] E. Masso and R. Toldra, "Light spinless particle coupled to photons," *Phys. Rev. D* **52** (1995) 1755.

[44] E. Masso, "Axions and Axion-like Particles," *Nuc. Phys. B (Proc. Suppl.)* **114** (2003) 67–73.

[45] W. Pauli, "Pauli letter collection: letter to Lise Meitner." `https://cds.cern.ch/record/83282?ln=en`, 1930. Accessed: 2019-03-17.

[46] F. L. Wilson, "Fermi's theory of beta decay," *American Journal of Physics* **36** (1968) 11501160.

[47] F. Reines et al., "Detection of the free antineutrino," *Physical Review* **117** (1960) 159.

[48] M. Goeppert-Mayer, "Double beta-disintegration," *Physical Review* **48** (1935) 512.

[49] S. R. Elliott, A. A. Hahn, and M. K. Moe, "Direct evidence for two-neutrino double-beta decay in Se 82," *Phys. Rev. Lett.* **59** (1987) 2020.

[50] A. Giuliani and A. Poves, "Neutrinoless Double-Beta Decay," *Advances in High Energy Physics* (2012) 1687–7357.

[51] W. H. Furry, "On transition probabilities in double beta-disintegration," *Physical Review* **56** (1939) 1184.

[52] B. Kayser, "Introduction To Massive Neutrinos," *Proceedings, 4th Moriond Workshop* (1984) 11–44. `http://inspirehep.net/record/201394`.

[53] J. Schechter and J. Valle, "Neutrino decay and spontaneous violation of lepton number," *Physical Review D* **25** (1982) 774.

[54] C. G. Wiseman, *An Axion Search With The Majorana Demonstrator*. PhD thesis, University of South Carolina, 2018.

[55] P. D. Bari, "An introduction to leptogenesis and neutrino properties," *Contemporary Physics* **53** (2012) 315–338.

[56] L. Canetti, M. Drewes, and M. Shaposhnikov, "Matter and Antimatter in the Universe," *New J.Phys.* **14** (2012) 095012.

[57] A. D. Sakharov, "Violation of CP Invariance, c Asymmetry, and Baryon Asymmetry of the Universe," *Pisma Zh.Eksp.Teor.Fiz.* **5** (1967) 32–35.

[58] C. Balazs, "Baryogenesis: A small review of the big picture," *ArXiv e-prints* (2014) . arXiv:1411.3398 [hep-ph].

[59] N. Abgrall et al., "The Large Enriched Germanium Experiment for Neutrinoless Decay: Legend-200 at LNGS," *Proposal submitted to LNGS* (2018) . `https://github.com/legend-exp/legend200-proposal-lngs/releases/tag/v03.02`.

[60] C. E. Aalseth et al., "Search for Neutrinoless Double-β Decay in ^{76}Ge with the Majorana Demonstrator," *Phys. Rev. Lett.* **120** (2018) 132502.

[61] V. Guiseppe, "New Results from the MAJORANA DEMONSTRATOR Experiment,". DOI:10.5281/zenodo.1286900.

[62] M. J. Dolinski, A. W. P. Poon, and W. Rodejohann, "Neutrinoless Double-Beta Decay: Status and Prospects," *ArXiv e-prints* (2019) . arXiv:1902.04097 [nucl-ex].

[63] R. Henning, "Neutrinoless Double-Beta Decay: Status and Prospects," *Rev. Phys.* **1** (2016) 29–35.

[64] F. T. Avignone, S. R. Elliott, and J. Engel, "Double beta decay, Majorana neutrinos, and neutrino mass," *Rev. Mod. Phys.* **80** (2008) 481.

[65] SURF, "Sanford Underground Research Facility." `https://www.sanfordlab.org`. Accessed: 2019-03-16.

[66] N. Abgrall et al., "Muon Flux Measurements at the Davis Campus of the Sanford 23 Underground Research Facility with the Majorana Demonstrator Veto System," *ArXiv e-prints* (2016) . arXiv:1602.07742 [nucl-ex].

[67] K. R. Vorren, *A Direct Search for Dark Matter with the Majorana Demonstrator*. PhD thesis, UNC-Chapel Hill, 2017.

[68] B. T. Cleveland, T. Daily, J. R. Davis, J. R. Distel, K. Lande, C. K. Lee, P. Wildenhain, and J. Ullman, "Measurement of the Solar Electron Neutrino Flux with the Homestake Chlorine Detector," *The Astrophysical Journal* **496** (1998) 505.

[69] P. Akerib et al., "LUX-ZEPLIN (LZ) Conceptual Design Report," *ArXiv e-prints* (2016) . arXiv:1509.02910v2 [physics.ins-det].

[70] N. Abgrall et al., "The MAJORANA DEMONSTRATOR Neutrinoless Double-Beta Decay Experiment," *Advances in High Energy Physics* **2014** (2014) .

[71] E. Aguayo et al., "The design of an ultra-low background thermosyphon for the MAJORANA Demonstrator," *NIM A* **701** (2013) 176–185.

[72] N. Abgrall et al., "The Majorana Low-noise Low-background Front-end Electronics," *Physics Procedia* **61** (2015) 654–657.

[73] S. Zimmermann, J. T. Anderson, and D. Doering et al., "Implementation and performance of the electronics and computing system of the gamma ray energy tracking in-beam nuclear array (GRETINA)," *IEEE Transactions on Nuclear Science* **59** (2012) 24942500.

[74] VITA, "VME bus Technology FAQ." `https://www.vita.com/page-1855175`. Accessed: 2019-03-24.

[75] M. A. Howe, G. A. Cox, and P. J. Harvey et al., "Sudbury neutrino observatory neutral current detector acquisition software overview," *IEEE Transactions on Nuclear Science* **51** (2004) 878883.

[76] NERSC, "National Energy Research Scientific Computing Center." https://www.nersc.gov. Accessed: 2019-03-24.

[77] N. Abgrall et al., "New Limits on Bosonic Dark Matter, Solar Axions, Pauli Exclusion Principle Violation, and Electron Decay from the MAJORANA DEMONSTRATOR," *Phys. Rev. Lett.* **118** (Apr, 2017) 161801. https://link.aps.org/doi/10.1103/PhysRevLett.118.161801.

[78] D. Edwins et al., "Livetime and Exposure for Majorana Demonstrator Data Sets 0-6," tech. rep., University of Washington, 2018. https://mjdoc.npl.washington.edu/record/1909/files/livetime_DS0-6_2018-05-21_v3.pdf.

[79] C. D. Christofferson et al., "Contamination control and assay results for the MAJORANA DEMONSTRATOR ultra clean components," *AIP Conference Proceedings* **1921** (2018) .

[80] B. D. LaFerriere, T. C. Maiti, I. J. Arnquist, and E. W. Hoppe, "A novel assay method for the trace determination of Th and U in copper and lead using inductively coupled plasma mass spectrometry," *Nucl. Instrum. Meth. A* **775** (2015) 93–98.

[81] E. W. Hoppe et al., "Microscopic evaluation of contaminants in ultra-high purity copper," *J. Radioanal. Nucl. Chem.* (2009) 282–315.

[82] E. W. Hoppe et al., "Use of electrodeposition for sample preparation and rejection rate prediction for assay of electroformed ultra high purity copper for Th-232 and U-238 prior to inductively coupled plasma mass spectrometry (ICP/MS)," *J. Radioanal. Nucl. Chem.* **277** (2008) 103110.

[83] E. W. Hoppe et al., "Reduction of radioactive backgrounds in electroformed copper for ultra-sensitive radiation detectors," *Nucl. Instrum. Meth. A* **764** (2014) 116–121.

[84] N. R. Overman, E. W. Hoppe, and R. S. Addleman, "Surface cleaning techniques: ultra-trace ICP-MS sample preparation and assay of HDPE," *J. Radioanal. Nucl. Chem.* **269** (2013) 13031310.

[85] E. W. Hoppe et al., "A method for removing surface contamination on ultra-pure copper spectrometer components," *J. Radioanal. Nucl. Chem.* **276** (2008) 645650.

[86] E. W. Hoppe et al., "Cleaning and passivation of copper surfaces to remove surface radioactivity and prevent oxide formation," *J. Radioanal. Nucl. Chem.* **579** (2007) 486–489.

[87] J. Amare et al., "Cosmogenic production of tritium in dark matter detectors," *Astropart. Phys.* **97** (2018) 96105.

[88] R. Agnese et al., "Production rate measurement of Tritium and other cosmogenic isotopes in Germanium with CDMSlite," *Astropart. Phys.* **104** (2019) 112.

[89] F. Avignone et al., "Theoretical and experimental investigation of cosmogenic radioisotope production in germanium," *Nuclear Physics B (Proceedings Supplements)* **28A** (1992) 280–285.

[90] N. Abgrall et al., "The processing of enriched germanium for the Majorana Demonstrator and R&D for a next generation double-beta decay experiment," *Nucl. Instrum. Meth. Phys. Res. Sec. A* **877** (2018) 314–322.

[91] L. Lucas and M. Unterweger, "Comprehensive Review and Critical Evaluation of the Half-Life of Tritium," *Journal of Research of the National Institute of Standards and Technology* **105** no. 4, (2000) 541.

[92] I. Barabanov et al., "Cosmogenic activation of germanium and its reduction for low background experiments," *Nucl. Inst. Meth. B* **251** (2006) 115120.

[93] G. K. Giovanetti, *P-type Point Contact Germanium Detectors and their Application in Rare-Event Searches*. PhD thesis, UNC-Chapel Hill, 2015.

[94] C. E. Aalseth et al., "CoGeNT: A search for low-mass dark matter using p-type point contact germanium detectors," *Phys. Rev. D* **88** (2013) 012002.

[95] P. Barbeau, *Neutrino and Astroparticle Physics with P-Type Point Contact High Purity Germanium Detectors*. PhD thesis, University of Chicago, 2009.

[96] P. Luke, F. Goulding, F. Madden, and R. H. Pehl, "Low Capacitance Large Volume Shaped-Field Germanium Detector," *IEEE Transactions on Nuclear Science* **36** (1999) 926930.

[97] Mirion, "SEGE: Standard Electrode Coaxial Ge Detectors." `https://www.mirion.com/products/sege-standard-electrode-coaxial-ge-detectors`, Accessed: 2019-03-24.

[98] M. Agostini et al., "The background in the 0 nu beta beta experiment GERDA," *The European Physical Journal C* **74** (2014) 1–25.

[99] G. Knoll, *Radiation detection and measurement*. John Wiley, 2010.

[100] G. Gilmore, *Practical Gamma-ray Spectroscopy*. Wiley, 2008.

[101] ORTEC, "ORTEC." `https://ortec.com/en-us/`, Accessed: 2019-03-24.

[102] Mirion, "Germanium." `https://www.mirion.com/products/germanium-detectors`, Accessed: 2019-03-24.

[103] W. Shockley, "Currents to Conductors Induced by a Moving Point Charge," *Journal of Applied Physics* **9** (1938) 635.

[104] S. Ramo, "Currents Induced by Electron Motion," *Proceedings of the IRE* **27** (1939) 584585.

[105] M. B. Budjas, M. B. Heider, O. Chkvorets, N. Khanbekov, and S. Schonert, "Pulse shape discrimination studies with a broad-energy germanium detector for signal identification and back- ground suppression in the GERDA double beta decay experiment," *Journal of Instrumentation* **4** (2009) . Article ID P10007.

[106] C. Cuesta, "Multi-site event discrimination for the MAJORANA DEMONSTRATOR data," tech. rep., MAJORANA Collaboration, 2018. `https://mjdoc.npl.washington.edu/record/1858/files/avse_unidoc_180804.pdf`.

[107] E. Aguayo et al., "Characteristics of signals originating near the lithium-diffused N+ contact of high purity germanium p-type point contact detectors," *Nucl. Instrum. Meth. A* **701** (2013) 176185.

[108] M. Agostini et al., "Pulse shape discrimination for Gerda Phase I data," *European Physical Journal C* **73** (2013) 2583.

[109] P. Chu et al., "Unidoc of Energy Performance of MAJORANA DEMONSTRATOR," tech. rep., MAJORANA Collaboration, 2018.

[110] V. T. Jordanov, G. F. Knoll, A. C. Huber, and J. A. Pantazis, "Digital techniques for real-time pulse shaping in radiation measurements," *Nucl. Instrum. Meth. Phys. Res. Sec. A* **353** (1994) 261–264.

[111] V. T. Jordanov and G. F. Knoll, "Digital synthesis of pulse shapes in real time for high resolution radiation spectroscopy," *Nucl. Instrum. Meth. Phys. Res. Sec. A* **345** (1994) 337–345.

[112] Ortec, "Introduction to Amplifiers." `https://www.ortec-online.com/-/media/ametekortec/other/amplifier-introduction.pdf?la=en`, Accessed: 2019-02-17.

[113] N. Abgrall et al., "The Majorana Parts Tracking Database," *Nucl. Instrum. Meth. in Physics* **779** (2015) 5262.

[114] C. Cuesta, "PSA A/E optimization," tech. rep., University of Washington, 2014. `http://mjwiki.npl.washington.edu/pub/Majorana/AnalysisReports/PSA_141208.pdf`.

[115] C. Cuesta, A. Reine, T. Caldwell, and C. Wiseman, "Run selection and data cleaning of DS0 (P3JDY)," tech. rep., MAJORANA Collaboration, 2017. `https://mjdoc.npl.washington.edu/record/1854/files/RSDC_DS0_171031.pdf`.

[116] C. Cuesta, A. Reine, and C. Wiseman, "Run selection and data cleaning of DS1 (P3KJR)," tech. rep., MAJORANA Collaboration, 2017. `https://mjdoc.npl.washington.edu/record/1855/files/RSDC_DS1_170925.pdf`.

[117] A. Reine, C. Cuesta, and C. Wiseman, "Run selection and data cleaning of DS2 (M1)," tech. rep., MAJORANA Collaboration, 2017. https://mjdoc.npl.washington.edu/record/1857/files/RSDC_DS2_171031.pdf.

[118] C. Cuesta, M. Buuck, A. Reine, and C. Wiseman, "Run selection and data cleaning of DS3 (M1)," tech. rep., MAJORANA Collaboration, 2017. https://mjdoc.npl.washington.edu/record/1852/files/RSDC_DS3_171031.pdf.

[119] C. Cuesta, M. Buuck, A. Reine, and C. Wiseman, "Run selection and data cleaning of DS4 (M2)," tech. rep., MAJORANA Collaboration, 2017. https://mjdoc.npl.washington.edu/record/1853/files/RSDC_DS4_171031.pdf.

[120] A. Reine, T. Caldwell, C. Cuesta, I. Guinn, J. Myslik, and C. Wiseman, "Run selection and data cleaning of DS5 (M1 and M2)," tech. rep., MAJORANA Collaboration, 2018. https://mjdoc.npl.washington.edu/record/1868/files/RSDC_DS5_180526.pdf.

[121] A. Reine, T. Caldwell, C. Cuesta, I. Guinn, J. Myslik, and C. Wiseman, "Run selection and data cleaning of DS6 (M1 and M2)," tech. rep., MAJORANA Collaboration, 2018. https://mjdoc.npl.washington.edu/record/1912/files/RSDC_DS6_v1.pdf.

[122] Paul Scherrer Institut, "ELOG Site." https://elog.psi.ch.

[123] C. Wiseman and B. Zhu, "Low Energy Analysis Toolkit (LAT) Results for Data Sets 06A," tech. rep., MAJORANA Collaboration, 2018. https://mjdoc.npl.washington.edu/record/1914/files/low_e_lat_analysis_v1.pdf.

[124] NIST, "Xcom: Photon cross sections database." https://physics.nist.gov/PhysRefData/Xcom/html/xcom1.html, Accessed: 2018-06-09.

[125] R. A. Johnson, *Alpha Backgrounds and Their Implications for Neutrinoless Double-Beta Decay Experiments Using HPGe Detectors*. PhD thesis, University of Washington, 2010.

[126] F. James, *Statistical Methods in Experimental Physics: 2nd Edition*. World Scientific Publishing, 2006.

[127] R. J. Barlow, *Statistics: A Guide to the Use of Statistical Methods in the Physical Sciences*. John Wiley & Sons, 1989.

[128] W. Verkerke and D. Kirkby, "The RooFit toolkit for data modeling." https://www.mirion.com/products/germanium-detectors. arXiv:0306116.

[129] S. S. Wilks, "The Large-Sample Distribution of the Likelihood Ratio for Testing Composite Hypotheses," *Ann. Math. Statist* **9** (1938) 6062.

[130] S. Mertens et al., "Sensitivity of next-generation tritium beta-decay experiments for keV-scale sterile neutrinos," *Journal of Cosmology and Astroparticle Physics* **2015** (2015) 020.

[131] B. White, "Private communication.".

[132] E. Armengaud et al., "Axion searches with the EDELWEISS-II experiment," *Journal of Cosmology and Astroparticle Physics* **2013** (2013) 067.

[133] J. D. Lewin and P. F. Smith, "Review of mathematics, numerical factors, and corrections for dark matter experiments based on elastic nuclear recoil," *Astropart. Phys* **6** (1996) 87–112.

[134] M. Pospelov, A. Ritz, and M. Voloshin, "Bosonic super-WIMPs as keV-scale dark matter," *Phys.Rev. D* **78** (2008) 115012.

[135] H. An, M. Pospelov, J. Pradler, and A. Ritz, "Direct detection constraints on dark photon dark matter," *Physics Letters B* **747** (2015) 331 338.

[136] E. Armengaud et al., "Searches for electron interactions induced by new physics in the EDELWEISS-III Germanium bolometers E.," *Phys. Rev. D* **98** (2018) 082004.

[137] XMASS Collaboration, "Search for dark matter in the form of hidden photons and axion-like particles in the XMASS detector," *Physics Letters B* **787** (2018) 153–158.

[138] C. Fu et al., "Limits on Axion Couplings from the First 80 Days of Data of the PandaX-II Experiment," *Phys. Rev. Lett.* **119** (2017) 181806.

[139] E. Aprile et al., "Erratum: First axion results from the XENON100 experiment [Phys. Rev. D 90, 062009 (2014)]," *Phys. Rev. D* **95** (2017) 029904.

[140] S. Liu et al., "Constraints on axion couplings from the CDEX-1 experiment at the China Jinping Underground Laboratory," *Phys. Rev. D* **95** (2017) 052006.

[141] D. Akerib et al., "First Searches for Axions and Axionlike Particles with the LUX Experiment," *Phys. Rev. Lett.* **118** (2017) 261301.